(Al,Ga)(As,P) Structures in the GaP Matrix: Growth and Characterization

DISSERTATION

zur Erlangung des akademischen Grades

doctor rerum naturalium

(Dr. rer. nat.)

im Fach Physik

eingereicht an der

Mathematisch-Naturwissenschaftlichen Fakultät

der Humboldt-Universität zu Berlin

von

M. Sc. Shabnam Dadgostar

Präsident der Humboldt–Universität zu Berlin

Prof. Dr. Sabine Kunst

Dekan der Mathematisch–Naturwissenschaftlichen Fakultät

Prof. Dr. Elmar Kulke

Gutachter:

1. Prof. Dr. W. T. Masselink
2. Prof. Dr. H. Riechert
3. Prof. Dr. T. Hannappel

Tag der Dissputation: 18.07.2016

Contents

Acknowledgments iv

Zusammenfassung - Abstract vi

1 Introduction **1**

2 Gas–Source Molecular–Beam Epitaxy **7**

2.1 Molecular–beam epitaxy 9

2.2 Ultra–high vacuum environment 10

2.3 Gas source MBE 12

2.4 The physics of MBE growth 14

2.4.1 Surface and epitaxial growth 15

2.4.2 Surface growth modes 18

2.5 Growth of quantum dots in self–assembled mode 21

3 Experimental characterization methods **25**

3.1 Structural characterization methods 27

3.1.1 Reflection high–energy electron diffraction (RHEED) . . . 27

3.1.2 High resolution X–ray diffraction 28

3.1.3 Atomic–force microscopy 32

3.1.4 Scanning Electron Microscopy 33

3.2 Optical characterization methods 36

3.2.1 Cathodoluminescence measurement 36

3.2.2 Photoluminescence (PL) measurement 37

3.2.3 Time–resolved PL measurement 37

4 Semiconductors and quantum dots heterostructures 39
4.1 Crystal structure 41
4.2 Band structure and energy gap 42
4.3 Heterostructures band alignment 45
4.4 Strain and model–solid theory 47
4.4.1 Strain induced energy shift 50
4.4.2 Valence band splitting due to strain 51
4.4.3 Conduction band splitting due to strain 52
4.5 Quantum confinement effect in quantum structures 52
4.5.1 Density of electronic states 54
4.6 Optical properties 55

5 AlGaP/GaP heterostructure 57
5.1 Photonic crystals 59
5.2 Photonic crystal cavity in the visible range of wavelength 62
5.3 Homoepitaxial growth of GaP: influences of growth temperature and PH_3 flux 62
5.4 AlGaP/GaP heterostructure:influences of growth temperature and PH_3 flux 65
5.5 Summary 72

6 GaAs quantum structures in the GaP matrix 73
6.1 III–V semiconductors QD in a GaP matrix 76
6.2 GaAs/GaP heterostructure 77
6.2.1 Electronic structure of GaAs in the GaP matrix 77
6.2.2 Growth and characterization of GaAs QDs on GaP (100) substrate 80
6.2.3 Influence of growth temperature on GaAs QDs 102
6.3 LEDs based on GaAs QDs embedded in GaP 113
6.3.1 LEDs based on the III–V semiconductors 113
6.3.2 Growth and processing 115
6.3.3 Optical results 117

6.4 Summary 119

7 $Al_xGa_{1-x}As$ quantum structure in the GaP matrix **121**

7.1 Electronic structure of $Al_xGa_{1-x}As/GaP$ 123

7.2 Growth and characterization of $Al_xGa_{1-x}As/GaP$ 125

7.3 Summary 134

8 Conclusion **135**

Appendix **139**

Appendix.I 139

Appendix.II 140

Appendix.III 141

Bibliography **143**

Curriculum Vitae **164**

Selbständigkeitserklärung 167

Acknowledgments

I would like to express my very special appreciation and thanks to my thesis supervisor Dr. Fariba Hatami. I would like to thank you for encouraging my research and for helping me to grow as a research scientist. I am thankful for your aspiring guidance, constructive criticism and friendly advice.

Very special appreciation to Prof. Dr. Ted Masselink. I am sincerely grateful to you for letting me work in your group. You motivated me and your comments helped me to think as a researcher and improved my work.

A very special thanks to Prof. Dr. Juan Jimenez, to Prof. Dr. Oscar Martinez, and to Dr. Alfredo Torres from Valladolid University for the optical characterizations. This thesis cannot come to this point without your help and comments and I appreciate it.

I would also like to express my appreciation to Dr. Jan Schmidtbauer and to Dr. Torsten Boeck from Leibniz–Institut für Kristallzüchtung for teaching me to work with atomic force microscopy system that was a critical measurement for characterizing my samples.

I would also like to thank Dr. Jens Tomm from Max–Born–Institute for the time resolved measurements and his comments related to the data analysis.

I would also like to thank Dr. Anna Mogilatenko in the Physics institute of Humboldt University for the TEM measurements.

I would like to express my sincere appreciation to Dr. Pierre Corfdir from Paul – Durde – Institute for low–temperature optical measurements.

A very special thanks to Dr. Mykhaylo Semtsiv. I am grateful for your help with the MBE system and your comments.

My sincere thanks also to Dr. Vanesa Hortelano Santos, to Dr. Yuri V. Flores, Mrs. Karin Braune and Mrs. Maryam Nazarzadeh. Thank you guys for your friendship, critical thinking, and continuous support.

I would like to express my deepest appreciation to all the members of the FET research group for their suggestions and critical comments in our weekly meetings.

This research would not have been possible without the financial assistance of the Yousef Jameel scholarship foundation. I want to express my gratitude to this agency.

My sincere thanks also to Dr. Uta Hoffmann from Young Researchers office for her friendship and continuous support.

My special thanks to my friends Masoumeh, Parvaneh, Salil, Sara, Zohreh, Nafiseh, Rahimeh, Azin, and Nahid. Thank you guys for your friendship, continuous support, and encouragements.

I would like to express my heartfelt appreciation to my uncle and aunt, Keyhan and Ajeh, and my cousin Nijousha for their supports and encouragements during the last five years.

I cannot end these acknowledgments without mentioning my heartfelt appreciation to my parents Shahmir and Mina, my sister Shaghayegh, and my brother Shervin, who supported me throughout the entire process, both by keeping me harmonious and helping me putting pieces together.

Abstract

Transparency of GaP due to the large indirect bandgap energy and its small lattice mismatch with Si make GaP an interesting candidate for optoelectronic devices in visible wavelength. This thesis is an investigation on the structural and optical characteristics of (Al,Ga)(As,P) heterostructures grown on GaP (001) substrates. The influences of the PH_3 flux and growth temperature are studied on the crystal and surface quality of AlGaP/GaP heterostructure. The results indicate the narrow growth window of PH_3 = 2.7 sccm and growth temperature = 490°C as the optimized conditions. To overcome the inefficient light emission of indirect GaP, direct bandgap GaAs was grown as the quantum structures in the GaP matrix. The QD formation is driven by the 3.7% lattice mismatch between GaAs and GaP for GaAs nominal thickness above 1.2 ML. The optical measurements show two peaks in the range of 1.7 to 2.1 eV and the luminescence up to room temperature for 2.7 and 3.6 ML samples. The high energy emission is attributed to indirect carrier recombination in the thin quantum wells or small strained quantum dots, whereas the low energy red emission is due to the direct electron-hole recombination in the relaxed quantum dots. The influence of the Al content on the band alignment and electronic structure of (Al,Ga)As quantum structures is studied. The optical spectra illustrate the blueshift of the radiative emission with increasing the Al content and the highest emission energy of 2.17 eV is observed for the (Al,Ga)As/GaP system that is related to the indirect type-II radiative recombination.

Keywords: III-V semiconductor, GaP, AlGaP, GaAs, AlGaAs, growth temperature, PH_3 flux, quantum structures, lattice mismatch, luminescence.

Zusammenfassung

GaP ist ein Halbleiter mit einer großen Bandlückenenergie und infolgedessen transparent im größten Teil der sichtbaren Wellenlängen. GaP hat außerdem die kleinste Gitterfehlanpasung zu Si (weniger als 0.4%). Das macht GaP ein interessantes Material für monolithische Integration zu III–V Lichtsender auf Si. Diese Arbeit ist eine Untersuchung über die strukturellen und optische Eigenschaften von (Al, Ga) (As, P) Heterostrukturen auf GaP (001) -Substrat aufgewachsen. Die Einflüsse des PH_3 Fluss und Wachstumstemperatur untersucht auf dem Kristallqualität und Oberflächenqualität von AlGaP/GaP Heterostructure. Experimentelle Ergebnisse deuten darauf hin, dass eine Wachstumstemperatur von 490 ^{o}C und ein geknackter (engl. cracked) PH_3 Fluss von 2.7 sccm zur besten AlGaP Qualität und gleichzeitig zur guten GaP Qualität führen. Um die ineffiziente Lichtemission von GaP zu überwinden wurde GaAs in der GaP-Matrix gewachsen. Die Entstehung der Quantenpunkte wurde durch die 3.7% Gitterfehlanpassung zwischen GaAs und GaP für GaAs Nenndicke über 1,2 ML. Die optischen Messungen zeigen zwei Peaks im Bereich von 1,7 bis 2,1 eV und die Lumineszenz auf Raumtemperatur für 2,7 und 3,6 ML-Proben. Die hohe Energieemission wird der indirekten Rekombination in den dünnen Quantentröge oder kleine gespannte Quantenpunkte zurückzuführen, Während die niedrige Energie Emission ist aufgrund der direkten Elektron-Loch-Rekombination in der entspannten Quantenpunkte. Die Wirkung von Al wird untersucht auf die energetische Bandausrichtung und auf die elektronische Struktur der (Al,Ga)As Quantenstrukturen. Die optische Spektren zeigten einen blaue Verschiebung (engl. blue shift) mit wachsendem Al-Inhalt und die höchste Emissionsenergie für die (Al,Ga)As/GaP-Heterostruktur war 2.17 eV die zum indirekten Typ-II-Rekombination zusammenhängt.

Stichwörter: III-V Halbleiter, GaP, AlGP, GaAs, AlGaAs, Wachstumstemperatur, PH_3 Fluss, Quantenpunkte, Gitterfehlanpassung, Lumineszenz.

Chapter 1

Introduction

The optoelectronic devices can function in applications such as data transportation, displays, information storage, etc. In principle, the optoelectronic devices such as photonic crystal cavities, lasers, and light emitting diodes convert and transmit the achieved signal as the photonic waves. Design, growth, and investigation of the optoelectronic devices based on the III–V semiconductors on GaP (001) substrate are the main goals of this thesis.

GaP is an indirect semiconductor with a large bandgap energy [1, 2]. The large bandgap energy of GaP makes it a transparent semiconductor in most part of the visible wavelengths. This, in turn, can cause the easier extraction of the emitted light from the optoelectronic devices based on GaP in the visible range. On the other hand, several attempts were done on monolithic integration of III–V optoelectronic devices with silicon. Among the III–V semiconductors, GaP has the closest lattice constant with Si (lattice mismatch is less than 0.4%). This small lattices mismatch may lead to the growth of the high-quality GaP on Si. Therefore, GaP can be considered as a promising material for the monolithic integration devices with Si. Several investigations were done on the heteroepitaxial growth of GaP on Si and recently, fabrication of optoelectronic devices such as solar cells and light emitting diodes on GaP/Si were reported [3, 4, 5, 6]. The indirect bandgap energy, however, makes GaP an inefficient light emitter. The challenge of high–efficiency light emitter based on GaP was approached by exploring the use of epitaxial quantum structures embedded in this material. Direct electron–hole recombination within the GaP matrix using III–V nanostructures permits high quantum efficiency.

The growth of high-quality structure of semiconductors on GaP, therefore, is an essential point for the fabrication of high-efficiency light emitters based on GaP. Among the several growth techniques [7, 8, 9], I used gas–source molecular–beam epitaxy (GSMBE) to grow the desired structures.

This thesis is divided into 8 chapters. This chapter is an overview of the all discussed contents in this thesis. Chapter 2 includes a brief introduction about MBE crystal growth method and particularly, GSMBE growth technique. GSMBE is applied in an ultra high vacuum environment that provides the possibility of the *in situ* monitoring of the surface during the growth. The possibility of *in situ* monitoring

reduces many guess works and allows a faster optimization of the growth conditions. The different parts of the Riber–32P GSMBE, the fundamental processes occurring on the surface of the substrate inside the growth chamber, the different growth modes, and the self–assembled growth of the quantum dots (QDs) will be brought up in the next section.

The growth of the desired heterostructures is the first step of the fabrication of the optoelectronic devices. The second step is the characterization of the features of the grown heterostructure. In chapter 3, the experimental characterization methods that I utilized to investigate the grown structures will be explained. In that chapter, the characterization methods are sorted into two categories of structural and optical methods. The reflection high–energy electron diffraction (RHEED), high–resolution X–ray diffraction, atomic force microscopy, and scanning electron microscopy are the utilized characterization methods to investigate the structural properties. The optical properties of optical devices are the key points that must be studied and methods such as cathodoluminescence, photoluminescence, and time–resolved photoluminescence were used in this thesis to study the optical properties. These techniques will be introduced briefly in chapter 3.

To analysis and interpret the results of experimental characterizations, a knowledge about the theoretical concepts is needed. Therefore, in chapter 4, the theoretical concepts of the crystal structure and electronic structure of the III–V semiconductors, the heterostructure definition, and its electronic structure will be discussed. Strain and its influence on the characteristic features of the heterostructures, and the theoretical models to determine the band alignment of the strained heterostructures will be introduced. Afterward, the different quantum structures and the effects of the quantum confinement on their properties will be explained.

Chapters 5, 6, and 7 include the data analysis, and interpretations of the experimental and calculation results of the studied samples in this thesis. Photonic crystal cavities are one of the optoelectronic devices with the application such as information processing and data transportation. The so–called photonic bandgap of a photonic crystal is determined by the refraction and reflection of the light from the different interfaces. A photonic crystal, therefore, can be designed and con-

structed with a defined photonic bandgap [11, 12, 13]. GaP is introduced as a good candidate for the photonic crystal cavities with the photonic bandgap at the visible wavelengths. The membrane of GaP can be produced using a sacrificial AlGaP layer. The quality of the GaP membrane, however, depends directly on the quality of AlGaP layer [14]. Therefore, optimization of the growth conditions to improve the crystal quality of the AlGaP layer is a key point for the enhancement of the GaP membrane crystal and surface qualities, which can lead to a higher Q–factor. I will bring up the results of the investigations on the influence of the growth temperature and phosphine (PH_3) flux on the structural properties of the epitaxial growth of the AlGaP layer on GaP (001).

The incorporation of photonic crystal cavities with light emitters, and particularly with single–photon light emitters based on QDs is an interesting topic for the investigations [15, 16, 17]. LEDs are, on the other hand, the useful optoelectronic devices that have applications such as data transmission, information storage, and visible displays. The transparent GaP permits the high efficient extraction of the emitted light. Therefore, the self–assembled growth of QDs of the direct bandgap semiconductor is a conducive idea to overcome the inefficient light emission of GaP for applications such as light emitters. GaAs is a well–known direct bandgap energy semiconductor. The lattice mismatch of GaAs with GaP (001) is about 3.7%. Therefore, the self–assembled growth of the GaAs QDs on GaP is expected due to the strain driven by the lattice mismatch. In this thesis, I studied the growth of the GaAs QDs on GaP (001) substrate and investigated the structural and the optical characteristics of the GaAs QDs embedded in the GaP matrix. The results of these studies will be discussed in chapter 6. Here, the controllable growth of GaAs QDs that emit light in the range of 1.7 eV to 2.1 eV depending on the size of the QDs will be shown and the light emission of the GaAs/GaP up to room temperature will be presented. The results of my investigations on the influence of the growth temperature and the nominal thickness of the grown GaAs layer on both morphology and optical features will be discussed and I will propose a model to interpret the experimental results based on the theoretical calculations. The results of the initial efforts to fabricate the LED based on the GaAs QDs as the active region in a p–i–n

junction of GaP:Be–GaAs QDs–GaP:Si will be explained in chapter 6. I will introduce the grown structures and the optical emission of the fabricated LED in the range of 1.83 eV to 1.96 eV.

The highest emission wavelength that is achieved from the GaAs/GaP system is at about 2.06 eV and it is attributed to an indirect type–II system of a thin GaAs QW embedded in GaP matrix. Therefore, the emission wavelengths of GaAs/GaP system is still far from the so–called green gap for light emitters. This green gap is still an ongoing challenge. Among the III–V semiconductors, AlAs has the closest lattice constant with GaAs and, therefore, the formation of AlAs QDs is expected due to the strain driven by about 3.7% lattice mismatch. The bandgap energy of AlAs is larger than GaAs and consequently, the shift toward the lower wavelengths (higher energies) is expected for AlAs/GaP system. AlAs, however, is an indirect semiconductor with low emission efficiency. $Al_xGa_{1-x}As$, on the other hand, has a direct bandgap energy for Al content ≤ 0.45. Therefore, $Al_xGa_{1-x}As$/GaP can be an alternative for shifting the bandgap energy toward the higher energy range. In chapter 7, the results of my attempts to engineer the band structure of $Al_xGa_{1-x}As$/GaP to achieve the higher emission energy than 2.07 eV will be summarized. The bandgap energy of the bulk $Al_xGa_{1-x}As$ can be tuned by the content of Al and it increases with increasing the Al content. In chapter 7, I will present the growth, structural, and optical characteristics of $Al_xGa_{1-x}As$ quantum structures embedded in the GaP matrix. The radiative emission of $Al_xGa_{1-x}As$/GaP is related to a thin $Al_xGa_{1-x}As$ QW and it varies in the range of 1.98 eV to 2.17 eV for the nominal content of Al in the range of 0.3 to 0.5 and nominal thickness of $Al_xGa_{1-x}As$ between 1.2 ML to 2.7 ML.

Finally, the conclusion of the investigations will be brought up in chapter 8.

Chapter 2

Gas–Source Molecular–Beam Epitaxy

The first required step to fabricate an optical or electronic device is the proper and high–quality growth of the designed structures of semiconductors. During the last decades, epitaxial growth methods such as molecular–beam epitaxy (MBE), liquid–phase epitaxy (LPE) [7], chemical vapor deposition (CVD) [8, 9], and vapor–phase deposition (VPD) [10] have been developed and enhanced. These developments lead to the possibility of the simple and accurate growth of well designed low–dimensional semiconductor heterostructures.

In this chapter, I describe briefly some features of the growth of heterostructures using MBE. Next section includes the general discussion of MBE. Different vacuum regime is defined in section 2.2 and the description of gas–source molecular–beam epitaxy (GSMBE) is given in section 2.3. Section 2.4 is focused on the fundamental processes in the MBE growth chamber. Finally, in section 2.5, the self–assembled growth of QDs using the MBE method will be explained.

2.1 Molecular–beam epitaxy

The successful fabrication of the single heterostructure laser of GaAs/$Al_xGa_{1-x}As$ in 1969 [18, 19, 20, 21] using the LPE method was the initial motivation of many studies and investigations on the physics of the epitaxially grown thin films and development of new devices.

The molecular beam epitaxy method, however, was realized initially at Bell Labs and it has been expanded during the last decades of the last century. The particular advantage of this method compared to the other vacuum deposition methods is the possibility to control precisely the growth conditions and the beam fluxes. MBE is known as a growth technique for nanostructures, such as quantum well (QW), quantum dots (QDs), and quantum wires of semiconductors (III–V, IV–VI, nitrides, and oxides), metals, and insulators [22]. In this technique, the growth of the thin crystallized films or nanostructures occurs through the reactions between two or several molecular or atomic beams on the surface of a heated crystalline substrate within an ultrahigh vacuum system. One monocrystalline or so called one monolayer (ML) is denoted as an epilayer. The growth of the epilayer is associated with the physical and chemical reactions between the atoms or molecules of the

constituent elements with the substrate atoms. In MBE method, the relative arrival rates of the constituent elements and dopants are responsible for determining the composition and doping level of the grown epilayer. The arrival rate of the molecular or atomic beam, in turn, is specified by the evaporation rates of the appropriate sources [21, 23]. MBE method is usually classified based on the difference of the applied sources for the elements and it might be classified into four essential groups of solid–source MBE (SSMBE), gas–source MBE (GSMBE), metal–organic MBE (MOMBE), and hybrid–source MBE (HSMBE).

Since MBE growth is done within the high vacuum environment, the growth conditions are far from the thermodynamic equilibrium. Consequently, the kinetics of the surface processes govern the growth. The surface kinetic processes are defined as all the possible reactions between the impinging beams and the outermost atomic layers of the crystalline substrate. In contrast to the non–equilibrium growth of MBE, the other growth approaches, such as LPE and VPD, are carried out at near thermodynamic equilibrium conditions. The diffusion processes, which occur in the crystallizing phase surrounding the crystalline substrate, control the growth using VPD and LPE growth [21].

The high vacuum environment provides the possibility of the *in situ* monitoring of grown surface in MBE method. Surface characterization methods such as reflection high–energy electron diffraction (RHEED) [21, 24, 25, 26], Auger electron spectroscopy (AES) [27], ellipsometry [28], and optical reflectance anisotropy spectroscopy (RAS) [29] are used to control and analysis the grown surface. The ability to control and analysis the structure during the growth can eliminate many of guesswork in MBE and, consequently, enable the fabrication of the high–quality structures using this technique.

2.2 Ultra–high vacuum environment

The vacuum systems, in which the growth of the thin film is carried out, can be sorted into two categories:

- High vacuum (HV), where the residual gas pressure is in the interval of $1.33\times10^{-7} \leq p \leq 1.33\times10^{-3}$ Pa ($10^{-3} - 10^{-9}$ Torr).

- Ultra–high vacuum (UHV), where the residual gas pressure is less than 1.33×10^{-7} Pa or 10^{-9} Torr [21, 23, 30].

A combination of several types of vacuum pumps whit different pressures working range is required to achieve the UHV condition. Fig. 2.1 shows the performance range of different types of pumps [31].

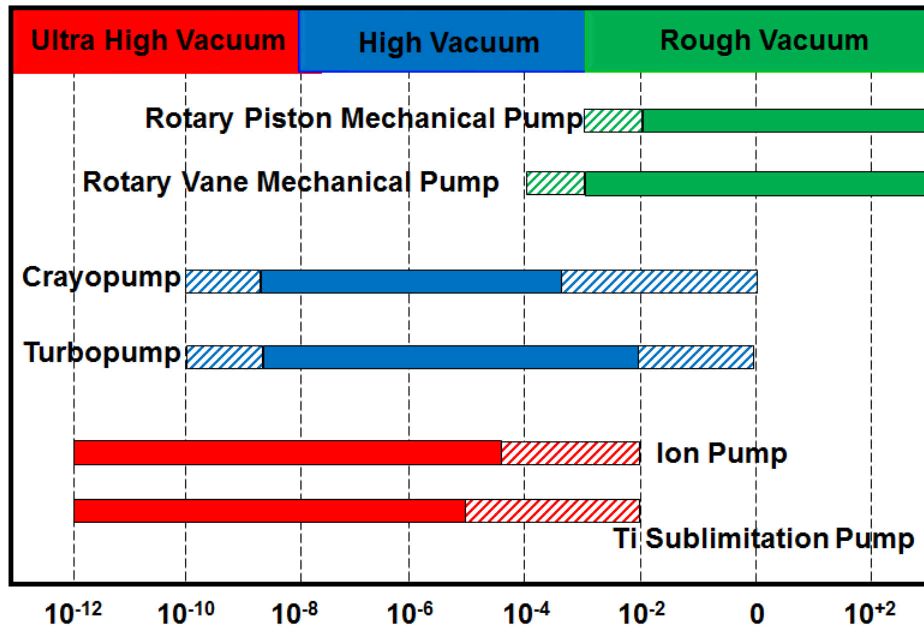

Figure 2.1: Performance range of different pumps in UHV system. A combination of several pumps is needed to achieve the UHV regime [31].

In the standard MBE growth chambers, the molecular beam is generated by the effusion cells or gas inlets. The produced molecules must travel approximately 0.2 m, which is the distance between the effusion cells and the substrate. Therefore, under the low vacuum environment, the molecules can encounter to the residual molecules and scatter. Consequently, the pressure of the residual molecules in the growth chamber ($P_{i,max}$) for the low growth rate (1 μm/h) is needed to be less than 1.7×10^{-9} Pa. This means that for the low growth rate, MBE growth must be carried out in an ultra–high vacuum environment.

In the MBE vacuum system, the residual gas pressure, which can be achieved, is in the range of low–10^{-8} Pa to mid–10^{-9} Pa [21]. These values increase during the growth due to the heated effusion cells and substrate. Although, the achievable

pressure is higher than 1.7×10^{-9} Pa but, it is still possible to produce highly clean thin films using MBE. The small sticking coefficient of the residual gas species on the heated substrate is the origin of this fact [21].

2.3 Gas source MBE

The gas source for the group V elements was a striking innovation in the path of the evaluation of MBE technology in the 1980s. The first and simplest form of the GSMBE or HSMBE method was introduced in 1980. In this method, similar to the conventional MBE, the atomic beam of group III elements are generated using the evaporation of elements in the effusion cells, however, the elements are replaced by hybrids as the group V sources. Thus, decomposition of Arsine (AsH_3) and Phosphine (PH_3) generate the group V elements [20, 21].

I used a Riber–32P GSMBE system to grow the structures. This system consists of two UHV chambers (Fig. 2.2). The first chamber is called the intro–chamber (IC) where the mounted substrates on the molybdenum holders are loaded into the system. Here, substrates are baked at a temperature about 200 ^{o}C to evaporate the water molecules. The second chamber is named the growth–chamber (GC) and the important parts of MBE growth are located in this chamber. These parts are:

- Beam sources (cracking cell and the Knudsen–effusion–cells) and their individual shutters.
- Sample holder with the heater.
- RHEED system, which consists of the electron gun and the fluorescent screen
- Quadrupole mass spectrometers
- Ion gauges to control the pressure of chamber
- Pyrometer

The five Knudsen–effusion–cells are connected to GC. Three of them contain the elements of group III (aluminum (Al), gallium (Ga) and indium (In)), and the other two contain the dopant elements, silicon (Si) from group IV as the n–type

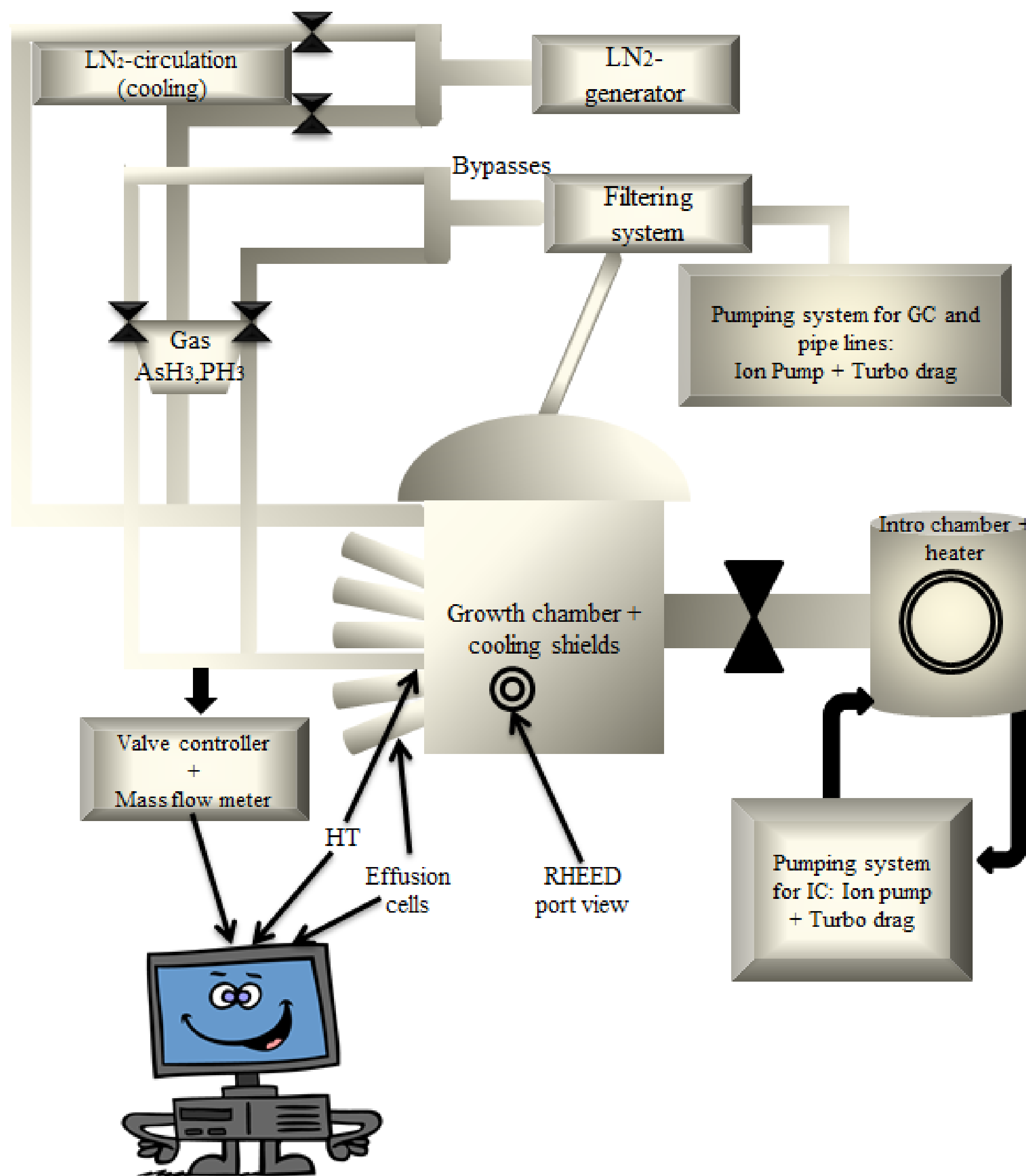

Figure 2.2: Scheme of the Riber–32P gas source molecular beam epitaxy. Growth chamber, intro chamber, Gas lines, cooling system, and vacuum system is shown.

dopant and beryllium (Be) from group II as the p–type dopant (Fig.2.2). AsH_3 and PH_3 are the sources for the group V elements and they are cracked by a low–pressure high–temperature cracker to produce the pure elements. The cracking efficiency is higher than 90% when AsH_3 and PH_3 are cracked with the temperatures equal to 830 ^oC and 850 ^oC, respectively [20]. The growth chamber and the effusion cells are surrounded by a liquid nitrogen cooling system to have the minimum residual molecules in the environment. The pyrometer has been calibrated for GaAs and

it measures the substrate radiation temperature. To improve the uniformity of the grown structure, a motor is responsible for rotating the substrate holder during the growth.

2.4 The physics of MBE growth

Fig. 2.3 illustrates the fundamental parts of an MBE growth including the effusion cells, the heating block, and the substrate. The growth environment can be divided into three zones in which different physical phenomena occur.

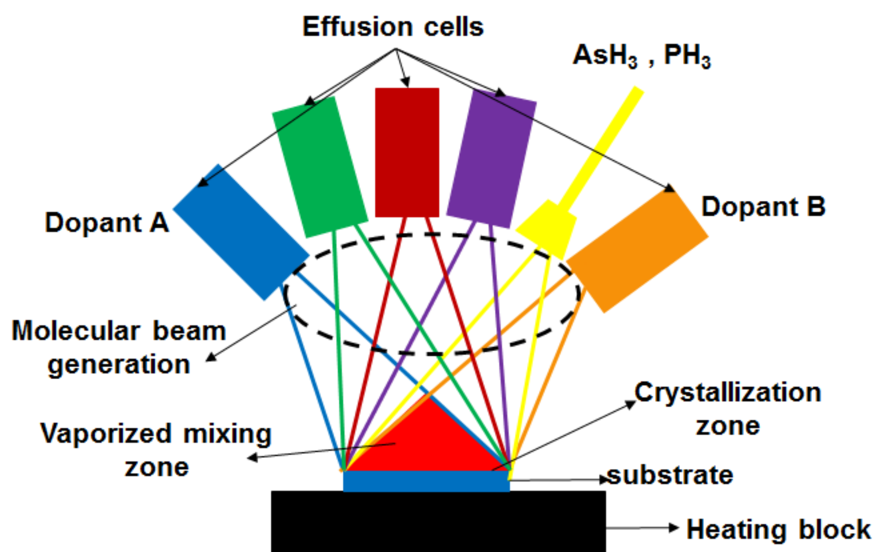

Figure 2.3: Different zones inside GC of MBE. Dash line zone is the molecular beam generation zone, the red zone illustrates the vaporized element mixture region, and the blue zone over the substrate is the crystallization zone.

1) The mixture beams zone that is located close to the effusion cells. It is also called molecular beam generation zone. Here, molecular beams are generated under the UHV condition using the Knudsen–effusion–cells [20, 21]. Temperatures of these cells are controlled precisely using the proportional–integral–derivative controllers (PID) and thermocouple feedback. This provides a flux stability of better than $\pm 1\%$ [20, 21, 33].

2) The vaporized zone, in which a mixture of vaporized elements is formed and a particular gas phase is created over the substrate. Since, the mean free

path of molecules of different intersecting beams are longer than the distance between the sources and the substrate, no collision or interaction exist between the molecules and, therefore, the occurring physical phenomena in the second zone is not well–known [20, 21].

3) The crystallization zone is located on the substrate where the crystallization processes take place. Later, the occurring physical phenomena in this zone will be discussed.

The uniformity in the thickness and also in the composition of the grown film using MBE, depend on the beam fluxes uniformity and the configurations of the substrate and sources. It is often very difficult to have a proper configuration of sources–substrate. Therefore, to have a better uniformity, the substrate is rotated around the axis normal to its surface with a constant angular velocity. The substrate rotation significantly optimizes the uniformity of the thickness and composition of the grown film [21, 34].

2.4.1 Surface and epitaxial growth

The crystallization of the grown epilayer in MBE occurs on the surface of the substrate. This is the third zone of the three fundamental zones of the growth processes that were introduced in the previous section. The first important processes that occur on the surface during the MBE growth is adsorption of the constituent impinging atoms or molecules on the surface of the substrate. Then, the migration of adsorbed atoms or molecules happens on the surface. Afterward, atoms or molecules incorporate to the crystal lattice of the substrate or already grown epilayer, and finally, thermal desorption of the molecules or atoms, which did not incorporate to the crystal lattice, occur [21]. The crystal surface is composed of the crystal sites that are formed by the vacancies or dangling bands, step edges and etc. Fig. 2.4 shows the interactions between the impinging atoms or molecules and the surface of the substrate through the crystal sites [21]. To explain the surface processes qualitatively, it is necessary to define the kinetic parameters. The impinging or arrival rate (r) of the atoms or molecules to the surface is a kinetic parameter that determines the number of atoms or molecules reaching the unit area of the surface

per second. This rate depends on the temperature of the source, T_i, mass of the impinging particle, M, and the vapor pressure of the impinging element, p_v. Therefore, the rate can be written as below [21]:

$$r = \frac{p_v}{\sqrt{\frac{2}{\pi M k_B T_i}}} \tag{2.1}$$

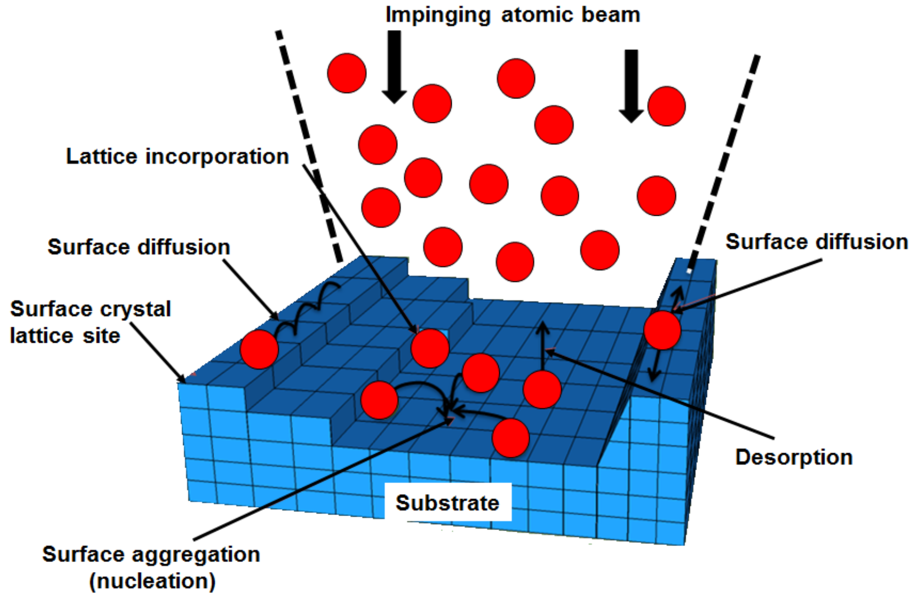

Figure 2.4: The physical processes over the substrate surface in the MBE growth chamber. The impinging atoms can incorporated with the lattice site of the substrate, diffuse over the substrate, or evaporate from the substrate [21].

The particles arrive at the substrate with the energy distribution proportional to the temperature of the effusion cell, T_i. This temperature is usually higher than the temperature of the substrate, T_s. Therefore, the particles can re–evaporate while carrying the energy corresponding to the temperature of T_e. The arriving molecules or atoms may also exchange energy with the atoms of the substrate until they reach the thermodynamic equilibrium with the substrate. Thermal accommodation coefficient can describe this process quantitatively as [21]:

$$a_T = \frac{(T_i - T_e)}{(T_i - T_s)} \tag{2.2}$$

In fact, accommodation coefficient defines how the arriving particles reach the thermal equilibrium to the substrate. It is noteworthy that the accommodation coef-

ficient differs from the sticking– or condensation–coefficient. The latter is defined as the ratio of the number of the atoms that adhere, to the number of the atoms that arrive at the substrate [21]:

$$s = \frac{N_{adh}}{N_{tot}} \tag{2.3}$$

The sticking coefficient is often less than unity, particularly in the case that the surface temperature is very high or the adsorption energy of the arriving atoms is low. However, even when all the arriving atoms are in a thermal equilibrium with the substrate, $a_T = 1$, it does not mean that they will remain on the surface permanently. They have a finite probability, to overcome the binding energy to the surface and leave it. This probability depends on to the surface temperature. Therefore, the sticking coefficient can be zero even under the conditions that the accommodation coefficient is unity. Consequently, if the condensation does not happen on the surface, all the arriving atoms will be evaporated [21]. The absorption of the arriving atoms is classified into tow types [21]:

- Physical absorption or physisorption
- Chemical absorption or chemisorption

The interaction potential of physisorbed and chemisorbed atoms are shown in Fig. 2.5 [21]. These two different types of adsorption have two different sticking coefficients. The physical adsorption is the case in which no electron is transferred between the adsorbate and adsorbent. Physisorption is based on the weak van der Waals attractive force. The sticking coefficient of the physisorption, s_p, is independent of the environment because this type of adsorption has a little or no dependence on the orientation or coverage of the surface. The chemisorption, on the other hand, is based on the transfer of the electron between the adsorbate and adsorbent. Therefore, a chemical reaction is done between the arriving atoms and the substrate atoms. The sticking coefficient of chemisorption, s_c, depends on the spatial distribution of already adsorbed atoms and the crystal orientation of the substrate [21].

The interaction potential of the chemisorbed atoms with the surface differs from the interaction potential of physisorbed atoms. Generally, the interaction potential

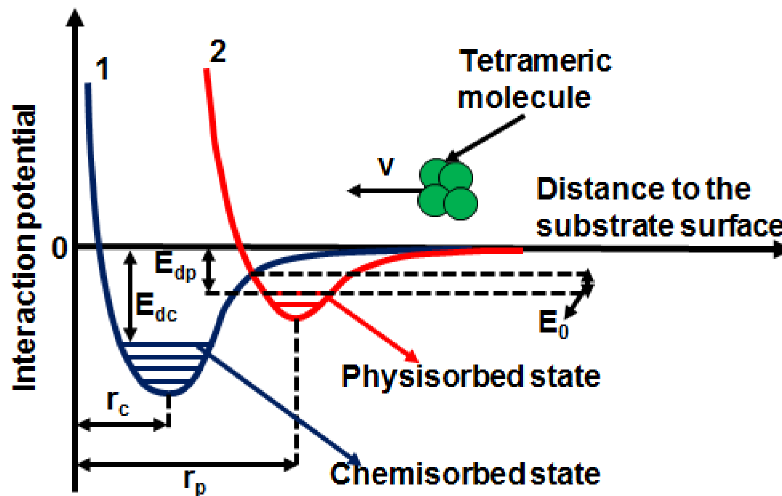

Figure 2.5: The interaction potential of physisorbed and chemisorbed atoms. The physisorbed atoms are interacting with each other through the weak van der Waals attractive force. The chemisorbed atoms make bond through the electron transfer [21].

of the physisorption is less than chemisorption processes. The reason for the less potential of physisorption is that the van der Walls bond, which forms between the adsorbate and adsorbent, is weaker compared to the ionic or covalent bond in the chemisorption. It can be seen in Fig. 2.5 that the molecules in the physisorbed state need to overcome the lower barrier for re–evaporating to the vacuum compared to the molecules in the chemisorbed state [21].

2.4.2 Surface growth modes

Crystal growth mode can be distinguished in three different modes.

- layer by layer or Frank–van der Merwe (FM) growth mode
- Volmer–Weber (VW) growth mode
- Stranski–Krastanov (SK) growth mode

Fig. 2.6 shows these different modes. Formation of each mode directly depends on the surface– and interface–energy and also the lattice constant of the grown material and substrate. Later defines that whether the growth is a lattice–matched or a lattice–mismatched growth mode.

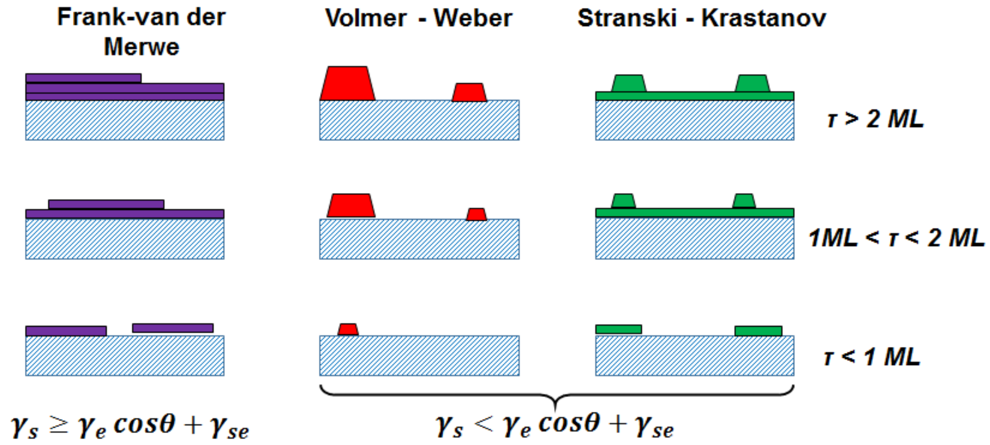

Figure 2.6: Three different growth modes. Formation of each mode directly depends on the surface– and interface–energy and also the lattice constant of the grown material and substrate.

In the lattice–matched mode, the lattice constant of the grown epilayer is equal or very close (less than 0.03 %) to the lattice constant of the substrate and, therefore, there is no or negligible strain at the interface. Under this condition, the surface, and the interface energies determine the growth mode. In a lattice–mismatched growth mode, however, the grown epilayer and the substrate have different lattice constant. Thus, the strain also participates in the determination of the growth mode[20, 35, 36]. Gibbs free energy at the interface of the substrate and the grown epilayer determines the different growth modes. At the interface, Gibbs free–energy is written as [37]:

$$G = E_e + E_{se} \tag{2.4}$$

where E_e and E_{se} are the energy of the epilayer and energy of the substrate–epilayer at the interface, respectively. Since tension is defined as the energy per unit length, then we can rewrite the previous equation as:

$$\gamma_s = \gamma_e \cos\theta + \gamma_{se} \tag{2.5}$$

Where γ_s is the substrate–surface tension, γ_e is the epilayer–surface tension, γ_{se} is the epilayer–substrate interface tension and, θ denotes the angle between the grown epilayer and the substrate (Fig. 2.7).

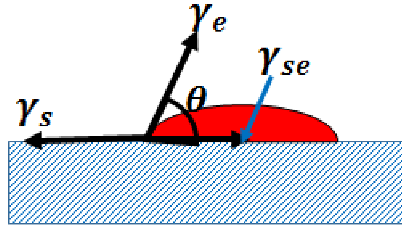

Figure 2.7: Tension at substrate, surface, and epilayer. γ_s is the substrate–surface tension, γ_e is the epilayer–surface tension, γ_{se} is the epilayer–substrate interface tension and, θ denotes the angle between the grown epilayer and substrate [37].

The layer–by–layer or FM growth mode happens when:

$$\gamma_s \geq \gamma_e \cos\theta + \gamma_{se} \tag{2.6}$$

Here, the atoms are more strongly bond to the substrate than to each other, and therefore, the first atoms condense in the form of a complete layer on the surface and then will be covered by the less tightly bond second layer. This type of growth mode is observed in the growth of the lattice matched materials with the substrate [35, 36, 37, 38].

In the case of:

$$\gamma_s < \gamma_e \cos\theta + \gamma_{se} \tag{2.7}$$

islands growth is favorable. In the VW growth mode, small clusters are nucleated directly on the substrate surface and the growth will be followed by the formation of islands. This growth mode arises when the atoms or molecules of the grown material are more strongly bonds to each other than to the substrate [37, 38].

The other growth mode with island formation is the SK growth mode, which is an intermediate growth mode. In the SK growth mode, the first– or few–monolayers are grown as a two–dimensional (2D) strained layer on the surface of the substrate. This 2D strained layer is also known as the wetting layer (WL). For a thicker layer than a critical thickness, however, the layer growth mode is unfavorable due to the increase of the strain between the grown epilayer and substrate. Therefore, the strain is released by the formation of islands. In this mode, QDs, which are defined as

the coherently strained three–dimensional (3D) islands, are formed self–assembly [38, 39, 40].

2.5 Growth of quantum dots in self–assembled mode

For the first time, Staranski and Krastanov reported the evaluation of the initially 2D growth into the 3D islands. In their paper in 1937, they proposed the possibility of the formation of islands on the initially flat heteroepitaxial layer for the lattice–matched ionic crystal which has different charges [21]. Later, the SK growth mode was used to explain the formation of three–dimensional islands on a two–dimensional strained layer [39, 40]. These islands can be relaxed with misfits–defects. The formation of coherent islands (defect free) in the SK growth mode is a concept that is highly used for the growth of self–assembled QDs. The SK growth mode is the dominant growth mode for a strained epilayer with small interface energy. In such a system, the few first monolayers growth is carried out in the layer–by–layer growth mode but, for a thicker layer, strain increases strongly. One mechanism that can reduce the strain is the formation of islands that might be coherently strained [45].

The elastic relaxation depends strongly on the shape of the islands. For a given shape, elastic relaxation is proportional to the volume of the islands. Fig. 2.8 shows two islands with different height/width ratio. A QD with a small height/width ratio is a non–relaxed while, a QD with the large height/width ratio is almost completely relaxed. The volume relaxation mechanism competes with the formation of dislocations in the strained layer.

The morphological phase diagram of a mismatched system is determined by the variations of the surface energy due to the formation of islands (ΔE_{surf}), the dislocated surface energy (E_{inter}^{disl}), and the ratio of them ($\Gamma = (E_{inter}^{disl}) / (\Delta \mathrm{E}_{surf})$). Fig. 2.9 illustrates that for the large amount of ΔE_{surf} or small E_{inter}^{disl}, where Γ is smaller than Γ_0 the formation of coherent islands is not favorable while for the opposite condition where $\Gamma > \Gamma_0$, the increase of the grown material quantity is followed by the formation of coherent islands. The coherent islands, however, have a critical size which is determined by the total energy of the islands. This total

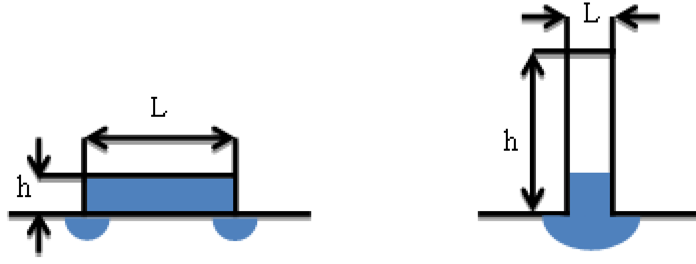

Figure 2.8: The elastic relaxation for a given shape depends on the height/width ratio. For a non–relaxed QD this ratio is small (a) and it is large in the case of a relaxed island.

energy is given as [38, 41, 42]:

$$E_{island} = E_{edges} + (\Delta E_{surf}) - E^{V}_{relaxation} \tag{2.8}$$

Here, E_{edges} is the short–range energy of the island edges and $E^{V}_{rlaxation}$ is the elastic relaxation of the strained volume caused by the lattice mismatch.

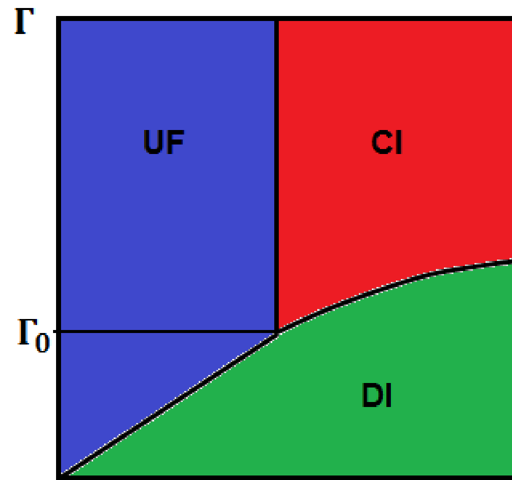

Figure 2.9: The morphological phase diagram of a mismatched system. In the case of $\Gamma < \Gamma_0$ non–coherent islands are generated while the formation of the coherent islands is predicted for $\Gamma > \Gamma_0$ [38, 44]. Here, UF, DI, and CI denote the uniform film, non–coherent islands, and coherent islands, respectively.

We can write these energies based on the size of the islands (L) and rewrite them as [38, 41, 42]:

$$E_{edges} = AL, E_{surf} = BL^2, E^{V}_{relaxation} = CL^3 \tag{2.9}$$

For a positive ΔE_{surf}, the critical size of islands is derived from [41]:

$$\frac{dE_{island}}{dL} = 0 \tag{2.10}$$

and when surface energy dominates over the short–range edges energy, L_{crit} will be [41]:

$$L_{crit} = \frac{2B}{3C} \tag{2.11}$$

In the case of larger sizes than L_{crit}, the coherent islands undergo with Ostwald ripening. Consequently, this causes the growth of large islands and appearance of the dislocations [38, 43, 44, 42].

Chapter 3

Experimental characterization methods

The development of high–resolution measurements in addition to the accurate analysis methods enable us to study, understand and interpret the behavior of quantum heterostructures. In this chapter, the different characterization methods that I used to characterize and study the grown samples for this project. The characterization methods are sorted in two classes of the structural and optical characterizations. Section 3.1 is concentrated on the different approaches for the structural characterization while in section 3.2 the principals of the optical measurements will be discussed.

3.1 Structural characterization methods

Reflection high–energy electron diffraction (RHEED), x–ray diffraction (XRD), atomic force microscopy (AFM), scanning electron microscopy (SEM), and transmission electron microscopy (TEM) were utilized to characterize the structural properties. RHEED and XRD indirectly provide the information from the structure, while AFM, SEM, and TEM give the direct information of morphology. The first two methods use the reciprocal lattice to obtain the information but in the case of the direct measurements, the structural images of real space are collected.

3.1.1 Reflection high–energy electron diffraction (RHEED)

RHEED is an *in–situ* real–time diffraction method that is used to study the surface structure, the surface quality, and the growth rate during the MBE growth. This method is based on an incidence electron beam with energy in the range of 10–50 keV that glances to the surface with a small incidence angle of 1–3°. The electrons penetrate only the first few monolayers of the material because of this small incident angle and, therefore, RHEED method is highly sensitive to the surface. The reflected electrons incident on the fluorescent port view and provide the possibility of studying the surface in real time. These advantages, however, are together with the requirements that are produced by UHV and design of the MBE growth chamber [25]. In this work, a 10 keV electron beam was used.

RHEED is an accurate method to determine the growth rate. The growth rate is characterized using the intensity oscillations of the RHEED pattern. These oscilla-

tions may be explained by the monolayer growth of the material on a flat substrate in a layer–by–layer growth mode. Accordingly, the frequency of the oscillations is associated with the monolayer growth. The RHEED pattern of a flat substrate has the highest intensity at the beginning of the growth. The intensity, however, decreases due to the formation of islands during the nucleation of next layer. The intensity increase again when the layer is finished and the islands coalesce into a flat layer. Consequently, the intensity oscillation is related to the roughness oscillation because of the atoms nucleation during the growth. Fig. 3.1 indicate the growth mechanism associated to the RHEED intensity oscillation [25].

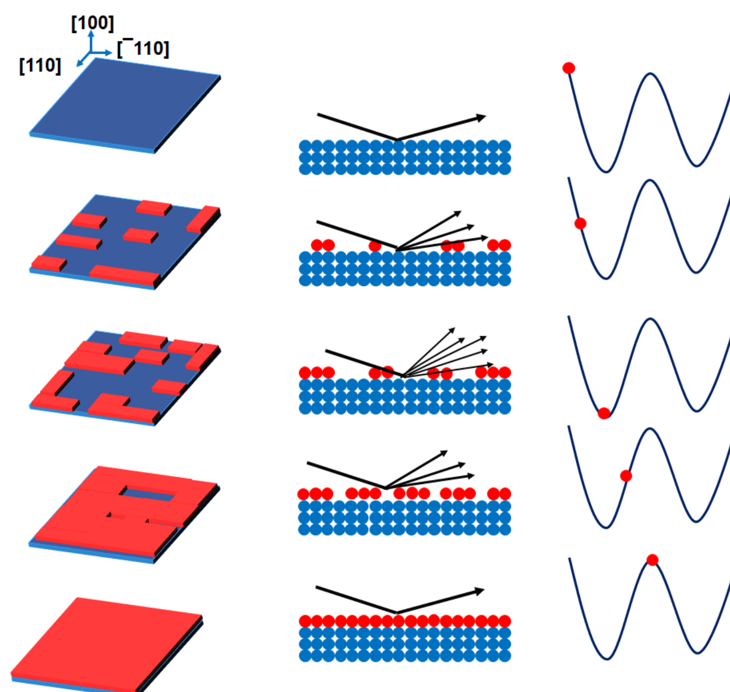

Figure 3.1: Scheme of the growth mechanism associated to the RHEED intensity oscillation. The maximum intensity is related to the beginning of the growth and when one atomic layer growth is finished [25].

3.1.2 High resolution X–ray diffraction

High–resolution X–ray diffraction (HRXRD) is the method that I used in this project to characterize the crystal properties of the grown samples. Using this method, one can determine the composition and thickness of a grown layer. Consequently, it is possible to indirectly determine the growth rate of the grown layer.

This measurement is also a powerful method to study the crystal quality of the grown layer, according to the investigations on the defects and determination of the density of dislocations. The mismatch, relaxation, and misorientation are the other parameters that can be determine using the HRXRD.

The X–ray spectrum can be provided using the highly energetic particles. If a 3D array of atoms coherently scatters a plane wave such as X–ray waves, then the diffraction occurs. Consequently, a concerted constructive interference is produced at a specific angle. This is known as the Bragg$^{'}$s law [46]:

$$n\lambda = 2dsin\theta \tag{3.1}$$

where, n is an integer that denotes the order of diffraction, λ is the wavelength of the incident wave (in our case it is fixed), d is the distance between each crystal plane and, θ is the incident angle (Fig. 3.2). Therefore, the Bragg$^{'}$s peak is determined by a family of planes at only a specific angle and the distance between different diffracting atomic planes specifies the peak position [46]. The absorption factor is

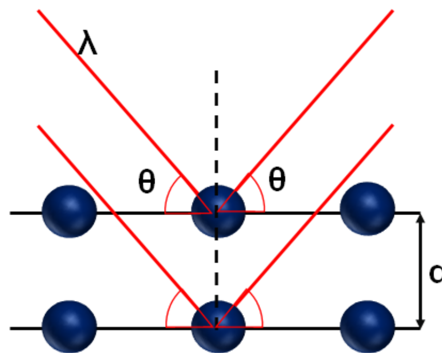

Figure 3.2: Diffraction of a plane wave from the crystal plane. The constructive interference of diffracted waves occurs when the Bragg's law is satisfied [46].

small for the X–ray wave and, consequently, the penetration length is large and the rocking curves (X–ray peaks) of the diffracted waves are narrow. This means that the X–ray measurement is sensitive to the strain because any small rotation caused by the strain can strongly broaden the rocking curves [47].

In HRXRD method, measurements are usually carried out as a function of ω and/or 2θ. ω, which is the incident angle of X–ray, is defined between the X–ray

source and the sample. The diffraction angle, 2θ, is distinguished between the incident beam and the detector angle (Fig. 3.3). The HRXRD measurement, therefore,

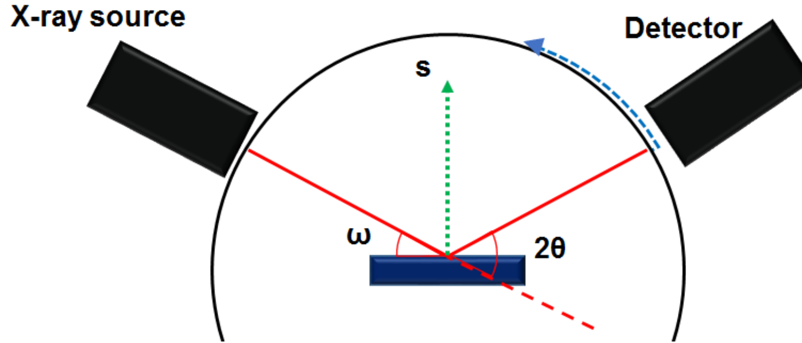

Figure 3.3: The scheme of a X–ray source, sample, and detector. The incident angle between the X–ray source and the sample is ω, while the angle between the incident beam and the detector is defined as 2θ [47].

can be sorted based on these angles[47]:

- Rocking curve scan that the X–ray intensity is plotted with respect to ω.
- Detector scan that the ω does not change and the X–ray intensity is plotted versus 2θ.
- Coupled scan in which the X–ray intensity is plotted versus 2θ but the ω also changes. The change of ω is linked to 2θ as $\omega = \frac{1}{2}2\theta$ + offset.

In this project, I used the detector scan or so–called $\theta/2\theta$ scan to study the samples. In this method, the relative angle is scanned with a 1:2 ratio between the incident X–ray beam to the sample and detector [48].

X–ray pattern is used to characterize the thickness of the grown layers. In this case, the angular distance between the firings obtained from the X–ray pattern is applied to calculate the thicknesses of the epitaxial layers [49].

$$D = \frac{\lambda|\gamma_h|}{\Delta n sin(2\theta)} \tag{3.2}$$

Where, λ is 1.541 Å, Δn is the angular space between the fringes, $\gamma_h = sin(\alpha + \theta)$, and α is the angle between the crystal surface and reflection plane. For a high

quality and flat substrate, it can be considered that the angle between crystal surface and reflection plan is negligible ($\alpha \simeq 0$), so that:

$$D = \frac{\lambda}{\Delta n cos(\theta)} \tag{3.3}$$

Strain is the other feature that can be determined using the X–ray pattern. In the case of a pseudomorphic grown layer, strain along the growth direction can be calculated using the angular space between the substrate peak and the associated peak of the epitaxial layer ($\Delta\omega$). The strain along the growth direction is then [49]:

$$\varepsilon_{zz} = \frac{\Delta d}{d} = \frac{2\Delta\omega}{2tan(\theta)cos^2(\alpha) + sin(2\alpha)} \tag{3.4}$$

Since, $\alpha = 0$, then the last equation is reduced to:

$$\frac{\Delta d}{d} = \frac{2\Delta\omega}{2tan(\theta)} \tag{3.5}$$

It is also possible to specify the composition of the grown layer. Δa, the difference between the lattice constant of the grown material and the substrate is calculated from 3.5:

$$\frac{\Delta a}{a} = \frac{\Delta d}{d}\{\frac{1-\nu}{1+\nu}\} \tag{3.6}$$

where a is the lattice constant of the substrate, and ν is the Poisson ratio.

Now, using the Vegard$^{'}$s law, which states that the lattice constants of substitutional solid solutions vary linearly between the values for the components, the composition of the epitaxial layer can be determined as follow:

$$a_{A_xB_{1-x}} = xa_A + (1-x)a_B \tag{3.7}$$

The X–ray pattern is also applied to study the crystal quality of grown epitaxial layer. The density of the dislocation defects is a feature that can be determined using the X–ray pattern. According to the Hirsh's model, N, density of dislocation defects, is [50]:

$$N = \frac{\beta^2}{9b^2} \tag{3.8}$$

Here, β is full width at the half maximum (FWHM) of the epitaxial layer peak and b is the Borger$^{'}$s vector.

3.1.3 Atomic–force microscopy

Although the opto–electrons microscopes are powerful equipment for surface characterization, they only function on the plane horizontal to the surface of the sample. Consequently, the produced images using these methods do not provide any information about the vertical dimension of the surface. On the other hand, AFM does not utilize the electromagnetic radiations to create an image. Instead of the photons or electrons, AFM measures the 3D topography of a surface with a sharp probe (Fig.3.4(a)) [51].

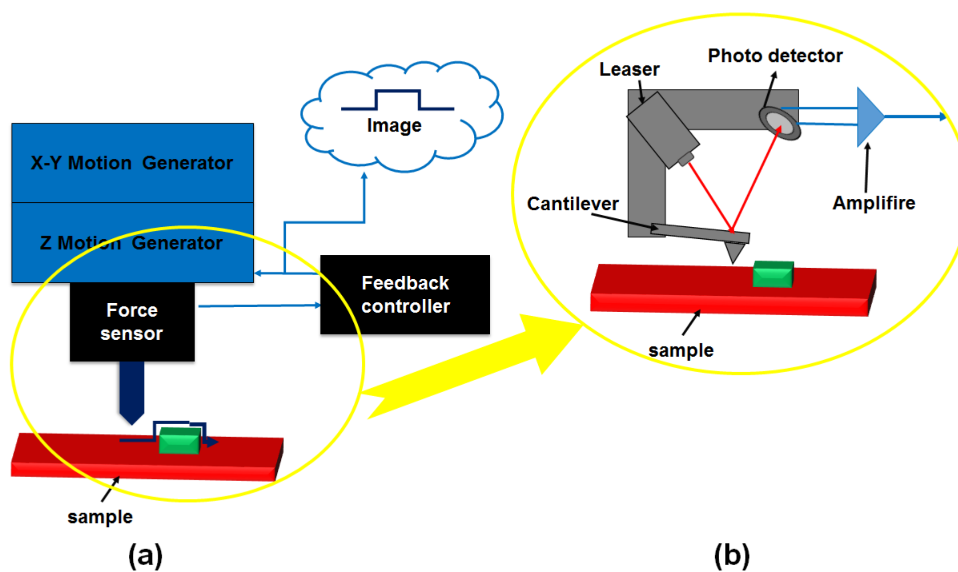

Figure 3.4: (a) Principle of AFM topography scan of the surface. (b) Interactions between sharp probe and surface cause different path for the reflected laser [51].

AFM measurement is based on the interaction between the sharp probe and the force fields of the surface. The probe is brought enough close to the surface and scan is done across the surface. Then, the image of the surface is obtained from the precise monitoring of the probe motion. The typical diameter of the probe is less than 50 nm and usually, the scanned areas are less than 100 μm^2. The maximum height which can be scanned using AFM is less than 20 μm and the scan time depends on the size of the scanned area and height of the features. The scan time can vary in the range of some seconds to many tens of minutes. The magnifications that achieved by AFM can be in the ranges of 100 X to 100000000 X along the horizontal (x–y) and vertical axis [51]. Interactions between sharp probe and surface

cause the different path for the reflected laser from the back side of the cantilever. This, in turn, causes the different amounts of the detected light by each section of a photo–detector (Fig.3.4(b)). Finally, the different amounts of the detected light along the z–axis, which are due to the features on the surface, in addition to the motions of the tip along x and y directions, are used to create an image of the surface [51].

The quality of scanned images using AFM directly depends on the geometry of the probe, for instance, if the probe cannot reach the bottom of the surface feature then the image will not present the exact and correct geometry of the sample (Fig. 3.5). In this work, the Si–based probes were used as the cantilevers that have low–level residual stress. This prevents the bending of the cantilever. This type of cantilever is, however, crispy and can easily break if it contacts to the surface. The shape of the Si cantilever is usually conical.

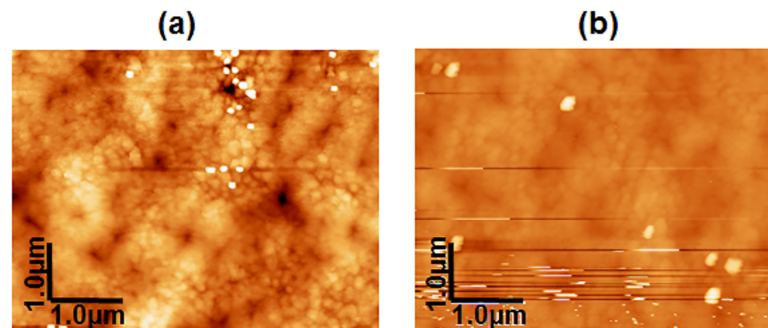

Figure 3.5: AFM images of one sample that were measured(a) using a sharp probe (b) using a broken probe

3.1.4 Scanning Electron Microscopy

The scanning electron microscopy (SEM) measurement is utilized to observe the surface and/or the cross–section of a sample. This approach provides also the possibility to study the optical properties of the sample (more discussion can be found in next section). The topography image of the surface is obtained by a two–dimensional scan of the surface. In this method, an electron beam is applied to scan the surface and then the emitted secondary and/or back–scattered electrons from the sample are collected and sent to the image display [52, 53] (Fig. 3.6).

The electrons are scattered when they reach to the sample. They lose gradually their energy with emitting different signals and finally are adsorbed by the sample. The emitted signals are secondary electrons (SE), backscattered electrons (BSE), Auger electrons, X–ray, and cathodoluminescence (CL) (Fig. 3.7). The different signals require different detectors to be investigated. In this project, however, SE, BSE, and CL signals were used to study the samples. The energy of SE, which are

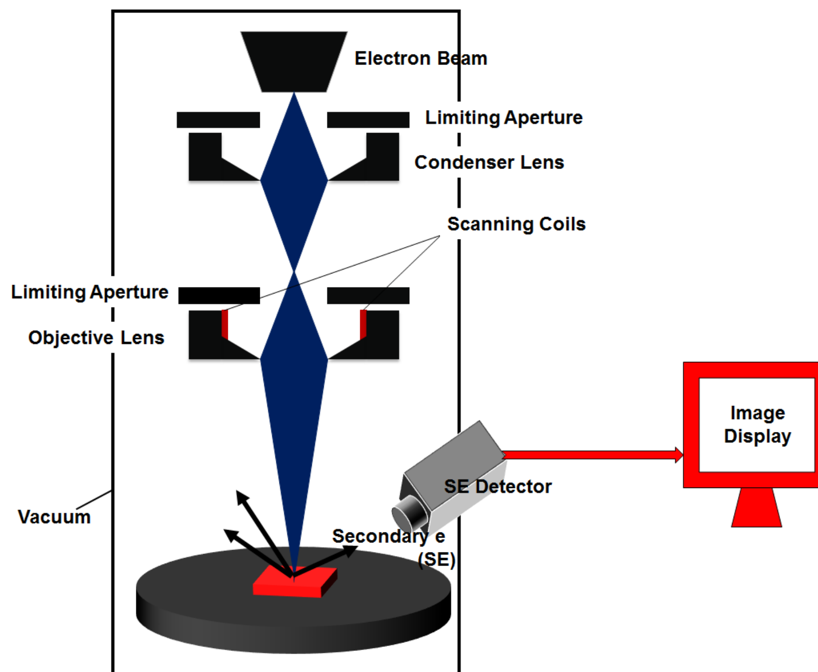

Figure 3.6: Fundamental sections of SEM. Stage, detectors, and optical system are all in a vacuum system. The different parts of the optical system are shown.

generated by excitation of electrons from the valence band of constituent atoms in the sample, is very small. Therefore, the generated secondary electrons at the deep regions are absorbed by the sample while those that are generated on the surface can be scattered. Consequently, the secondary electrons are very sensitive to the surface and can be used to observe the topography of the surface [52, 53]. BSE are those electrons that scattered backward and emitted out of the samples. They have higher energy compared to the SE and, therefore, can produce information about the deeper regions of the sample. These electrons are sensitive to the composition of the sample, thus the area that is composed of the heavier atoms is shown as a brighter area in BSE image [52, 53]. The CL signal is a unique contact–less electromagnetic

signal that can provide the information about the optical properties of the under investigation samples.

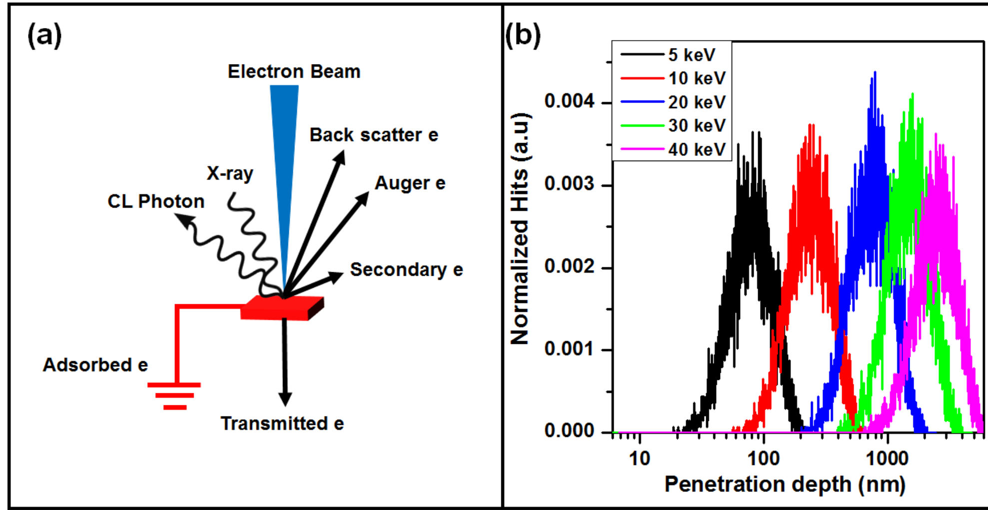

Figure 3.7: Scheme of various electron emission and electromagnetic waves from the sample due to the interaction with the incident electrons [53]. (b) Monte–Carlo simulation of the electron penetration range in GaAs for different electron energies.

The penetration range of the electrons inside the sample, however, depends on the electron energy, atomic number of the constituent elements, and the density of the atoms. The scattering range increase for higher electron energy, while it decreases for larger atomic number and density. Kanaya et al. express the relation between the penetration range and electron energy, atomic number of the constituent, and atomic density as:

$$R_e = \left(\frac{0.0276A}{\rho Z^{0.889}}\right)E_b^{1.75} \tag{3.9}$$

where R_e is the penetration range in μm, A is the atomic weight in g/mol, ρ is in g/cm^3, Z is the atomic number, and E_b is the electron energy in keV [53, 55]. Fig. 3.8(b) indicates the Monte–Carlo simulation of the electron behavior in a bulk GaAs (the simulation was done using the Casino software [56]). Accordingly, the energy (acceleration voltage) dependency of penetration range of electrons is an advantage of SEM method. The higher acceleration voltage may give more information about the deeper region of the sample, but it also causes an unclear image of that region, which overlaps on the surface image. Therefore, depending on the interested information one can do a depth analysis using the SEM method [52, 53].

3.2 Optical characterization methods

A semiconductor is excited into a non–equilibrium state when a certain sort of energy is applied to it. The excited semiconductor may emit photons and this process is called luminescence, which is a characteristic feature of the investigated semiconductor. The luminescence depends directly on the excitation source. The excitation can be provided using an incident light beam (photoluminescence or PL), an energetic electron beam (cathodoluminescence or CL), carrier injection across a junction (electroluminescence or EL), a chemical reaction (chemiluminescence), and etc [53]. In this work, CL, PL, time–resolved photoluminescence (TR–PL) and, EL methods were used to characterize the optical properties of the grown structures. In this section, I will introduce briefly these methods, their excitation sources, advantages, and disadvantages.

3.2.1 Cathodoluminescence measurement

The photoemission mechanism, with different excitation sources, is similar for inorganic semiconductors. Therefore, the obtained results for a sample excited by electron beam (CL) are comparable with the luminescence of the same sample excited by photons (PL). Some differences, however, arise in detail for different excitation sources. CL measurements can be used for depth analysis by changing the electron beam energy, while PL is an excitation energy dependent measurements and, consequently, can provide information about particular emission process by selecting a certain excitation energy. The grown structures in this project mostly consist of different layers (buffer layer, active layer, and cap layer). Therefore, CL measurements are significantly important for providing the possibility of a depth–dependent analysis [53]. Fig. 3.8 presents a scheme of a CL setup. CL measurements are usually carried out in a SEM system which is equipped with a monochromator and a charged–couple device(CCD)(more information about the SEM system can be found in 3.1.4). The CL analysis can be sorted into two categories:

- Image mode: luminescence images or maps of the interested region are displayed.

- Spectroscopy mode: In this case, the spectrum of an interested point of the sample is collected.

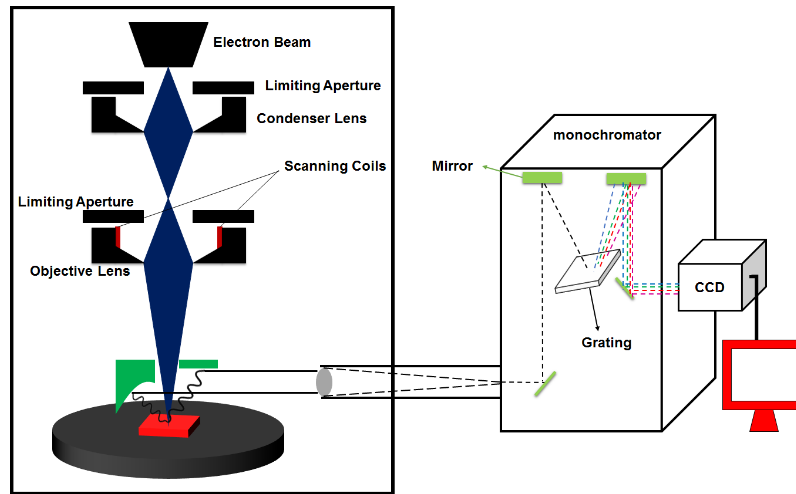

Figure 3.8: Scheme of a CL setup that is composed of a SEM equipped with a monochromator and a CCD.

3.2.2 Photoluminescence (PL) measurement

For a continues–wave (CW)–PL measurement, a CW laser source is needed. This laser source can be provided using a He–Ne, He–Cd, Ar^+ or Kr^+ ion, Nd: YAG, dye, or Ti: Sapphire laser. The laser can be a tunable source or a fixed frequency laser. The frequency (the wavelength), however, must cover the bandgap of the materials that should be investigated [53]. Since the focus of this work is on the materials and structure in GaP matrix, the He–Cd lasers with ultraviolet lines were used to excite the structures. In PL measurements, photons with energy higher than the bandgap energy of the investigated sample excite the electrons from the valence band to the conduction band. The excited electrons, then, rapidly become relaxed via a radiative recombination with the holes in the valence band and emit photons. The emitted photons are dispersed in a monochromator and then they are collected by a photo–multiplier and/or a CCD.

3.2.3 Time–resolved PL measurement

One powerful approach to investigate the carrier dynamic in a semiconductor is the femtosecond spectroscopy. This method has two advantages; first sample prepa-

ration is not required and furthermore, investigation of very fast radiative processes is possible by using a very short laser pulse. Radiative signal detection, however, needs suitable techniques. Streak–camera is the most used technique to detect the photons in the TR–PL measurements. It has high sensitivity to the light with the wavelength shorter than 1200 nm and allows to collect the results quickly. The streak camera boasts a superb maximum temporal resolution of 0.2 ps. A TRPL setup consists of a pulse laser with high repetition rate and excitation wavelength that covers the bandgap of the investigated samples, a trigger section that controls the timing of the streak sweeps, a streak camera, a high sensitive camera and a display [54].

Chapter 4

Semiconductors and quantum dots heterostructures

Characteristic features of a semiconductor device are directly determined by the physical properties of the constituent semiconductors. In this chapter, the fundamental physical properties of III–V semiconductors will be briefly reviewed. Then, to understand the optoelectronic properties of the quantum structures, which are the goal of this work, the fundamental physical properties of QDs and QWs will be described. This chapter is divided into six sections. In section 4.1, crystal structure of III–V semiconductors will be introduced. Section 4.2 contains a brief discussion about the band structure of III–V semiconductors. Section 4.3 is focused on band alignment of heterostructures. Section 4.4 introduces the strain as the origin of the formation of self–assembled quantum dots and the influence of the strain on the band alignment of heterostructures. The effects of low dimension on the electronic substructures of the quantum structures will be discussed in section 4.5. The last section is focused on the fundamental optical features.

4.1 Crystal structure

A crystal is defined as a periodic network of atoms. These atoms are bonded to their nearest neighbored by two electrons with different spins. III–V semiconductors are defined with the zinc blende crystal structure, which can be considered as the two interpenetrating face–centered cubic (fcc) lattices [57, 58, 59, 60]. Fig.4.1(a) shows a zinc blende crystal structure in which one sublattice is occupied by the group III elements atoms, for instance, gallium (Ga), and the other sublattice is occupied by the group V elements, for example, phosphorus (P). Fig. 4.1(b) illustrates the first Brillouin zone of an fcc crystal structure in the reciprocal space, in which Γ represents the center of the k–space, X is located at the center of the rectangular face, and L is the center of the hexagon face of the Brillouin zone.

The binding energy between the group III and V atoms defines the distance between them that is known as the lattice constant. Therefore, the stronger binding energy leads to the less distance between atoms and, consequently, smaller lattice constant and higher band–gap energy. Fig. 4.2 shows the bandgap energy of the III–V compounds with respect to the lattice constant.

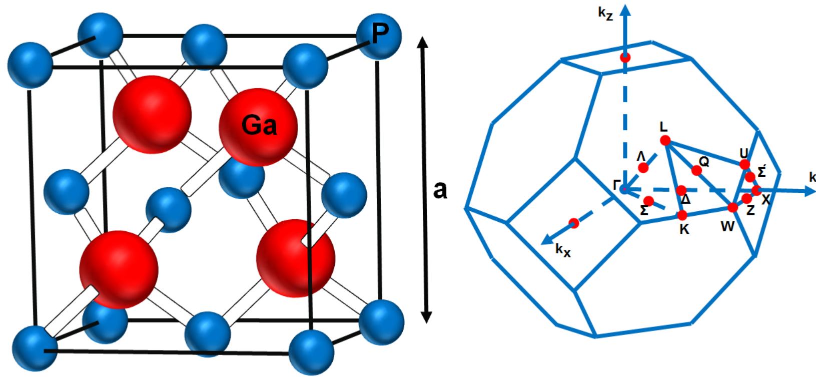

Figure 4.1: (a) Zinc blende crystal structure of the III–V compounds. The blue circles are representative of group V elements and the pink circles show the position of group III elements. (b) First Brillouin zone of an fcc crystal structure in k–space. Different crystallographic points are represented.

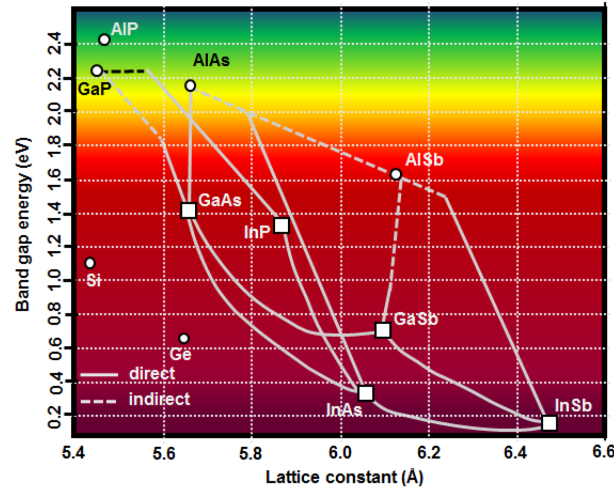

Figure 4.2: III–V semiconductors bandgap energy with respect to the lattice constant. The bold lines indicate the III–V compounds with direct bandgap energy, while the dash lines present the indirect bandgap energy III–V compounds.

4.2 Band structure and energy gap

The band structure of a crystalline solid is the solution of Schrödinger equation. Schrödinger equation can be solved for one–electron as a good approximation when a periodic background potential of $V(\mathbf{r})$ is considered. This periodic background potential is known as the "Bloch′s potential" that has the periodicity of the lattice vector in the real space ($\mathbf{R}$) [62, 63, 64].

$$V(\mathbf{r}) = V(\mathbf{r}+\mathbf{R}) \tag{4.1}$$

Therefore, the solution of Schrödinger equation is a wavefunction with a special form described by the Bloch$^{'}$s theorem.

$$(-\frac{\hbar^2}{2m}\nabla^2 + V(\mathbf{r}))\Psi_{\mathbf{k}}(\mathbf{r}) = E(\mathbf{k})\Psi_{\mathbf{k}}(\mathbf{r}) \tag{4.2}$$

here, m denotes the electron mass. According to the Bloch$^{'}$s theorem, the eigenfunctions of Schrödinger equation for a periodic potential are the product of a plane wave $e^{i\mathbf{k}.\mathbf{r}}$ and a function, $u_k(r)$, with the lattice periodicity:

$$\Psi_{\mathbf{k}}(\mathbf{r}) = e^{i\mathbf{k}.\mathbf{r}}u_{\mathbf{k}}(\mathbf{r}) \tag{4.3}$$

$$u_{\mathbf{k}}(\mathbf{r}) = u_{\mathbf{k}}(\mathbf{r}+\mathbf{R}) \tag{4.4}$$

Therefore, the electron probability is periodic in the lattice with a periodic background potential:

$$|\Psi_{\mathbf{k}}(\mathbf{r}+\mathbf{R})|^2 = |\Psi_{\mathbf{k}}(\mathbf{r})|^2 \tag{4.5}$$

The vector **k** is called **k**-vector and the quantity $\hbar\mathbf{k}$ is known as the crystal momentum. The exact shape of the band structure is calculated by solving the complicated Schrödinger equation taking the exact form of the potential into account. When E is known as a function of **k**, according to the Taylor theorem, the bands can be expanded at the extreme point of k_0 near the bandedges [62]:

$$E(k) = E(k_0) + \frac{\hbar^2}{2m^*}(k-k_0)^2 \tag{4.6}$$

Here, m^* is a constant called the effective mass [62].

The band structure of solids has been studied theoretically by various numerical methods and approximations [62, 63, 64]. According to these studies, the band structure of a semiconductor has a forbidden energy region. Consequently, the allowed energy states are located either above or below of this region. The upper bands are called conduction band while the lower bands are known as the valence band. The energy region between the highest level of the valence band and the lowest level of the conduction band is called bandgap energy (E_g) [62, 63, 64].

The minimum of the conduction band can be located at the center (**k** = 0) or off center of Brillouin zone, along the different **k**–axis (Fig.4.1(b)). Semiconductors

are classified in two types based on the position of the minimum of the conduction band, direct bandgap, and indirect bandgap semiconductors. In the case of a direct semiconductor, the minimum is at Γ (**k** = 0) while for an indirect semiconductor, minimum of the conduction band may be located at L (**k** = 2π/a(1/2 1/2 1/2)) or at X (**k** = 2π/a(1 0 0)). It is notable that for a direct bandgap semiconductor, crystal momentum ($\hbar$**k**) is conserved for a transition from the valence band to the conduction band [57, 58, 59, 60, 62].

Experimental and theoretical results indicate that GaP is an indirect bandgap semiconductor and the minimum of the conduction band is located close to X (Fig. 4.3). Therefore, momentum conservation law is not satisfied for the electron transition from the valence band to the minimum of conduction band [1, 2]. This leads to the very low probability of radiative recombination for GaP.

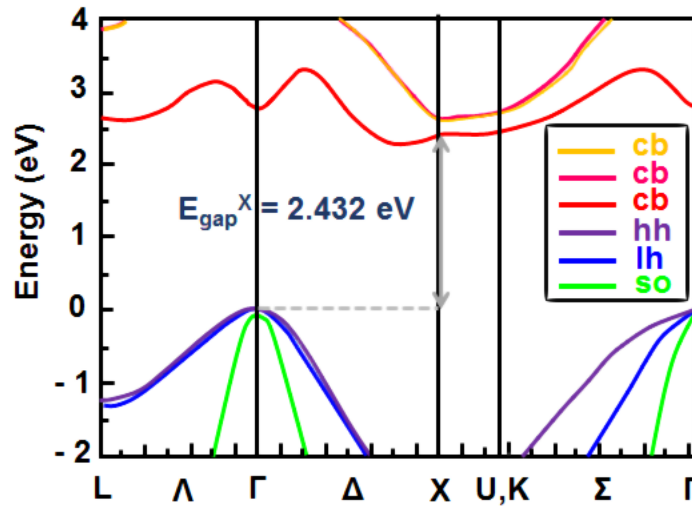

Figure 4.3: Calculated band structure of GaP. The minimum of conduction band is located at X–valley and consequently, GaP is known as an indirect bandgap semiconductor [79].

The lattice constant is a function of temperature and it expands with increasing the temperature. Consequently, the bandgap energy of a semiconductor decreases with the temperature elevation. The relation between the bandgap energy and temperature is given by Varshni model as [64, 65, 66, 67]:

$$E_g(T) = E_g(0) - \frac{(\alpha T^2)}{(T+\beta)} \tag{4.7}$$

Here, $E_g(0)$ is the bandgap energy at 0 K. α and β are two constants that are determined experimentally (The value of α and β for different semiconductors can be found in Appendix.I). Fig. 4.4 shows the variation of bandgap energy versus temperature for GaP [2].

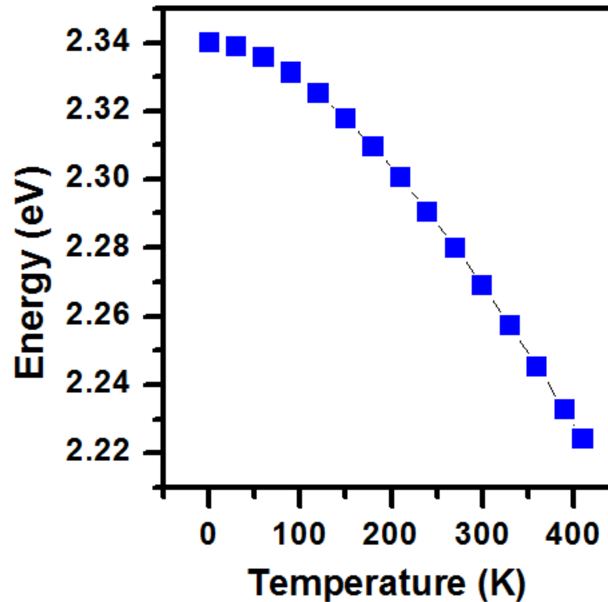

Figure 4.4: Temperature dependence of bandgap energy of GaP. The energy gap shifts toward lower energy with increasing the temperature.

4.3 Heterostructures band alignment

When two dissimilar crystalline semiconductors are brought in adjacent to each other, the interface between them is called a heterojunction. A heterostructure is defined as one or more heterojunctions. The most fundamental feature of a heterojunction is the different bandgap energies of the participating semiconductors. The different bandgap energies cause discontinuities in both valence band and the conduction band. These discontinuities are the origin of many interesting and useful properties of heterojunctions. The recent advanced epitaxial growth methods help to achieve the high–quality heterostructures which are useful for designing the new devices based on the heterostructures [69, 70].

Since the charge carriers occupy the band state with lower energy, the properties of the heterojunction depend critically on the band alignment at the interface.

The band alignment is defined as the relative position of band edges at the interface of a heterojunction. The heterojunctions, therefore, may be classified in two fundamental systems based on their band alignment, (1) Type–I, (2) Type–II [2, 70]. Fig. 4.5 shows the two basic types of the heterojunctions. In a type–I heterojunction, both electrons and holes are localized in semiconductor B. It means that the bandgap of semiconductors A and B are aligned such that both conduction band or electrons barrier and, valence band or holes barrier are of the same material. In a type–II heterojunction, on the other hand, the electrons barrier (conduction band) and the holes barrier (valence band) are in different semiconductors. This leads to spatial separation of electrons and holes. Localization of electrons and holes in two different materials causes the reduction of the overlap between electron–hole wavefunctions. This reduction is followed by longer recombination time compared to the type–I system [71]. To calculate the band alignment of a heterojunction,

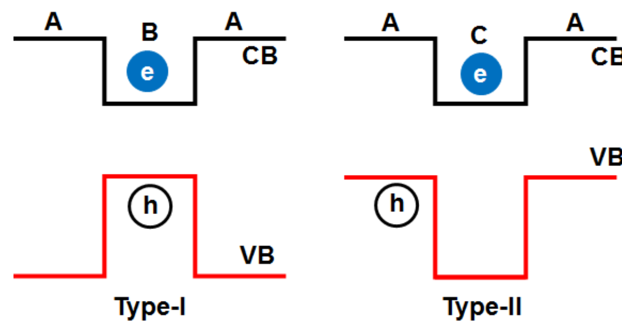

Figure 4.5: Type–I heterojunction with localized electron (e) and hole (h) in material B, and Type–II heterojunction with localized electron in material C and hole in material A [2]. The black circles represent e and the empty circles denote h.

various model theories have been developed. The electron affinity rule calculates the conduction band offset by considering that the difference between conduction and valence band at the surface is fixed. Anderson presented a simple model to explain the Ge–GaAs heterojunction band alignment. In his model, the band profile is determined with the Fermi level and the electron affinity in both semiconductor [73, 74]. Tersoff proposed the formation of a neutrality level in each participating semiconductors at the interface [75]. All these models are based on the bulk properties and the electron distribution at the interface is not taken into account. A better

picture about the band alignment at the interface is given by the self–consistent calculation based on the density functional theory (DFT) [76]. These calculations are, however, time–consuming and complicated. The model–solid theory or the Van de Walle model is a simple model theory, which can predict the band alignment at the interface without requiring very complicated calculation. Although, this model for simplification uses some approximation, but the calculations are reliable [77, 78].

In this thesis, the model–solid theory is used to calculate the band alignment of the desired heterojunctions. The more discussion about the Van de Walle model will be done in the next section.

4.4 Strain and model–solid theory

Strain is referred as the alteration of the relative position of the atoms in crystal sites due to an external mechanical force. At the interface of a heterojunction, the different lattice constants of adjoining semiconductors can act as the origin of this external force. This mechanical force changes the relative positions of atoms in the crystal structure and the displacement of the atoms compared to their initial positions can be defined using a vector, $\overrightarrow{u}$. Since different atoms may have different displacement, therefore, the displacement vector is a coordinate–dependent ($\overrightarrow{u}$ = u($\overrightarrow{r}$)). Knowing the relative displacement of each atom, the crystal deformation can be described by the symmetrical tensor of strain as [71, 72]:

$$\varepsilon = \begin{pmatrix} \varepsilon_{xx} & \varepsilon_{xy} & \varepsilon_{xz} \\ \varepsilon_{yx} & \varepsilon_{yy} & \varepsilon_{yz} \\ \varepsilon_{zx} & \varepsilon_{zy} & \varepsilon_{zz} \end{pmatrix} \quad (4.8)$$

where ε_{ij} is defined as the relative displacement of atoms in crystal:

$$\varepsilon_{ij} = \frac{1}{2}(\frac{\partial u_i}{\partial x_j} + \frac{\partial u_j}{\partial x_i}), i, j = x, y, z \quad (4.9)$$

If an external force is applied on a crystal or one part of crystal applies force on the neighbor part, then, the crystal is under the "stress". The stress is defined as [71]:

$$\sigma_i = \sum_{k=1}^{6} C_{ik}\varepsilon_k \quad (4.10)$$

where C_{ijkl} are the "elastic stiffness matrix". In the case of a cubic crystal, symmetry reduces the matrix elements to only three independent matrix elements. Consequently, elastic stiffness matrix is reduced to:

$$C_{ik} = \begin{bmatrix} C_{11} & C_{12} & C_{13} & 0 & 0 & 0 \\ C_{12} & C_{11} & C_{13} & 0 & 0 & 0 \\ C_{13} & C_{13} & C_{11} & 0 & 0 & 0 \\ 0 & 0 & 0 & C_{44} & 0 & 0 \\ 0 & 0 & 0 & 0 & C_{44} & 0 \\ 0 & 0 & 0 & 0 & 0 & C_{44} \end{bmatrix} \tag{4.11}$$

The stress state can be organized into two states [71]:

- Uniaxial stress, in this state, σ_{xx} is the only non–zero element of stress matrix
- Biaxial stress, in which both σ_{xx} and σ_{yy} are not equal to zero.

The biaxial stress is the common stress state in the quantum well heterojunctions. It occurs when a thin layer of material B with the lattice constant of a_B is deposited on a thick substrate with the lattice constant of a_A. Accordingly, a_B is forced to change and an in–plane strain is created. In a pseudomorphic growth, the lattice constant of grown material(B) becomes fully equal to the lattice constant of substrate, perpendicular to the growth direction. The in–plane strain in the pseudomorphic growth can be calculated as [71]:

$$\varepsilon_{\parallel} = \frac{(a_B - a_A)}{a_A} \tag{4.12}$$

where a_A and a_B are the lattice constant of the substrate and grown material, respectively.

The lattice constant of the epitaxial layer can be either larger or smaller than the lattice constant of the substrate. In the case of $a_A < a_B$, the strain is compressive and consequently the lattice constant of the epitaxial layer in growth direction will be larger than the original lattice constant of material B (Fig. 4.6(a)). While, when $a_A > a_B$ the in–plane strain is tensile and, therefore, the epitaxial lattice constant in the growth direction shrinks to a smaller value than the original lattice constant [71]. However, if the thickness of the epitaxial layer is larger than a specific thickness, the

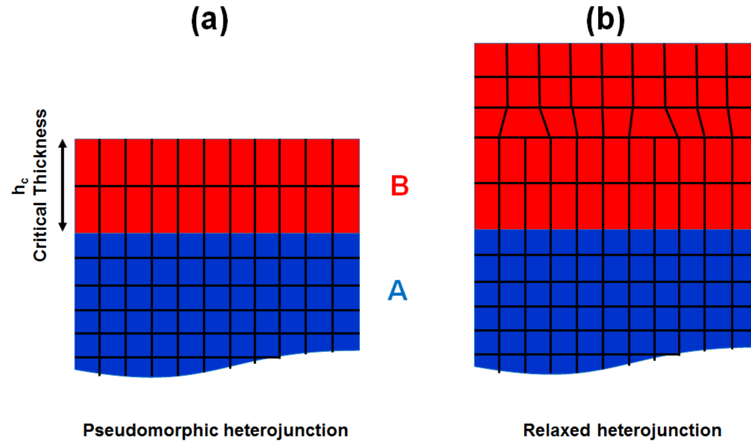

Figure 4.6: Scheme of a lattice mismatched growth, (a) pseudomorphic, (b) relaxed.

layer relaxes in–plane and achieves its original lattice constant. This process leads to the formation of defects and imperfections within the grown layer (Fig.4.6b). This specific thickness, in which the strain energy is higher than the defect formation energy, is called "critical thickness".

The relation between the stress and strain for the cubic semiconductors is given by Hooke's law that for biaxial stress is written as [71]:

$$\begin{bmatrix} \sigma_1 \\ \sigma_2 \\ \sigma_3 \\ 0 \\ 0 \\ 0 \end{bmatrix} = \begin{bmatrix} C_{11} & C_{12} & C_{13} & 0 & 0 & 0 \\ C_{12} & C_{11} & C_{13} & 0 & 0 & 0 \\ C_{13} & C_{13} & C_{11} & 0 & 0 & 0 \\ 0 & 0 & 0 & C_{44} & 0 & 0 \\ 0 & 0 & 0 & 0 & C_{44} & 0 \\ 0 & 0 & 0 & 0 & 0 & C_{44} \end{bmatrix} \begin{bmatrix} \varepsilon_1 \\ \varepsilon_2 \\ \varepsilon_3 \\ \varepsilon_4 \\ \varepsilon_5 \\ \varepsilon_6 \end{bmatrix} \tag{4.13}$$

Therefore, strain in the epitaxial layer grown in (001) crystal direction is given as:

$$\varepsilon_1 = \varepsilon_2 = \varepsilon_{\parallel} \tag{4.14}$$

$$\varepsilon_{\perp} = \varepsilon_3 = -2\frac{C_{12}}{C_{11}}\varepsilon_1 \tag{4.15}$$

where $\nu = -2\frac{C_{12}}{C_{11}}$ is known as the "Poisson's ratio". The lattice– and elastic–constants of the III–V semiconductors that were used in this work can be found in Appendix.II [78]. Using equations (4.12) and (4.15), it is possible to calculate the strain, perpendicular and parallel to the growth direction. Fig.4.7 presents the strain profile of a

thin GaAs layer with thickness of 3 nm on GaP substrate along the crystal direction of (001) [79].

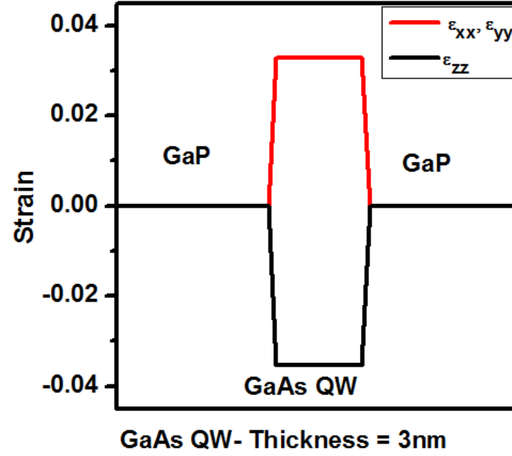

Figure 4.7: Strain profile for a GaAs QW with the thickness of 3 nm grown on GaP (001) substrate. Pink line indicates the strain perpendicular to the growth direction. Blue line is related to the strain parallel to the growth direction.

4.4.1 Strain induced energy shift

Strain perturbs the size and symmetry of the epitaxial layer and, therefore, changes its geometry. This, in turn, leads to the changes in the electronic structure of the epitaxial layer and particularly, it modifies the conduction band and valence band edges. To analysis the optoelectronic properties of any heterojunction, it is necessary to understand the discontinuity of conduction and valence band at the interface and effects of the strain on the band alignment. The shift of the conduction and valence band because of strain is determined using the deformation potential. This potential is defined as the changes in the relative energy of the electronic states.

To calculate the band lineup based on solid model theory, $E_{v,av}$ is defined as the average of three uppermost valence band energies at Γ. Therefore, it is possible to express any splitting of valence band due to shear strains or spin–orbit with referring each individual bands to the average. The spin–orbit splitting(Δ_0), bandgap energy (E_g), and average of valence band energy ($E_{a,v}$) for different III–V semiconductors can be found in Appendix.III [78]. The shift of $E_{v,av}$ of epitaxial layer due to the

strain is given by [78]:

$$\Delta E_{v,av} = a_v \frac{\Delta\Omega}{\Omega} \tag{4.16}$$

In the last equation, $\frac{\Delta\Omega}{\Omega} = Tr(\overrightarrow{\varepsilon}) = \varepsilon_{11} + \varepsilon_{22} + \varepsilon_{33}$ is the fractional volume change and a_v is the hydrostatic deformation potential of valence band that is defined as [78]:

$$a_v = \frac{dE_{v,av}}{dln\Omega} \tag{4.17}$$

and a_v indicates the shift of $E_{v,av}$ per unit fractional volume change. Similarly, the shift of CB edge is given by [78]:

$$\Delta E_c = a_c \frac{\Delta\Omega}{\Omega} \tag{4.18}$$

Therefore, minimum of conduction band and maximum of valence band of a strained epitaxial layer is given by [78]:

$$E_v = E^0_{v,av} + \Delta E_{v,av} + \frac{\Delta_0}{3} \tag{4.19}$$

$$E_c = E^0_c + \Delta E_c \tag{4.20}$$

The last term in equation (4.18) is related to the splitting of valence band due to the spin–orbit effects.

4.4.2 Valence band splitting due to strain

As it has been discussed in section 4.1, all the semiconductors, which are used in this work have a zinc blende crystal structure. Therefore, they have a band structure with three degenerated valence bands at Γ. These bands, which are labeled by E_{hh} for heavy holes, E_{lh} for light holes, and E_{so} for spin–off band, are strictly degenerated in the absence of strain and spin–orbit splitting effects. The average of these three bands is called $E_{v,av}$ (as it has been mentioned in the last section). Due to the spin–orbit splitting effect, E_{hh} and E_{lh} are shifted to the higher energy level compared to E_{so}. Strain, on the other hand, splits the heavy hole and light hole bands and determines the uppermost position of valence band. For strain along (001) crystal direction, the splitting of these three bands is calculated as [78]:

$$\Delta E_{hh} = -\frac{1}{6}\Delta_0 + \frac{1}{4}\delta E_{001} + \frac{1}{2}[\Delta_0^2 + \Delta_0 \delta E_{001} + \frac{9}{4}(\delta E_{001})^2]^{\frac{1}{2}} \tag{4.21}$$

$$\Delta E_{lh} = \frac{1}{3}\Delta_0 - \frac{1}{2}\delta E_{001} \quad (4.22)$$

$$\Delta E_{so} = -\frac{1}{6}\Delta_0 + \frac{1}{4}\delta E_{001} - \frac{1}{2}[\Delta_0^2 + \Delta_0\delta E_{001} + \frac{9}{4}(\delta E_{001})^2]^{\frac{1}{2}} \quad (4.23)$$

In the last three equations Δ_0 is the spin–orbit splitting, and δE_{001} is defined as [78]:

$$\delta E_{001} = 2b(\varepsilon_{zz} - \varepsilon_{xx}) \quad (4.24)$$

where b is a negative value of the shear deformation potential for a strain of a tetragonal symmetry. b has been measured for some of the semiconductors (not all) and it can be also calculated theoretically by analyzing the changes of the band structure due to the strain [78].

4.4.3 Conduction band splitting due to strain

The conduction band of growing material at X valley is also subjected by the biaxial strain, and it appears as the splitting. The value of splitting, of course, depends on the growth direction. In (100) growth direction, the conduction band splitting is calculated as [78]:

$$E_c^z = \frac{2}{3}X_i(X)(\varepsilon_{zz} - \varepsilon_{xx}) \quad (4.25)$$

$$E_c^x = E_c^y = -\frac{1}{3}X_i(X)(\varepsilon_{zz} - \varepsilon_{xx}) \quad (4.26)$$

In the last two equations $X_i(X)$ is the deformation potential of conduction band at X valley and ε_{zz} and ε_{xx} are the strain components parallel and perpendicular to the growth direction, respectively [79, 78].

4.5 Quantum confinement effect in quantum structures

Advances in microfabrication methods and techniques allow the creation of unique quantum confinement systems. These systems are called nanostructures that are in the length range of 10–1000 Å. Consequently, a wide field has been opened for investigation of fundamental physics of nanostructures and also the fabrication of new devices based on the nanostructures and their interesting properties [69, 71, 80, 81, 83].

The quantization effects in a semiconductor, however, occurs when the motion of charge carriers is confined in a small space with the size of the order of de Broglie wavelength. The de Broglie wavelength, in turn, is a function of, m^*, the effective mass of charge carriers (electron or hole), and k_BT. It is given as [69, 71, 80]:

$$\lambda_{de-Broglie} = \frac{h}{3m^* k_B T} \tag{4.27}$$

Since m^* is usually smaller than the free electron mass, consequently the quantization effect can be observed for the sizes in order of several tens of the lattice constant of the semiconductors. Fig. 4.8 indicates the gradual evaluation of a system from a three–dimension (bulk) to zero–dimension (quantum dot), and the density of electronic states of different system with respect to the energy [69]. In the case of a

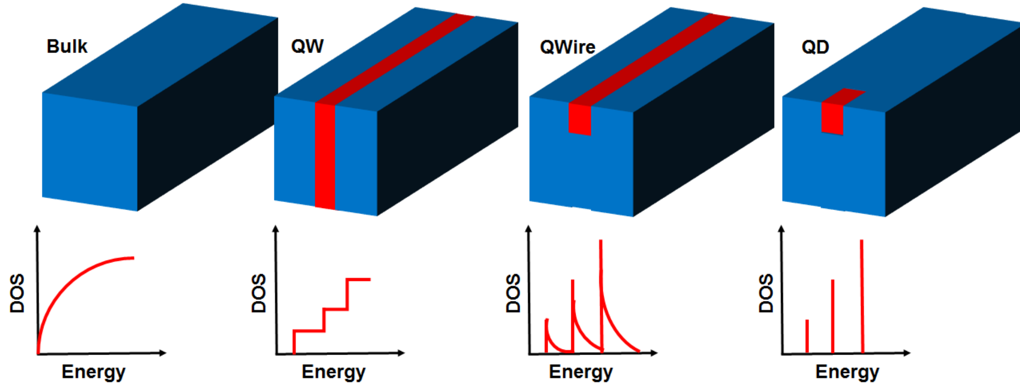

Figure 4.8: Scheme of evaluation from three–dimension bulk to zero–dimension QD. Second row presents the density of electronic states with respect to the energy and its evaluation with decreasing the dimension [69].

three–dimensional gas, electrons move freely in all three directions with the energy of [69, 71, 80]:

$$E = \frac{\hbar^2}{2m^*}(k_x^2 + k_y^2 + k_z^2) \tag{4.28}$$

here $k_{x,y,z}$ are the wavevectors and m^* is the effective mass of electrons in the bulk. Consequently, the energy spectrum of a bulk semiconductor is continuous.

The electron motion in a two–dimensional QW is quantized into two district sub–band in the z–direction (along the well thickness), but it is free in the x and y directions. The energy of a QW can be given as [69, 71, 80]:

$$E = \frac{\hbar^2}{2m^*}(k_x^2 + k_y^2 + E_z^i) \tag{4.29}$$

where i = 1, 2, 3,... and E_z^i is the ith energy state in the z–direction.

In a quantum wire (Q–Weir), which is a one–dimensional structure, electron motion is quantized in two directions and the energy can be written as [69, 71, 80]:

$$E = \frac{\hbar^2}{2m^*}k_x^2 + E_y^i + E_z^j \tag{4.30}$$

Again, i and j = 1, 2, 3,... give the energy states in y and z directions, respectively (Fig. 4.9(Q–Weir)).

Quantum dot (QD) is a zero–dimensional system with energy quantization in all three directions. This means that the electron motion is confined in x, y, and z–directions and, therefore, the energy is discrete and given by [69, 71, 80]:

$$E = E_x^i + E_y^j + E_z^k \tag{4.31}$$

4.5.1 Density of electronic states

According to Bloch's theory, in a bulk semiconductor the eigenstates must display the periodicity of the crystal. Therefore, the eigenstate of $\psi = \frac{1}{\Omega}exp(ik.r)$ in a cubic crystal with the length of L must behave as [71, 80]:

$$\psi(x,y,z) = \frac{1}{\Omega}exp(ik_x(x+L) + ik_y(y+L) + ik_z(z+L)) \tag{4.32}$$

and therefore:

$$k_i = \frac{2\pi}{L}n_i \tag{4.33}$$

where i = x, y, z and n_i is an integer. Hence, the occupied volume by one state in k–space is $(\frac{2\pi}{L})^3$. The density of states in k–space is defined as the number of states per energy per unit volume of real–space:

$$\rho(E) = \frac{dN}{dE} \tag{4.34}$$

The total number of states in k–space, N, is given by the volume of a sphere with radius of $\overrightarrow{k}$ divided by the volume of one occupied state, again divided by the volume of real–space. Consequently, we can write it as:

$$N = 2(\frac{4\pi k^3}{3(2\pi)^3}) \tag{4.35}$$

where, factor 2 shows the double possible occupancy of each state by carriers with different spins. Therefore, $\rho(E)$ in a bulk semiconductor can be written as:

$$\rho(E) = \frac{1}{2\pi}(\frac{2m^*}{\hbar^2})^{\frac{2}{3}} E^{\frac{1}{2}} \tag{4.36}$$

Accordingly, the density of state of a bulk semiconductor is continues and proportional to $E^{\frac{1}{2}}$. In a QW, however, the energy is continuous in two directions (only two freedom degrees). The density of state, in this case, is known as a two–dimensional electron (or hole) gas. The density of states of a single sub–band in a QW, therefore, is given by [69, 71, 80]:

$$\rho^{2D}(E) = \frac{m^*}{\pi\hbar^2} \tag{4.37}$$

For a QW system with many confined states, the density of states at any particular energy is equal to the sum over all the sub–bands below that point:

$$\rho^{2D}(E) = \sum_{i=1}^{n} \frac{m^*}{\pi\hbar^2} \Theta(E - E_i) \tag{4.38}$$

In (4.38), n denotes the number of confined states in the QW and Θ is the unit step function [71, 80]. In a QD system, the density of states behaves as a δ–function because the carriers motions are confined in all three directions.

4.6 Optical properties

This work is mostly concentrated on the optical properties of the quantum heterostructures. Therefore, to understand and interpret the obtained results from different optical measurements such as CL and PL, it is useful to have a brief introduction about the optical properties.

When photons with higher energy than the bandgap energy incident a semiconductor, electrons can be excited from the valence band across the bandgap into the conduction band. This process is called the excitation in which a free electron is created in the conduction band and an empty state is left in the valence band. This empty state that behaves as a bubble in a liquid is called "hole", which has generally larger mass than the electron. Holes are positively charged and they rise to

the uppermost states in the valence band [71, 80]. The transition between the electron and hole can occur only when the energy and momentum are conserved [53]. Fig.4.9 shows some of the radiative and non–radiative recombination processes. The excited electron may relax via the radiative or non–radiative recombination. In

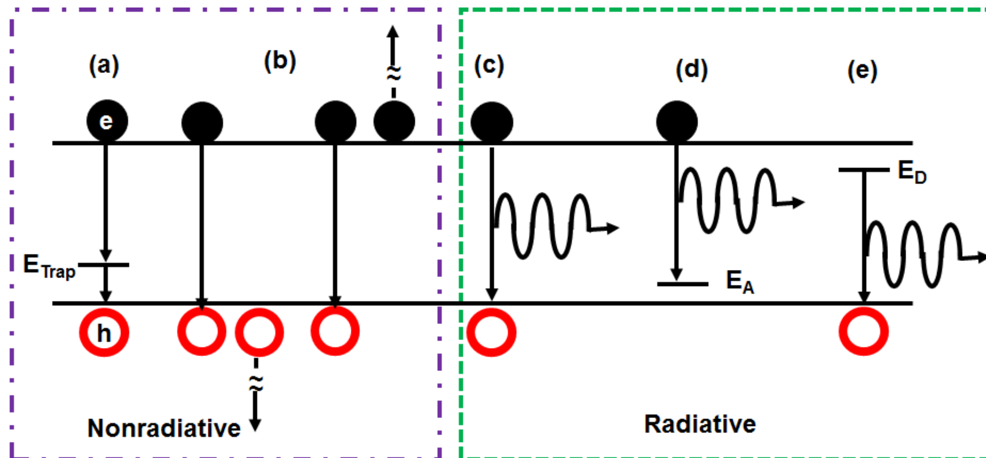

Figure 4.9: Different radiative and non–radiative recombination [53]. (a) Non–radiative with trap states, (b) Auger non–radiative recombination, (c) band to band radiative, (d) electron–acceptor radiative, (e) donor–hole radiative.

a radiative recombination or transition event, a photon is emitted due to the recombination of electron and hole. An interband transition is an intrinsic transition referred to the recombination of the electron in the conduction band and hole in the valence band and emission of a photon with the energy of $h\nu = E_g$. In a semiconductor with impurities, transitions that start or finish to the localized states (donors or acceptors) in the gap produce extrinsic luminescence [53]. In a non–radiative recombination, on the other hand, the electron energy is converted to the heat (phonon). Non–radiative recombination events are caused by defects in the crystal structure. Defects such as unwanted foreign atoms, native defects, dislocations, and any complexes of defects construct one or several energy levels within the forbidden gap of the semiconductor. Energy levels within the gap of the semiconductor are efficient recombination centers; in particular, if the energy level is close to the middle of the gap. The non–radiative recombination centers are luminescence killers that reduce the output efficiency of the light emitters [82].

Chapter 5

AlGaP/GaP heterostructure

In 1965, the co–founder of Intel G. Moore predicted that the number of transistors that can be fitted in one integrated circuit is doubled every two years [84]. However, parameters such as atomic-scale miniaturization, production facilities, the existence of many wires close to each other, and heat build–up in one tiny chip can be the limitations of Moore′s law. In the last decade, the photonic devices were introduced as the interesting candidates to substitute the electronic transistors. These devices, which can be fabricated with the existing facilities, get the electronic signals and then convert and transmit them as the photonic waves. Basically, the electrical wires are replaced by the photonic waves and hence, the limiting factors to design the processors are eliminated. Consequently, Moore′s law can be valid through these photonic devices. Photonic crystal cavity is one of these devices that got lots of attention. The performance of the photonic crystal cavities, in turn, depends on the losses, which determine their quality factor.

In this chapter, I will discuss the results of the investigations on the influence of the growth conditions on the AlGaP/GaP heterostructures which can be applied to fabricate a two–dimensional photonic crystal slab (or cavity). In the next section, 5.1, the photonic crystals will be introduced and the different types of defects and their effects on the losses of the photonic crystals will be discussed. Section 5.2 is focused on the different materials for the photonic crystal cavities fabrication in the visible range of wavelength. The influence of the growth temperature and PH_3 flux on the homoepitaxial growth of GaP will be discussed in section 5.3. The growth of AlGaP/GaP heterostructures will be described and the characterizations and results will be discussed in section 5.4. Finally, section 5.5 includes the summary.

5.1 Photonic crystals

The advantages of photonic devices for the information processing in the optical domain make them an interesting candidate as the replacement of the electronic devices. The optical equivalent of a lattice is called a "photonic crystal". In a photonic crystal, atoms or molecules are replaced with the macroscopic media and the periodic potential is replaced by the periodic dielectric constants (or refractive indexes) [11, 12, 13, 15, 16, 17]. The phenomena that are produced by the lattice

for the electrons, can be reproduced by the photonic crystal for the photons if the dielectric constants of the constituent materials are greatly different and the light absorption by the materials is little. Therefore, the refraction and reflection of the light from different interfaces determine the "photonic bandgap" of the photonic crystal. Thus, a photonic crystal can be designed and constructed with a particular photonic bandgap that specifies a certain direction with a given wavelength for the light propagation [11, 12, 13, 15, 16, 17]. Photonic crystals are classified based on their dimensional [12]. The distributed Bragg reflectors (DBR) are the one–dimension [85, 86, 87, 88], cavities or slabs are the two–dimension photonic crystals [89] and, third class is for 3D–photonic crystals [90, 91, 92, 93, 94, 95].

The performance of the photonic crystal cavities is defined by the high–quality factor (Q–factor). The Q–factor is a dimensionless parameter that depends on the energy loss mechanisms. The experimentally obtained Q–factor for a fabricated cavity, Q_{exp}, is usually less than the theoretically determined Q–factor by the designed cavity, Q_{design}. This difference is explained using the Q–factor of the imperfections of the fabricated cavity, $Q_{imperfect}$ [96]:

$$\frac{1}{Q_{exp}} = \frac{1}{Q_{design}} + \frac{1}{Q_{imperfect}} \tag{5.1}$$

The crystal imperfections such as dislocation defects and surface roughness are likely the mechanisms that contribute in the $Q_{imperfect}$ and reduce the total Q_{exp}. In fact, the real materials are not perfect crystal and, consequently, their properties are not determined only by their composition or crystal structure. The crystal imperfections, or so–called crystalline defects, contribute effectively in the property determinations of the materials [97]. Dislocation defects, for instance, are the 1–dimensional type of the crystalline defects. This type of defects is defined as line defects along which the crystal symmetry is lost. They are formed during the growth of the crystals and particularly at the interface of the heterostructures. They behave as the traps for charge carriers in the optoelectronic materials and semiconductors, which is an undesired parameter against the electrical conductivity [97, 98, 99, 100]. Dislocations are usually categorized into two fundamental types of (i) the edge dislocations and (ii) the screw dislocations. The other types of dislocations, such as

compound or ring–dislocations, might be constructed from the combination of the edge– and screw dislocations. Fig. 5.1 shows the scheme of (a) an edge–dislocation , and (b) a screw–dislocation. The density of dislocations in a grown structure can be determined using Hirsch's model [50]. It has been already shown in chapter 3 that the density of dislocation of a grown layer can be determine using the X–ray diffraction pattern and it is proportional to the FWHM of its associated peak (equation 3.8) [101].

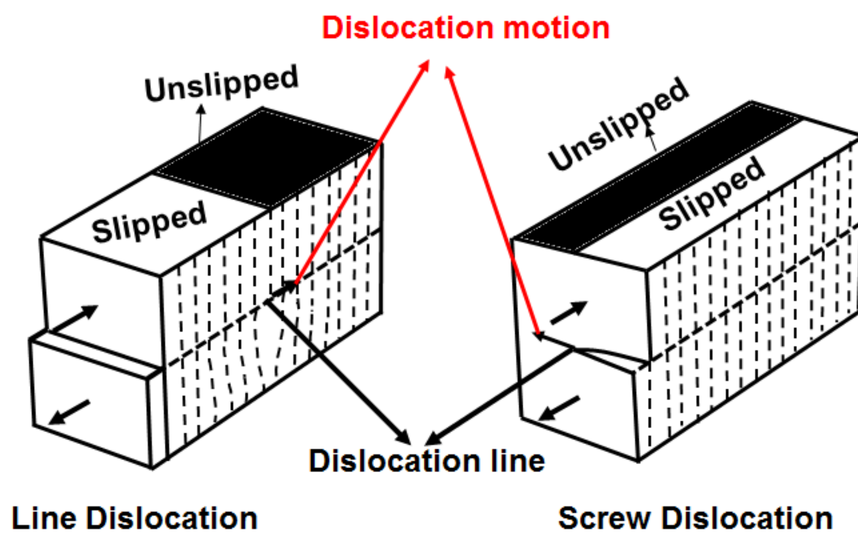

Figure 5.1: Scheme of the dislocation defects, (a) line dislocation, (b) screw dislocation [99].

The surface roughness (or roughness) is the other type of crystal imperfection that might contribute to the losses of the photonic crystal cavities (or slabs). The roughness is defined as the deviation in the direction of the normal vector to the ideal surface and the average surface roughness is determined according to the deviation amplitude. Therefore, a rough surface is associated with a large amplitude of the deviation [102]. The surface roughness is particularly important for the light scattering in the short wavelengths region. Consequently, for the photonic crystal cavities, which are designed for visible and short wavelengths range, the surface roughness is an undesired parameter that can increase the losses and reduces the Q–factor.

5.2 Photonic crystal cavity in the visible range of wavelength

For the applications in the range of visible wavelengths, photonic crystal cavities based on GaAs and Si cannot be applied because of their small bandgaps and, consequently, high absorption. Photonic crystal cavities with shorter wavelengths transparency are usually fabricated based on the GaN, SiN, and GaP systems. Difficult fabrication processes and the low refractive index are the problems of GaN systems [103, 104]. The low refractive index is also a disadvantage of SiN which limits the Q–factor of the device [105]. GaP, on the other hand, is a good candidate for short wavelengths photonic crystals due to its large indirect bandgap energy of 2.24 eV and high refractive index in the range of 3.44 to 3.25 for the wavelengths between 555 to 700 nm [106]. Moreover, the fabrication of the GaP photonic crystal in coupling with InP, InGaAs, and GaAs quantum dots can raise the quantum efficiency of the light emitters in visible wavelengths region [107]. Rivoire et al. investigated the fabrication of high–quality photonic crystal cavities based on GaP using a sacrificial layer of AlGaP [14, 108, 109].

The Q–factor of a photonic crystal based on GaP, as it has been already mentioned, is limited by the crystal quality of the membrane that is, in turn, dependent on the AlGaP sacrificial layer crystal quality. AlGaP, however, is a reactive material which can be easily oxidized, therefore, to prevent the oxidation a thin GaP layer is needed to grow on the AlGaP layer. Since the growth of the AlGaP layer with the minimum density of dislocations and oval–defects and minimum surface roughness is a difficult challenge, it is limiting the quality of the GaP top layer that should be fabricated into a membrane.

5.3 Homoepitaxial growth of GaP: influences of growth temperature and PH_3 flux

The growth of a high–quality AlGaP layer is required to achieve a high–quality GaP cap layer (membrane). The growth of an AlGaP layer with high–quality, in turn, depends on the quality of the homoepitaxial growth of GaP buffer layer on

the GaP substrate. The influence of the III/V ratio and growth temperature on the surface structure of GaP grown by MBE have been investigated [110, 111]. The optimized conditions to carry out a high–quality homoepitaxy growth of GaP, however, may change depending on the MBE system. Accordingly, I have investigated the influence of growth temperature and PH_3 flux to optimize the quality of the grown GaP buffer layer in our Riber–32P GSMBE system. The growth of GaP layer was done using PH_3 as the phosphorus source and solid Ga source. The growth temperature was measured by a thermocouple located directly behind the GaP substrate held by its rim and the PH_3 flux was controlled using a flux meter with the unit of the standard cubic centimeter (sccm).

Several GaP buffer layer were grown with identical thicknesses of 0.2 μm under two different PH_3 fluxes and at the different growth temperatures with an identical growth rate of 1.1 μm/h. Tab. 5.1 presents the different growth conditions. All the samples were grown on the S–doped GaP (001) substrates with a thickness of 300 μm.

Table 5.1: Growth conditions and AFM characteristics of GaP layer grown on GaP (100) substrate

sample	**Growth T (^{o}C)**	**PH_3 (sccm)**	**Roughness (nm)**
B1	520	2.7	15.1
B2	510	2.7	15.3
B3	490	2.7	12.7
B4	540	1.9	16.7
B5	510	1.9	0.5
B6	490	1.9	0.5
B7	480	1.9	0.4

The native oxide of the GaP substrates was removed by heating the substrate to 580°C under a PH_3 over pressure and the RHEED pattern of GaP substrate showed a streaky reconstruction after oxide desorption (Fig. 5.2(a)). RHEED reconstruction patterns indicate that independent of the growth temperature the higher PH_3 flux

of 2.7 sccm leads to a spotty pattern for the grown GaP layer (Fig. 5.2(c)), while growth of GaP layer under 1.9 sccm PH_3 flux and at growth temperatures in the range of 480–510 ^oC leads to the streaky pattern of RHEED reconstruction.

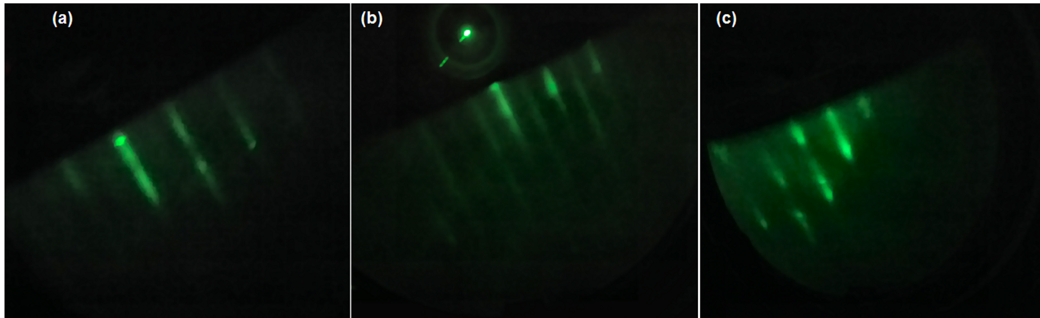

Figure 5.2: RHEED pattern of the surface reconstructions, (a) after desorption at 580°C, (b) GaP Buffer layer grown at 490°C and under PH_3 flux of 1.9 sccm, and (c) GaP Buffer layer grown at 490°C and under PH_3 flux of 2.7 sccm.

The surface quality of the grown samples was characterized using a force–mode Burker AFM system. The measurements were done in Leibniz–Institut f*ü*r Kristallz*ü*chtung (IKZ) with the assistance of Dr. J. Schmitdbauer. The results were analyzed using the WSxM v5.0 [112]. Fig. 5.3 illustrates the results of AFM measurements of different grown samples. The bright and almost round shape particles on the surface of samples B5 and B6 are related to the grown InGaAs QDs.

The AFM results indicate that for identical growth temperatures of 490 and 510 ^oC the surface roughness decreases when the PH_3 flux is reduced about 40% from 2.7 sccm to 1.9 sccm. According to the RHEED pattern and AFM results, GaP buffer layer, grown under 1.9 sccm PH_3 flux and at the growth temperature range of 480–510 ^oC, indicates the optimum quality with the minimum surface roughness of 0.4$\pm$0.1 nm.

It can be suggested that the higher PH_3 leads to lower mobility of group III ad–atoms that can increase the probability of the agglomeration and ,consequently, the formation of 3D–islands instead of a 2D layer by layer homoepitaxy of GaP. The rise of growth temperature up to 540 ^oC under lower PH_3 flux, however, may cause the insufficient P_2 flux due to the increase of the evaporation rate of the group V element. This, in turn, causes a Ga–rich growth which is followed by the formation

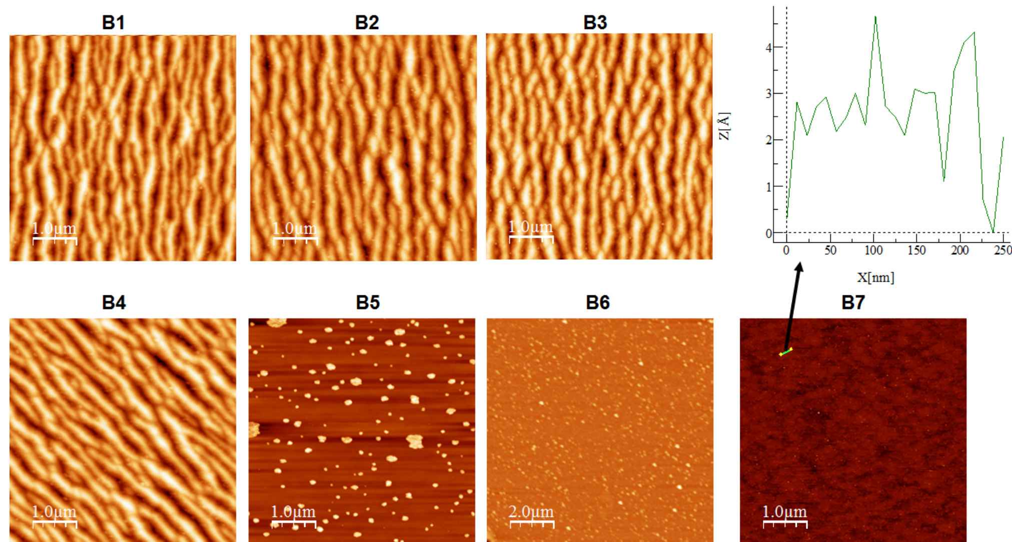

Figure 5.3: AFM images of grown GaP buffer layer. The bright particles on the surface of the B5, B6, and B7 are related to the grown InGaAs QDs on the GaP buffer layer. The scan line of B7 is also shown, the –axis shows the height profile in Åand the x–axis is related to the line scan size in nm.

of islands. To avoid the influence of the GaP buffer layer quality on the AlGaP layer the optimized growth conditions (P_2 flux = 1.9 sccm and growth temperature in the range of 490–500 ^oC) were applied to grow the GaP buffer layer.

5.4 AlGaP/GaP heterostructure:influences of growth temperature and PH_3 flux

After optimization of the growth conditions for the GaP buffer layer, the effects of the growth temperature and PH_3 flux on the crystal quality of AlGaP layer were studied and the influences of the quality of this layer on the final GaP cap layer that will be fabricated as the membrane for the photonic crystal cavities applications were investigated.

The X–ray diffraction technique has been utilized to study the crystal quality of the GaP/AlGaP heterostructures [113, 114]. The influences of the growth temperature and PH_3 flux, however, have not been studied on the crystal structure of AlGaP. Thus, the influences of the quality of AlGaP layer on the GaP cap layer has

not been investigated. I have grown several AlGaP/GaP heterostructures to study the influences of III/V ratio and also growth temperature on the crystal quality of AlGaP and to optimize the quality of GaP cap layer. Fig. 5.4 illustrates the grown structures. Each sample consists of a 0.2 μm GaP buffer, 1.0 μm $Al_{0.85}Ga_{0.15}P$, and the 80 nm GaP cap layer. The GaP layers were grown at 1.1 μm/h and the AlGaP at 1.6 μm/h. The growth of each GaP layer was carried out under the optimized growth conditions of the PH_3 flux equal to 1.9 sccm and the growth temperature in the range of 490$\pm$10 ^{o}C (section 5.3). Two different PH_3 flux of 2.3 or 2.7 sccm were applied to investigate the influence of the PH_3 flux on the AlGaP layer. A constant growth temperature of 480, 490, or 500°C was used for each sample. The applied growth conditions are summarized in Tab. 5.2.

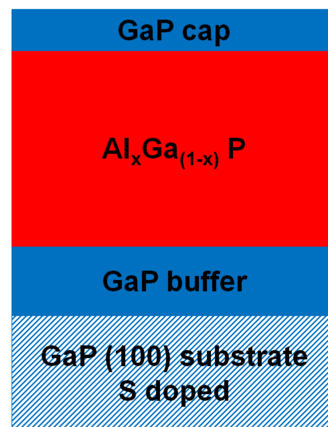

Figure 5.4: Scheme of structures. Al content for all samples was set to be 85%. GaP buffer and cap layer were grown under 1.9 sccm PH_3 while to grow AlGaP layer different fluxes of 2.3 and 2.7 were used. Same growth temperature was applied during growth of GaP and AlGaP.

In the last section, I have discussed the growth of high–quality GaP buffer layer. Accordingly, AlGaP layer was grown on the optimized GaP layer with the minimum surface roughness. Consequently, for all samples, the RHEED patterns of GaP buffer layers demonstrate a very sharp and streaky pattern (Fig. 5.2(b)). The samples grown using the lower PH_3 flux (2.3 sccm) show a spotty RHEED pattern for the first monolayers upon initiation of the AlGaP growth(Fig. 5.5(a)). The pattern, however, becomes better by the time the full 1.0 μm AlGaP layer is grown (Fig.5.5(b)) [115].

Table 5.2: Growth temperature and PH_3 flux of the AlGaP layer for different samples

sample	Growth T (^oC)	PH_3 (sccm)
S1	480	2.3
S2	480	2.7
S3	490	2.7
S4	500	2.7
S5	500	2.3

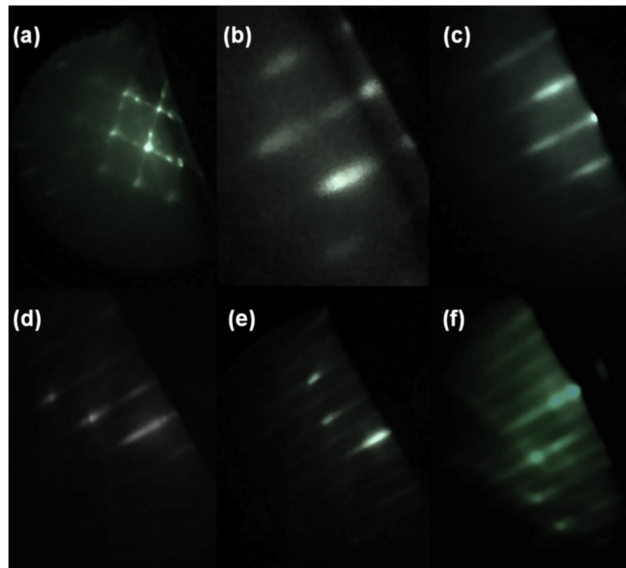

Figure 5.5: RHEED pattern images, (a) first ML growth of AlGaP under 2.3 sccm PH_3 flux indicated the spotty pattern, (b) this pattern improved by the time the 1.0 μm AlGaP layer was grown fully, (c) the pattern of GaP cap layer for S1, while S3 showed, (e) a streaky and sharp pattern from the beginning of the AlGaP layer, (f) after full growth of AlGaP layer, and (g) after the growth of GaP cap layer.

After overgrowth with the GaP cap layer, the RHEED is again sharp (Fig. 5.5(c)). The RHEED of the AlGaP grown under the higher PH_3 flux (2.7 sccm), however, indicate sharper and streakier patterns for both AlGaP and GaP cap layers (Fig. 5.5(d, e, and f)). The RHEED pattern is sharp from the initial grown monolayers of the AlGaP. This may be associated with the better crystal quality of AlGaP layer grown under higher PH_3 flux which can lead to the improvement of the crystal

quality of the GaP cap layer.

The crystal quality of grown AlGaP layer was measured using a Bede–QC1 diffractometer in our lab and the measured spectra are presented in Fig.5.6. The results indicate the strong reduction of full FWHM of AlGaP peak with 25% increase of the PH_3 flux from 2.3 sccm (S1 and S5) to 2.7 sccm (S2, S3 and, S4) and, consequently, this suggests that the density of defects is reduced. In the case of 2.3 sccm PH_3 flux, however, the increase of growth temperature from 480 ^oC (S1) to 500 ^oC (S5) leads to the narrowing of AlGaP peak while FWHM changes slightly with the growth temperature under the higher PH_3 flux (Tab. 5.3) [115]. The density of dislocation defects can be calculated based on the Hirsch model [50].

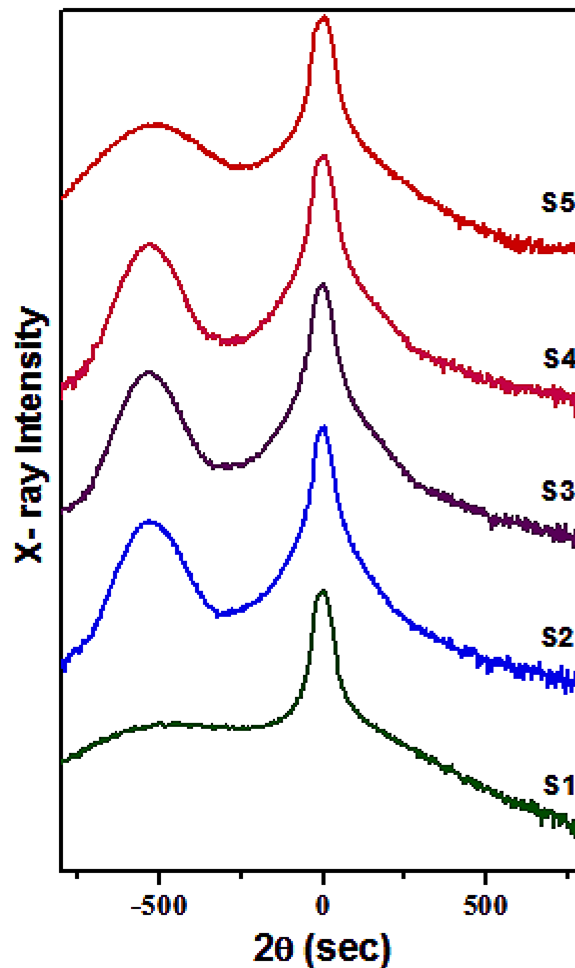

Figure 5.6: X–ray measurement results for samples grown at different temperature and under different PH_3 flux. The sharper peak belongs to the GaP and the other peak is related to $Al_{0.85}Ga_{0.15}P$ layer.

Calculated results show that for S1 and S2, N decreases from 7.4 $\times$ 10 ^{8} to 0.1 $\times$ 10^{8} cm^{-2}. These results may be associated with the sharper RHEED patterns of AlGaP layer grown under higher PH_3 flux.

Table 5.3: Extracted result from the X–ray measurements rocking curve

sample	**FWHM $\times 10^{-3}$ (rad)**	**N $\times$ 10^{8} (cm^{-2})**
S1	2.24	7.4
S2	0.38	0.1
S3	0.32	0.1
S4	0.34	0.1
S5	0.74	0.8

Since the equivalent optimized growth conditions were utilized to grown the GaP buffer layer and cap layer, the structural quality of the cap layer can be affected by the quality of AlGaP layer. Hence, AFM and SEM results of the surface can be related to the structural quality of AlGaP layer. Fig. 5.7 presents the AFM images of the different samples. Even though the growth of both GaP buffer and cap layers was carried out under the optimum conditions, the results are different. This can be associated with the quality of AlGaP layer for different samples. Using the AFM results, we can determine the optimum growth conditions for the AlGaP layer which lead to the minimum surface roughness and density of oval defects for the GaP cap layer. AFM results indicate that the surface roughness and density of oval defects of the grown GaP cap layer reduce strongly when the PH_3 flux for the AlGaP layer rises. Tab. 5.4 gives the results of AFM measurements for the surface roughness and density of oval defects of different samples [115].

Accordingly, samples S2 and S3 indicate lower surface roughness and density of oval defects compared to S5. This can be related to the narrowing of X–ray peak of AlGaP. In the case of the samples with AlGaP layer grown under higher PH_3 flux, however, AFM measurements indicate that 10 ^{o}C lower growth temperature than 490 ^{o}C leads to the formation of the oval defects.

These results indicate the formation of oval defects with the average size of

Table 5.4: Extracted result from AFM and SEM measurements of different samples. The PH_3 flux was 1.9 sccm for the cap layer of all samples, while it was 2.3 sccm for S1 and S5 and 2.7 sccm for S2, S3 and, S4 for the AlGaP layer. d_o represents the diameter of oval defects, while D_o denotes the density of oval defects

sample	**r_{ms} (nm)**	**AFM d_o (μm)**	**AFM $D_o \times 10^8$ (cm^{-2})**	**SEM d_o (μm)**	**SEM $D_o \times 10^8$ (cm^{-2})**
S1	14.8	0.287	12.8	0.33	7.6
S2	0.58	0.230	0.1	0.33	0.07
S3	0.48	No	No	No	No
S4	1.03	No	No	0.33	0.28
S5	3.78	0.285	2.0	0.33	4.0

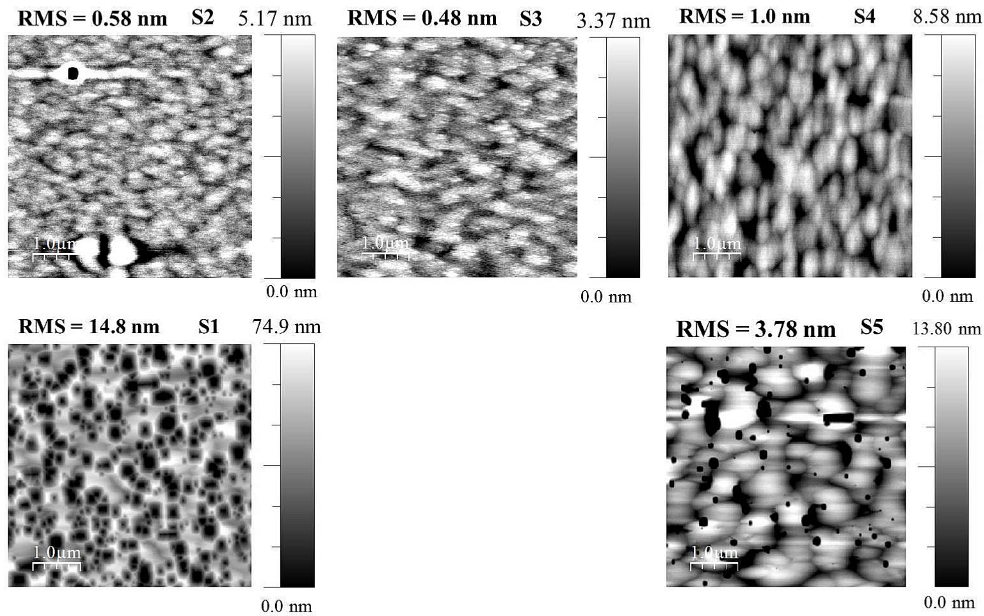

Figure 5.7: AFM images of the grown samples at different temperature. The PH_3 flux was 1.9 sccm for the cap layer of all samples, while it was 2.3 sccm for S1 and S5 and 2.7 sccm for S2, S3 and, S4 for the AlGaP layer. All the AFM measurements were done on the 5×5 μm scale.

0.23 ± 0.05 μm and density of 1.1×10^7 cm^{-2} for S2 and, consequently, the root mean square (r_{ms}) of surface roughness of S2 (0.58 nm) is slightly larger than S3

(0.48 nm). This result may be related to the slight broadening of the FWHM of AlGaP X–ray peak of S2 compared to S3 (Tab. 5.3).

SEM measurements corroborate the AFM results (Fig. 5.8). The results do not show any oval defects for S3 while the formation of the hole–shape oval defects is illustrated for all the other 4 samples. According to these measurements the average size of the oval defect is almost same for the different samples and it has been measured to be about 0.33±0.02 μm. The density of defects, however, strongly decreases with the increase of the PH_3 flux (Tab. 5.4).

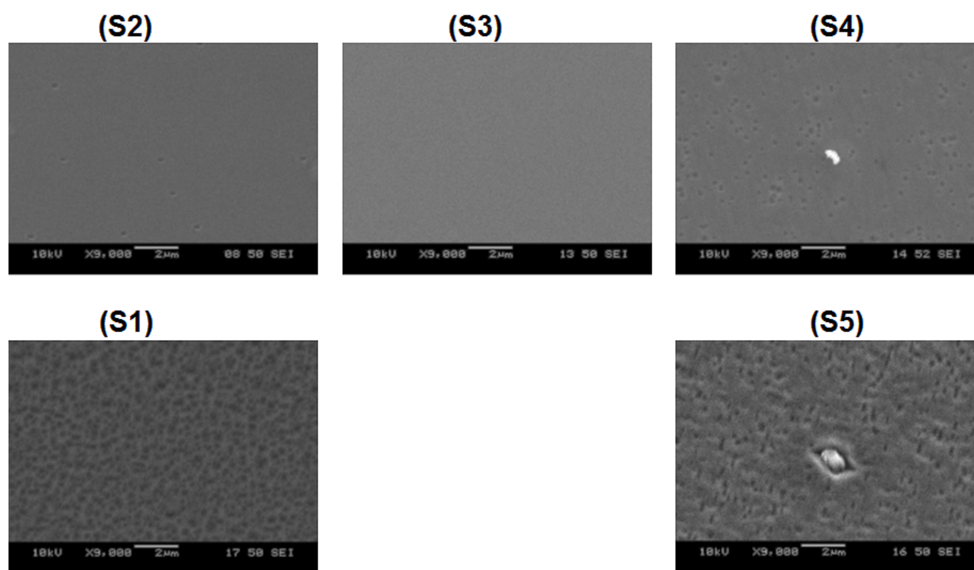

Figure 5.8: Top view SEM images of the different samples. For S3 no oval defect is observed while the density of the oval defect rises with the reduction of PH_3 flux for identical growth temperature. Images were carried out under 10 keV and identical scale of 2 μm.

It is possible that the 25% increase of the PH_3 flux improves the crystal quality by decreasing the surface mobility, resulting in smoother surfaces. Under these conditions, the probability of formation of the 3D islands or agglomeration of group–III ad–atoms reduces [110, 111, 116]. The insufficient availability of P_2 might be the reason of the wide FWHM of X–ray peak and, therefore, the high density of the dislocation defects of the AlGaP layers grown under lower PH_3 flux. The low crystal quality of AlGaP layer can affect the crystal quality of the GaP cap layer, and consequently, the high roughness and density of oval defects of S4 and S5 may be

associated with the high density of dislocation defects. The AFM and SEM results, however, indicate that S3 has the lowest surface roughness and density of oval defects. Accordingly, 490 ^{o}C is the optimum growth temperature under high PH_3 flux. This may be related to the better crystal quality of the AlGaP layer of S3 which is confirmed by its less FWHM compared to S2 and S4. The increase of growth temperature can lead to the less availability of P_2 and consequently the increase of the diffusivity of group–III ad–atoms. Thus, a higher probability for the agglomeration of group–III ad–atoms [110, 111, 116] can be predicted which results in the rise of the density of dislocation defects and wider FWHM for AlGaP layer. However, for the growth temperature lower than 490 ^{o}C, the insufficient surface energy may be the reason for the formation of dislocation defects [114]. The mobility reduction of group–III ad–atoms may be related to the increase of the FWHM of AlGaP which can cause the oval defects formation on the GaP cap layer for S2 [115].

5.5 Summary

According to the RHEED pattern and AFM, a smooth GaP buffer layer can be grown on the GaP (001) substrate utilizing the PH_3 flux of 1.9 sccm and temperatures in the range of 480–510 ^{o}C. The X–ray results of AlGaP layer imply that the grown sample at 490 ^{o}C under 2.7 sccm PH_3 flux (S3) has the minimum FWHM of AlGaP layer and AFM and SEM measurements also show that the GaP cap layer has the both minimum density of oval defects and surface roughness. Density of defects and surface roughness rise with PH_3 flux reduction which may be due to the insufficient availability of P_2 and it can be the origin of higher probability for formation of 3D islands of group–III ad–atoms. Under high PH_3 flux (2.7 sccm), both increase and decrease of the growth temperatures than 490 ^{o}C, show the rise of FWHM of AlGaP and roughness of cap layer. The growth temperatures below 490 ^{o}C might bring the insufficient mobility of group–III ad–atoms due to the low surface energy which may be the reason for the formation of defects while above 490 ^{o}C less availability of P_2 may cause the defects.

Chapter 6

GaAs quantum structures in the GaP matrix

In the 1980s, the advantages of using QDs in the optical devices such as injection lasers and light emitters were predicted theoretically. Narrower bandwidth, a higher characteristic temperature for threshold current, and lower threshold current were predicted as the characteristic advantages of the QDs lasers compared to the conventional QWs injection lasers [117]. Indeed, the provided higher density of states by the QDs close to the band edges (conduction or valence band) leads to the larger concentration of the injected charge carriers close to the bottom (top) of the conduction (valence) band. This, in turn, improves the gain and reduces the temperature dependence of the device [118]. Accordingly, QDs are introduced as the promising candidates to produce the new generation of high–performance light emitters. Numerous investigations were done on different semiconductor QDs particularly on the self–assembled III–V QDs systems [119, 120, 121, 122, 123, 124, 125, 126].

On the other hand, LEDs are beneficial devices with applications such as data transmission, information storage, and visible displays. The high output efficiency is the necessity factor of the LEDs that are applied for these applications [127, 128]. The low cost, well established, and simple production of LEDs based on III–V semiconductors make them interesting for most applications.

In this chapter, the results of the investigations on the structural and optical properties of self–assembled GaAs QDs in the GaP matrix will be discussed. In section 6.1, a brief overview of the accomplished investigations on the self–assembled QDs of III–V semiconductor in the GaP matrix will be given. Section 6.2 concentrates on the growth and characteristic properties of GaAs QDs on GaP(001) substrate. The electronic structure of GaAs/GaP is studied and the results of the simulations and the theoretical calculations for GaAs/GaP system will be described in section 6.2.1. In section 6.2.2, the growth and results of structural and optical properties of GaAs/GaP with respect to the nominal thickness of GaAs will be demonstrated. I will discuss the results of the studies on the influence of the growth temperature on structural and optical features of GaAs QDs in section 6.2.3. Section 6.3 will contain the results of our attempts to fabricate the LEDs based on the GaAs QDs. In this section, a short review of the investigations on the LEDs based on III–V semiconductors will be given. Afterward, I will explain briefly the grown structures

and the utilized processing methods. Then, the EL measurements will be explained. It is noteworthy that I grew the desired p–i–n heterostructures while, the LED fabrication, electrical and EL measurements on the fabricated mesas were done by C. Golz and a more detailed discussion can be found in his M.Sc. thesis [129]. The results will be summarized in section 6.4.

6.1 III–V semiconductors QD in a GaP matrix

Numerous studies were done on the growth and characteristic features of different III–V semiconductors QDs on GaP (001). The radiative recombination from InP QDs embedded in the GaP matrix was described in 2001. The formation of the InP QDs was related to the 7.7% lattice mismatch with GaP. A low density in the order 10^8 cm^{-2} was reported for InP QDs [125]. The observed PL peak at 2.0 eV was associated with the InP QDs [125]. The radiative transition in InP QDs was suggested to result from a direct type–I heterostructure, while a type–II system was offered for the 2D InP QW grown on GaP [130, 131, 132].

In 1998, Leon et al. investigated the formation of the self–assembled InAs QDs on GaP (001) substrates [124]. They reported that the 3D–islands of InAs are formed due to the 11% lattice mismatch with GaP in the Volmer–Weber growth mode and with a large inhomogeneous size distribution. A broad PL peak centering at 1.73 eV was measured at 77 K for InAs QDs and the broad FWHM of the detected peak was associated with the large inhomogeneous size distribution of QDs [124]. The 11% lattice mismatch of InAs with GaP, however, causes the formation of 90° dislocations [126, 133] that can act as the non–radiative recombination centers for optical purposes.

A suggested alternative to overcome the large lattice mismatch was In$_x$Ga$_{1-x}$As. Consequently, several investigations were done on growth and characterization of the In$_x$Ga$_{1-x}$As QDs on GaP. The lattice mismatch can be tuned with respect to the In content in this material system and it changes between 3.7% and 11% for x = 0 and x = 1, respectively [134, 135, 136, 138, 139, 140, 141, 142]. The results indicate that depending on the nominal content of In, density of QDs varies between a low amount of 1.5×10^{10} cm^{-2} [135] to the 1.6×10^{11} cm^{-2}. The emission line

of $In_xGa_{1-x}As$ QDs was reported to vary in the range of 1.76–2.0 eV depending on the In content and the size of QDs[136, 138, 139, 140, 141, 142, 143]. The incorporation of In atoms in the QDs, however, cannot be controlled precisely due to the In segregation and, consequently, the exact content of incorporated In in the QDs is less than the defined content [136, 142]. Stracke et. al demonstrated the difficulties to grow the $In_xGa_{1-x}As$ QDs directly on GaP (001) substrate. In order to grow the $In_{0.25}Ga_{0.75}As$ QDs on GaP(001) substrates, 3 ML of GaAs is needed as the interlayer between the GaP buffer and $In_{0.25}Ga_{0.75}As$ QDs [138, 141].

Investigations on GaAs/GaP material system are mostly concentrated on the QW or superlattice of thin GaAs layer [144, 145, 146, 147, 148]. According to these studies, a type–I to type–II transition with decreasing the thickness of strained GaAs QW is expected [144]. This transition is related to the decreasing of the separation between electron states at Γ– and X–valley and rise of the mixing probability due to the confinement effect [145, 147]. There are several investigations on the morphology and structural properties of GaAs QDs embedded in the GaP matrix [149, 150, 151]. According to literature review done by author, however, there are few studies on the optical characteristic of GaAs QDs grown on the GaP (001) substrates[152, 153]. Shamirzaev et.al reported the formation of GaAs QDs with a low density of 2×10^{10} cm^{-2} for 3 ML nominal coverage of GaAs. They reported an emission line at 1.96 eV at 5 K and suggested a type–I system for the relaxed GaAs QDs in GaP matrix, in which the minimum of the conduction band is located at the L–valley [152, 153]. More investigations, however, can lead to constructing a better explanation of the electronic and structural properties of the strained and partially relaxed GaAs QDs that may be a potential candidate for the LED fabrication. Fabrication of the LEDs based on the GaAs quantum structures in the GaP matrix will be described in this chapter.

6.2 GaAs/GaP heterostructure

6.2.1 Electronic structure of GaAs in the GaP matrix

The 3.7% lattice mismatch of GaAs with GaP induces a comprehensive strain to the GaAs layer grown on the GaP (001) substrates. This induced strain affects

the band alignment of GaAs/Gap heterostructure. To calculate the band alignment of the GaAs QDs with a large ratio of the diameter to the height, a GaAs QW with the same thickness as the height of QDs may be applied as a good approximation. Using this approximation and the solid–model theory [78], the band alignment of the system can be calculated. Fig. 6.1 shows the calculated band alignment of a 3 nm thick GaAs QW embedded in the GaP matrix. Accordingly, the strain causes the shift of the minimum of the conduction band of GaAs at Γ–valley to the higher energies. The X–valley of GaAs splits also to X_{xy} and X_z due to the biaxial strain. On the other hand, the valence band edge splits to two bands for hh and lh because of the biaxial strain. Fig. 6.1 a, and b show the results of the calculations for a fully relaxed, and a fully strained GaAs QW, respectively.

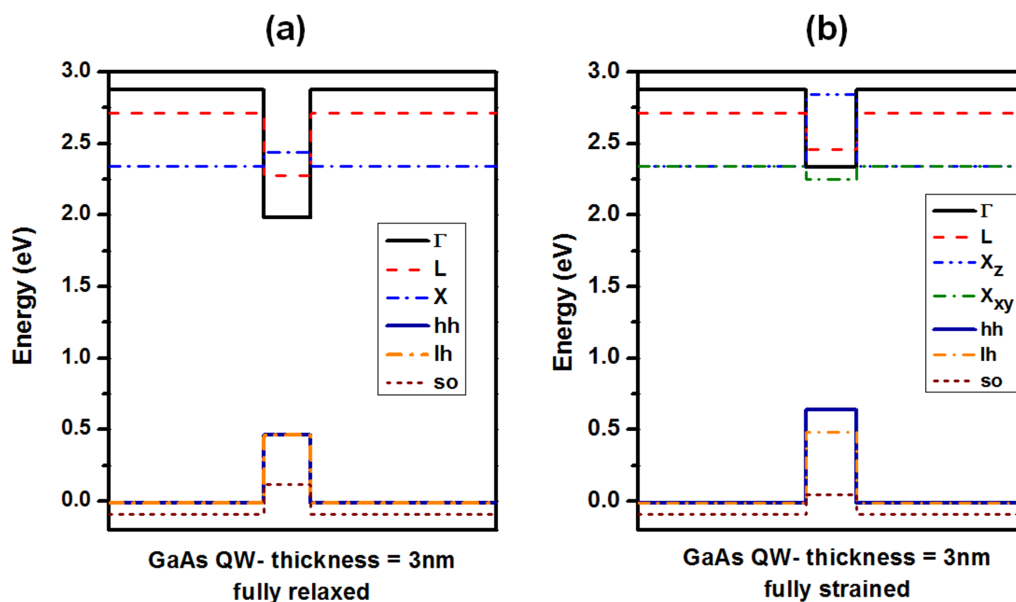

Figure 6.1: The band alignment of a 3 nm GaAs QW in the GaP matrix, (a) without considering the strain effect, (b) with considering the effect of the strain. The black, red, and blue lines represent the conduction band at Γ–, L–, and X–valley. The solid blue, orange and brown lines denote the hh, lh, and so valence band. The green dashed line in (b) is related to the X_{xy} component of GaAs X–valley.

The results indicate that for a fully relaxed system the GaAs/GaP heterostructure is a direct type–I system with the minimum of the conduction band and the maximum of the valence band at the Γ–valley of GaAs. The conduction band of

GaAs Γ–valley is 370 eV lower than the conduction band edge of GaP at X–valley. In the case of the fully strained system, however, the conduction band edge of GaAs at Γ–valley is very close (10 meV lower than) to the minimum of the conduction band of GaP at X–valley. The component of the X–valley of GaAs in the growth direction (X_z) is located at higher energy than the Γ–valley of strained GaAs while the X_{xy}–valley of GaAs is the minimum of the conduction band [147]. Popescu et. al declares that the electron states in the Γ–Valley of the strained GaAs are in resonant with the GaP continuum. This, in turn, leads to the weakly coupled e^{Γ}–e^{X_z} states [154]. Therefore, an indirect type–II system is suggested for the fully strained GaAs in the GaP matrix.

Strain, however, can be released via the formation of QDs. Therefore, it can be suggested that the increase of the size of GaAs QDs might lead to the transformation of the system from a fully strained system toward the partially relaxed and finally, the fully relaxed system. The variation of the strain in addition to the quantum confinement effect can change the electronic structure of the system from a type–II and indirect transition to a type–I and direct transition of electron and holes. Fig. 6.2 shows the results of the calculated transition energy between the e– and hh–states with respect to the strain for two different thicknesses (0.3 nm, and 3.0 nm) of GaAs QW. The calculations were done using the 1 band–k.p approach and effective mass approximation [79]. The red circles are related to the transition energy of the e^{X}–GaP and hh^{Γ}–GaAs, while the blue triangles are associated with the transition energy of $(e–hh)^{\Gamma}$ of GaAs. The results demonstrate that for a 0.3 nm GaAs QW, in the range of the fully strained to the fully relaxed system, the transition energy of e^{X} and hh^{Γ} occurs at lower energy than $(e–hh)^{\Gamma}$–GaAs. Therefore, it can be concluded that the expected radiative transition corresponds to the e^{X}–hh^{Γ} states. The calculated results for a 3.0 nm GaAs QW, however, indicate that with reducing the strain degree, system changes from a type–II indirect to a pure type–I direct. The transition energy of e^{X}–hh^{Γ} is equal to the transition energy of $(e–hh)^{\Gamma}$ for the 50% relaxed system. The favorable radiative transition, therefore, can be related to $(e–hh)^{\Gamma}$ states of GaAs QW for 50% relaxed system.

Consequently, the radiative band to band transition in GaAs/GaP system may

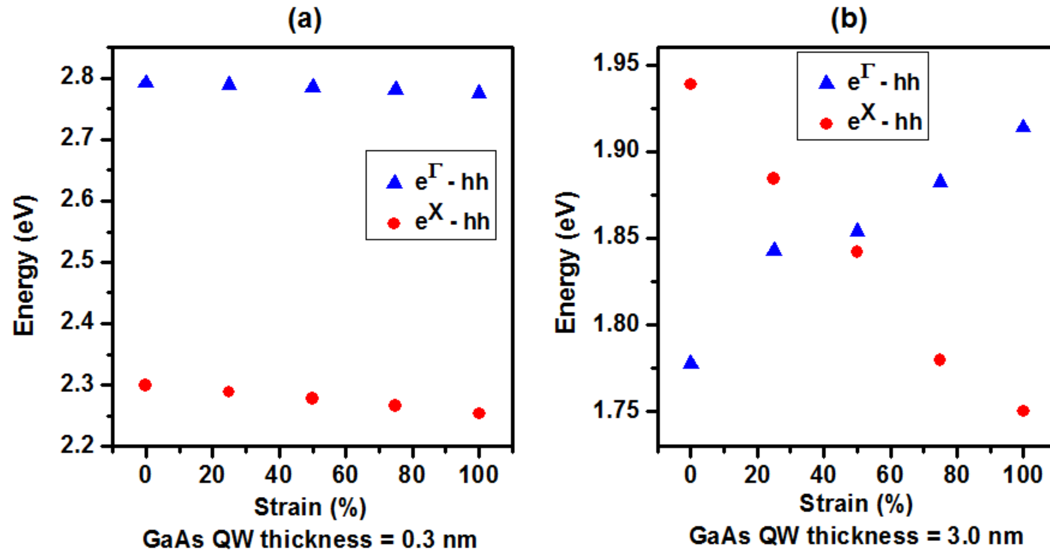

Figure 6.2: The transition energy for a GaAs QW with thickness (a) of 0.3 nm, and (b) 3.0 nm with respect to the strain. The red circles are related to the transition between the electrons at X–valley of GaP and hh at Γ–valley of GaAs, while the blue triangles show the transition between electron and hh at Γ–valley of GaAs. Strain = 0% corresponds to the fully relaxed system and Strain = 100% demonstrates the fully strained system.

transfer from a resonant $e^{\Gamma-X}$–states with hh^{Γ}–states transition [154] to a direct type–I $(e\text{–}hh)^{\Gamma}$ transition with increasing the relaxation degree of QDs. The rise of the relaxation degree, in turn, may occur via the formation of the larger QDs.

6.2.2 Growth and characterization of GaAs QDs on GaP (100) substrate

To test the theoretical model, structures were grown using a Riber–32P GSMBE system on 400 μm thick GaP (001) undoped substrates. The native oxide layer on GaP substrate was removed by heating the substrate up to 610 ^{o}C and under a PH_3 over pressure. The temperature was measured using a thermocouple located directly behind the GaP substrate held by its rim. Afterward, 0.5 μm GaP buffer layer with the growth rate of 0.83 μm/h was grown at 520 ^{o}C under 2.7 sccm PH_3 flux. Then, the growth was interrupted while the substrate temperature was reduced to 450 ^{o}C. Afterward, the desired thickness of GaAs layer was grown under 2.5 sccm

AsH_3 and with the growth rate of 0.3 ML/s (about 0.31 μm/h). The resulting structures then were capped with 50 nm GaP that was grown at 520 ^oC, using a PH_3 flux of 2.7 sccm and the growth rate of 0.83 μm/h (Fig. 6.3). To study the influ-

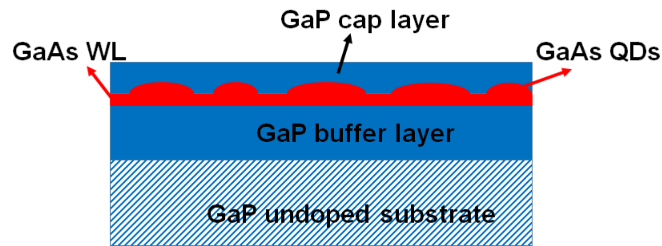

Figure 6.3: Scheme of grown structure. Each sample consists of 500 nm GaP undoped buffer layer and 50 nm GaP undoped cap layer and the desired thickness of GaAs layer was grown between these layers.

ence of the nominal thickness of GaAs on both structural features, such as shape, size, density, and optical properties of GaAs quantum structures, four samples with different GaAs nominal thicknesses between 1.2 to 3.6 ML were grown. Samples then were capped for optical measurements while equivalent growth processes were performed to grow the uncapped GaAs layer for AFM measurements.

The RHEED technique was utilized to monitor the growth processes. Fig. 6.4 shows the RHEED pattern of (a) GaP layer before deposition of GaAs layer, and (b) after growth of 3.6 ML GaAs. The results indicate the transition of RHEED from a sharp line pattern for the GaP buffer layer reconstruction to the broken lines reconstruction after the deposition of 3.6 ML of GaAs layer. Consequently, it can suggest the formation of 3D islands of GaAs that can be driven due to the 3.7% lattice mismatch of GaAs with GaP. The RHEED pattern, however, does not show this transition for 1.2 ML deposited GaAs, while a pattern with the broken lines was observed for the 1.8 ML grown GaAs layer. This can be related to the SK growth mode. Therefore, the first ML of GaAs is grown on GaP substrate as a 2D fully strained layer. For larger thickness than the critical thickness, the driven strain due to the lattice mismatch is released via the formation of the 3D QDs of GaAs.

The AFM results are consistent with the RHEED patterns (Fig. 6.5).

Fig. 6.5a shows a flat surface after deposition of 1.2 ML GaAs while the formation of small GaAs QDs is observed for the deposited GaAs with nominal thick-

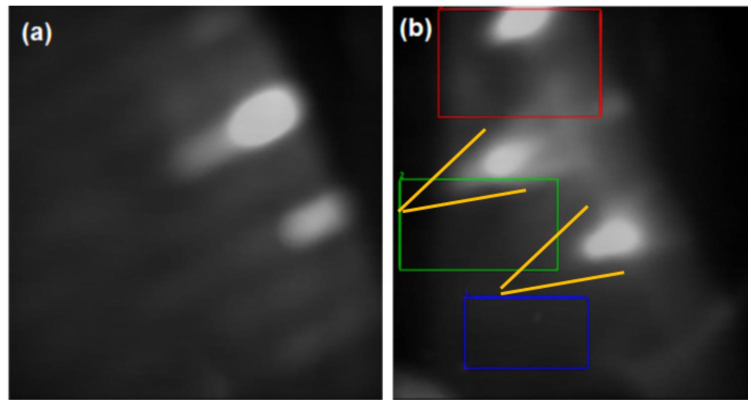

Figure 6.4: RHEED pattern (a) the streaky pattern of GaP buffer layer reconstruction before GaAs deposition, and (b) the broken lines reconstruction after deposition of 3.6 ML of GaAs.

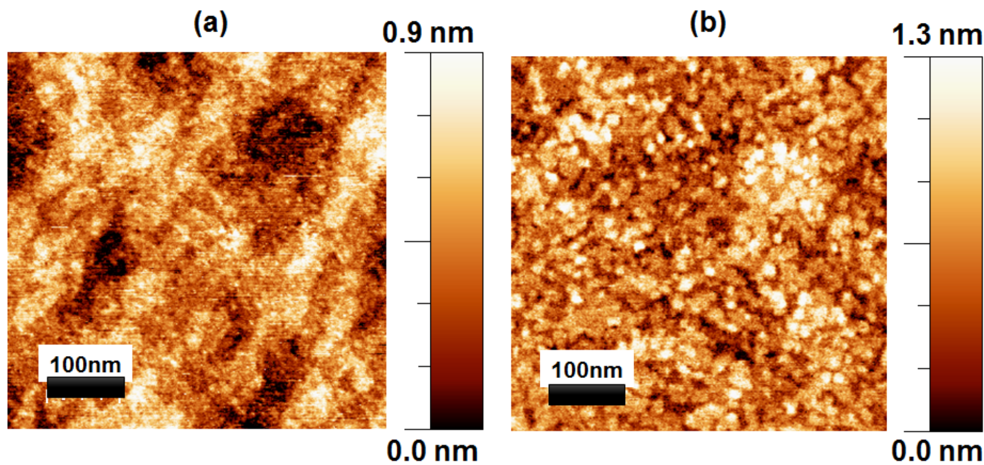

Figure 6.5: AFM results of GaAs layer with different nominal thicknesses grown on GaP (001). (a) 1.2 ML, 3D islands are not formed, (b) 1.8 ML, 3D islands are observed.

nesses larger than 1.2 ML. Fig. 6.5b illustrates the AFM scan for the sample with GaAs nominal thickness of 1.8 ML. The scan size for both images is 0.5×0.5 μm. It is noteworthy that the AFM measurements were carried out in IKZ with the assistance of Dr. J. Schmidtbauer. The results show that the lateral size of QDs increases with nominal thickness from averaged diameter of 18 nm in the case of 1.8 ML GaAs to 35 nm for 3.6 ML samples. The same tendency is seen for the QDs height. The averaged height is 0.9 nm for 1.8 ML while it rises to 2 nm for 3.6 ML sample(Fig. 6.6).

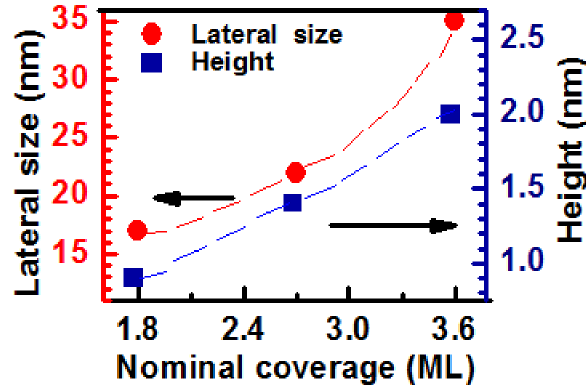

Figure 6.6: Average height and diameter of QDs with respect to the nominal thickness of GaAs. Both vertical and lateral size of QDs increases with nominal thickness. The dash lines are for eye guide.

The AFM analyses demonstrate that for 2.7 ML and 3.6 ML GaAs samples the lateral and vertical size distributions are multimodal. However, a Gaussian size distribution fits better to 1.8 ML sample. Fig. 6.7 shows the size distribution of QDs in both lateral and vertical directions. The density of the QDs is $7.0\pm0.2\times\ 10^{10}$ cm^{-2} for 1.8 ML nominal thickness of GaAs. The density increases to $7.6\pm0.2\times10^{10}$ cm^{-2} for 2.7 ML, whereas it reduces to $6.0\pm\ 0.2\times10^{\ 10}$ cm^{-2} with increasing the nominal thickness to 3.6 ML. The multimodal size distribution of the QDs can be described using two distinct thresholds for the formations of QDs. The first threshold can be related to the GaAs nominal thickness for the formation of QDs while the second one may be associated with the nominal thickness for the formation of QDs with equilibrium islands size [155]. The lower density of the QDs for 3.6 ML compared to the 2.7 ML sample, therefore, might be due to the formation of QDs with equilibrium islands size and 1.6 times larger lateral size. To estimated the WL thickness using the AFM results, QDs were considered as a half of an ellipsoid. Therefore, the volume of the QDs was assumed to be equal to the half of the volume of an ellipsoid. Here, the lateral size of QDs was considered as the diameter of ellipsoid and their height was assumed as the height of the ellipsoid. The calculated WL thickness reduces from 0.4±0.05 nm for the 1.8 ML to 0.2±0.02 nm for the 3.6 ML nominal thickness of GaAs. The reduction of the WL

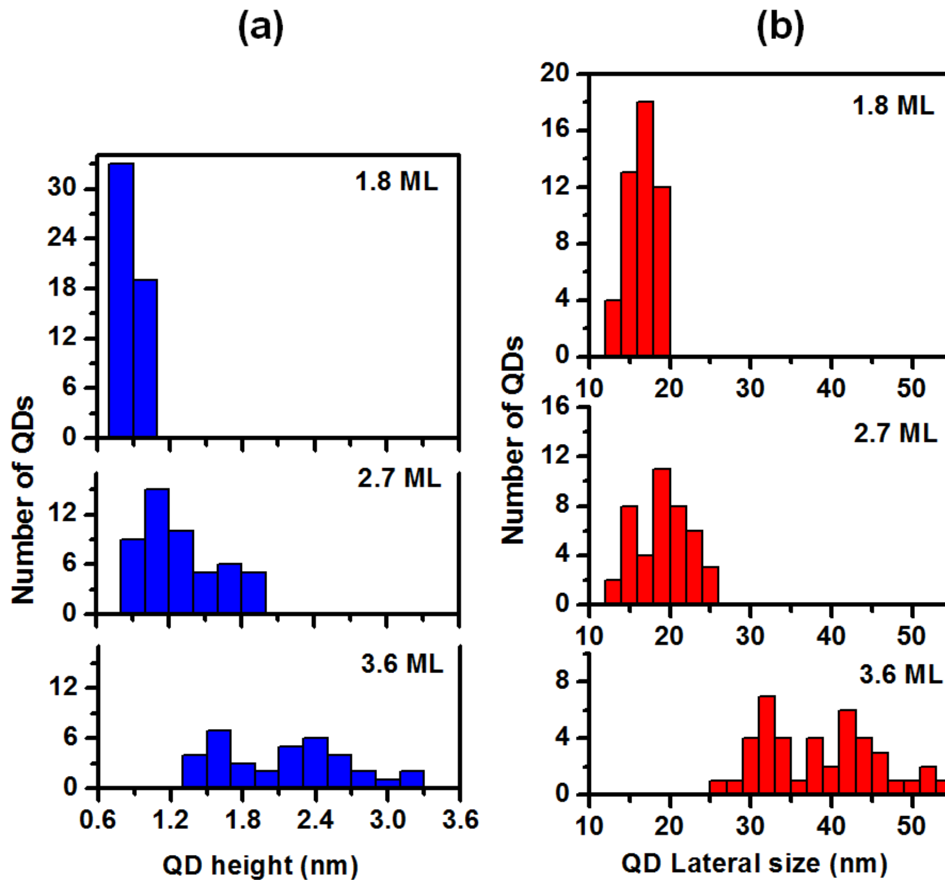

Figure 6.7: (a) The vertical and (b) the lateral size distributions of GaAs QDs for different samples with GaAs nominal thicknesses of 1.8, 2.7, and 3.6 ML.

thickness for 3.6 ML samples is associated with the formation of larger QDs.

Fig. 6.8 illustrates the cross section High–Angle Annular Dark–Field Scanning Transmission Electron Microscopy (HAADF STEM) image of the sample with 1.8 ML GaAs nominal thickness. The measurements were done by Dr. A. Mogilatenko in TEM in the Physics institute of Humboldt University. The results of HAADF STEM measurement are consistent with the AFM. Accordingly, the formation of GaAs QDs on GaAs WL occurs for the 1.8 ML nominal thickness of GaAs layer. Consequently, it can be concluded that the growth of QDs occurs in the SK growth mode. A lens shape QD with the height of about 0.9±0.1 nm is observed and the WL thickness is about 0.4±0.05 nm. The 2D GaAs WL and the small QDs are fully strained.

The optical characterizations were carried out using CL and PL measurements

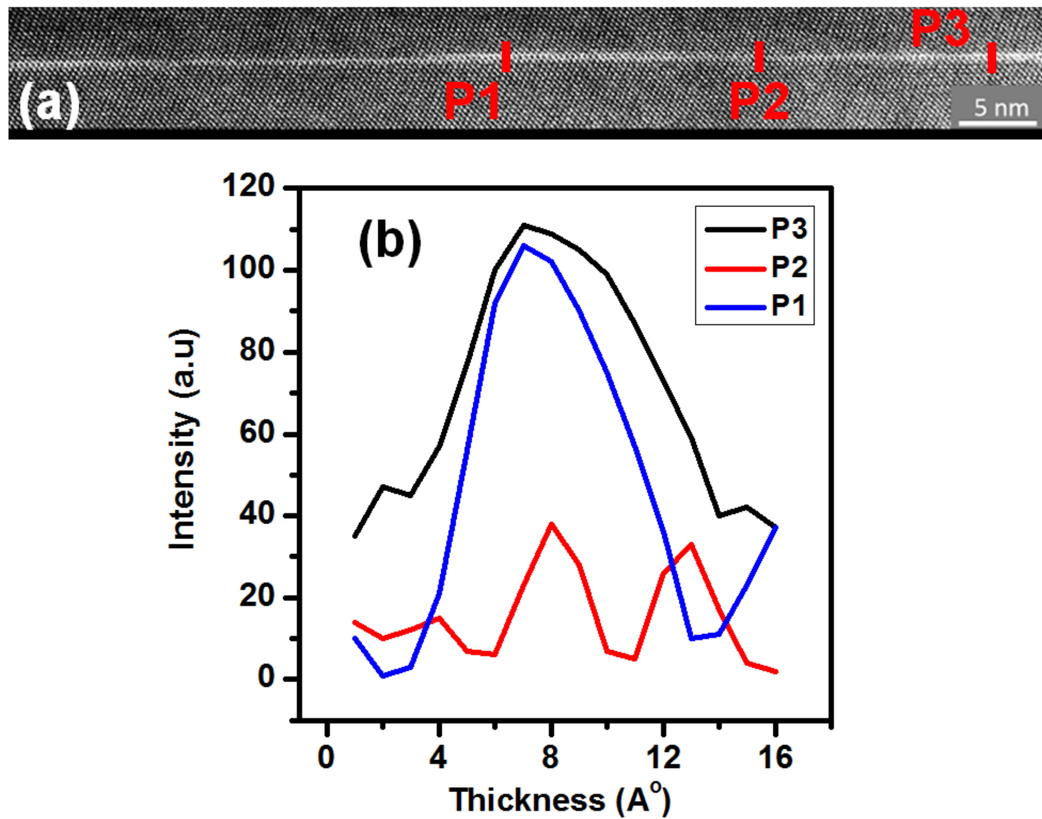

Figure 6.8: (a) HAADF STEM image of the sample with 1.8 ML GaAs nominal thickness. GaAs wetting layer and lens shape QDs are seen. (b) The line scan profile of the image for three different points of P1, P2, and P3. The QDs have short height of 9.0±0.1 nm.

and the collected results from both measurements confirm each other. The CL measurements were done in Valladolid University in the group of Prof. J. Jimenez. The measurements were carried out using a XiCLOne (Gatan UK) CL system attached to an LEO 1530 (Carl–Zeiss) field–emission scanning electron microscope(FESEM). The luminescence signal was detected with a Peltier–cooled charge–coupled device camera (CCD) allowing the acquisition.

The advantage of CL compared to the other optical measurement is that the different layers of the structure can be studied with respect to the applied acceleration voltage. In fact, acceleration voltage determines the penetration length of the electron beam and, therefore, depth of excitation (more discussions in 3.2.1). The Monte Carlo Simulation of electron trajectory in solids (CASINO) of a heterostructure composed of a 500 nm GaP buffer layer, a thin GaAs layer (2 nm), and 50 nm

GaP cap layer, indicates that 75 to 90% of collected CL spectrum corresponds to the thin GaAs layer when the excitation energy is in the range of 5–10 keV [56]. Fig. 6.9 shows the map of energy distribution calculated using CASINO with respect to the excitation depth and lateral distribution [56]. Here, it was assumed that the defined heterostructure is excited using a 5 keV excitation energy. The results indicate that 90% of collected information is associated with the GaAs and GaP cap layer. The CL results of the sample with 2.7 ML GaAs is shown in Fig. 6.10. The

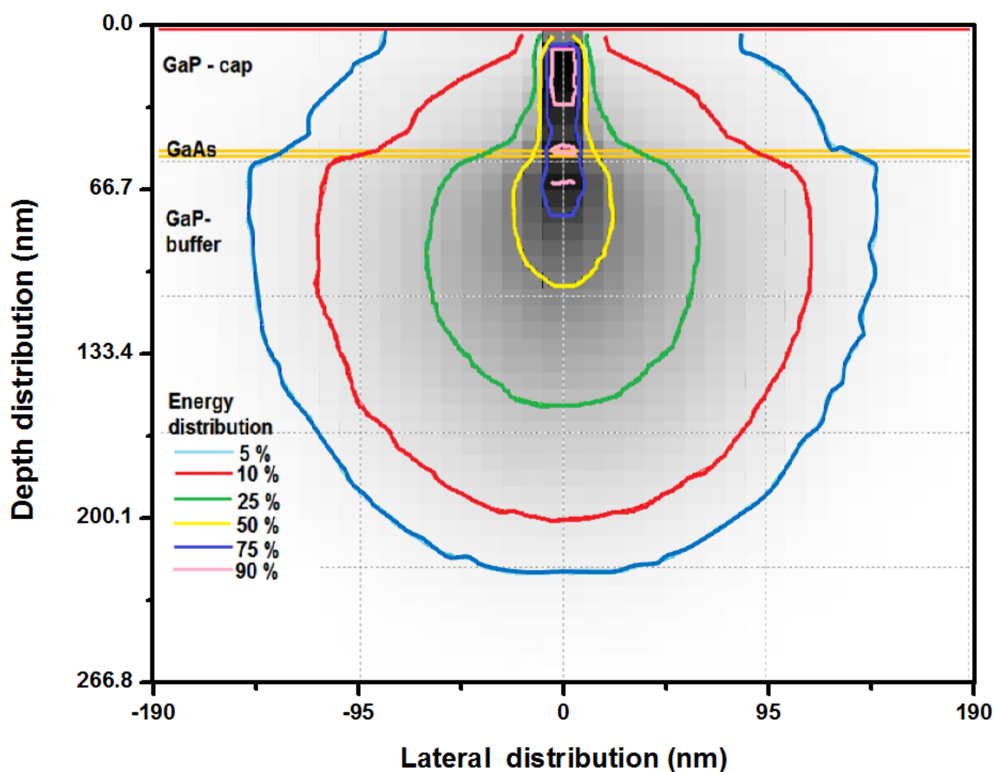

Figure 6.9: Results of casino simulation for a heterostructure composed of GaP substrate, 500 nm GaP buffer layer, 2 nm GaAs QW, and 50 GaP cap layer that is excited using a 5 keV excitation energy. Results indicate that 90% of collected information is related to the GaAs and GaP cap layer.

measurements were carried out at 80 K and under different excitation energy in the range of 1–20 keV. The results of the simulations demonstrate that the penetration depth of the electron beam of 1 keV is almost 20 nm and consequently the spectrum must be related to the GaP cap layer.

The CL results do not show any radiative transition peak when the sample is excited using an electron beam of 1 keV. This can be related to the surface states,

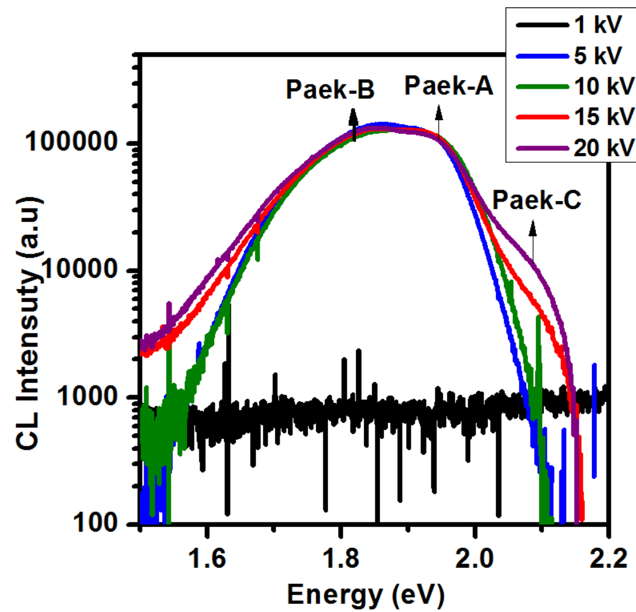

Figure 6.10: CL results of the sample with 2.7 ML GaAs nominal thickness. Measurements were carried out at 80 K and under different electron beam energies in the range of 1–20 keV.

which act as the non–radiative recombination centers. A broad spectrum is observed under 5 keV and 10 keV excitation energies. This broad spectrum contains two emission lines that can be fitted using two Gaussian, peak–A and peak–B. According to the simulation results, 75–90% of the detected spectrum under 5–10 keV electron beam energy is related to the GaAs layer. Therefore, it can be suggested that the origin of peak–A and –B is the radiative recombination in the GaAs QDs. The results of the simulations demonstrate that the penetration length of the electron beam is longer than 500 nm for the acceleration energy in the range of 15–20 keV. Therefore, the GaP substrate can be excited and the third peak (peak–C) at about 2.10 eV may be related to the radiative recombination in the shallow defects in the GaP substrate [2]. In this thesis, the results of the CL measurements carried out under 5 keV excitation energy were utilized for discussions.

Fig. 6.11 shows the CL results of radiative transitions of four samples with different nominal thickness at 80 K. The CL spectrum of a GaP epitaxial layer is shown for comparison. The spectra were fitted using the Gaussian peaks. The corresponding fitted peaks are also shown in Fig. 6.11. The corresponding spectrum

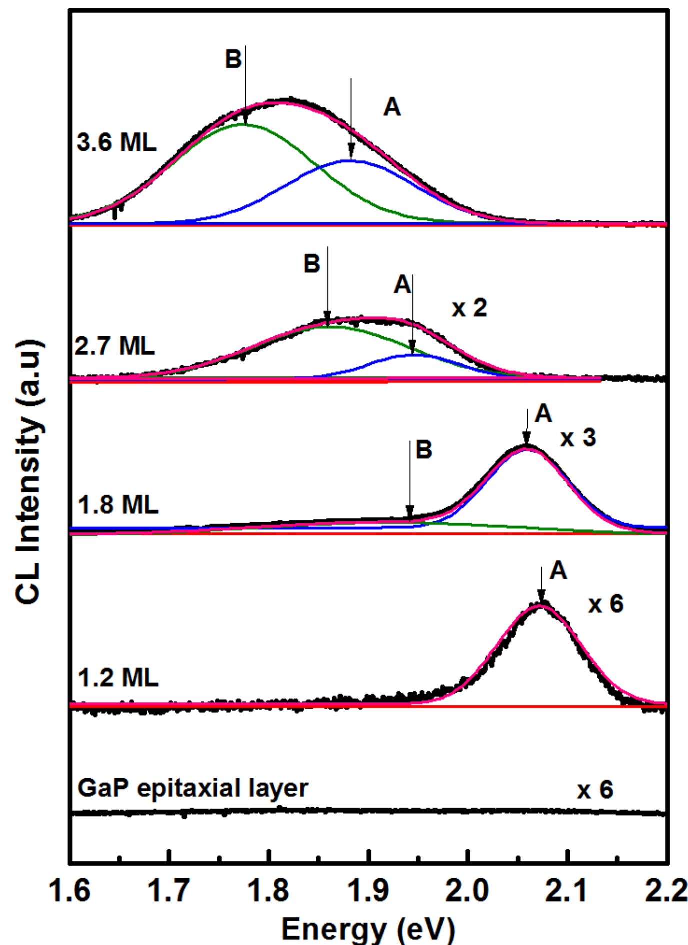

Figure 6.11: CL results of four samples with different nominal thickness in the range of 1.2–3.6 ML. CL spectrum of GaP buffer layer is shown for comparison. One sharp peak is observed for 1.2 ML GaAs, while two peaks (–A and –B) are observed for the other 3 samples. The spectra were fitted using the Gaussian peaks. Blue curve shows peak–A while green curve corresponds to peak–B.

of the GaP epitaxial layer does not demonstrate any emission line between 1.6 eV to 2.2 eV. The CL results of the 1.2 ML GaAs sample, however, indicates a single emission line at 2.07 eV. The AFM results show a flat structure for 1.2 ML GaAs sample and, therefore, the radiative transition of this sample may be attributed to the thin GaAs QW. For the samples with nominal thicknesses above 1.2 ML and containing QDs, CL spectra demonstrate the broad spectra. These broad spectra were fitted by two Gaussian peaks that are denoted as peak–A and peak–B (Tab. 6.1). The emission lines show an overall redshift with increasing the nominal thickness.

The first emission peak at higher energies (peak–A) shifts from 2.06 eV (1.8 ML sample) to 1.88 eV (3.6 ML sample) and the peak–B shifts from 1.93 eV (1.8 ML sample) to 1.78 eV (3.6 ML sample). This overall redshift is associated with the formation of larger quantum structures with increasing the nominal thickness that is confirmed by the AFM results.

Table 6.1: The energy position of peak–A and –B for four samples with different GaAs nominal thickness in the range of 1.2–3.6 ML.

nominal coverage (ML)	**Peak–A (eV)**	**Peak–B (eV)**
1.2	2.07	—-
1.8	2.06	1.92
2.7	1.94	1.84
3.6	1.89	1.78

Temperature dependent measurements were carried out using a PL setup equipped with a He–Cd laser with excitation energy of 3.81 eV (λ = 325 nm). Samples were mounted inside a cryostat and measurements were done in the range of 10–300 K. Dr. P. Corfdir in Paul Drude Institute assisted me for doing the measurements. Fig. 6.12a shows the results for the sample with 3.6 ML GaAs. The thermal quenching of the PL and the shift of the spectra with increasing the temperature are observed. Both peak–A and peak–B shift toward lower energy (redshift) with increasing the temperature (Fig.6.12b). The redshift of both peaks corresponds with the shift of the bandgap energy of III–V semiconductors with temperature [65]. The total intensity of radiative recombination reduces with increasing the temperature that is related to the increase of the probability of non–radiative recombination, such as Auger recombination, at higher temperatures.

Temperature dependent CL measurements confirm the redshift and thermal quenching of the luminescence with increasing the temperature. The results indicate that the radiative recombination vanishes at temperature higher than 150 K for the samples with nominal GaAs thicknesses of 1.2 ML and 1.8 ML. The samples with the nominal thicknesses above 1.8 ML emit light at 300 K. Fig. 6.13 shows the up to room temperature CL spectra of the 2.7 ML and 3.6 ML samples.

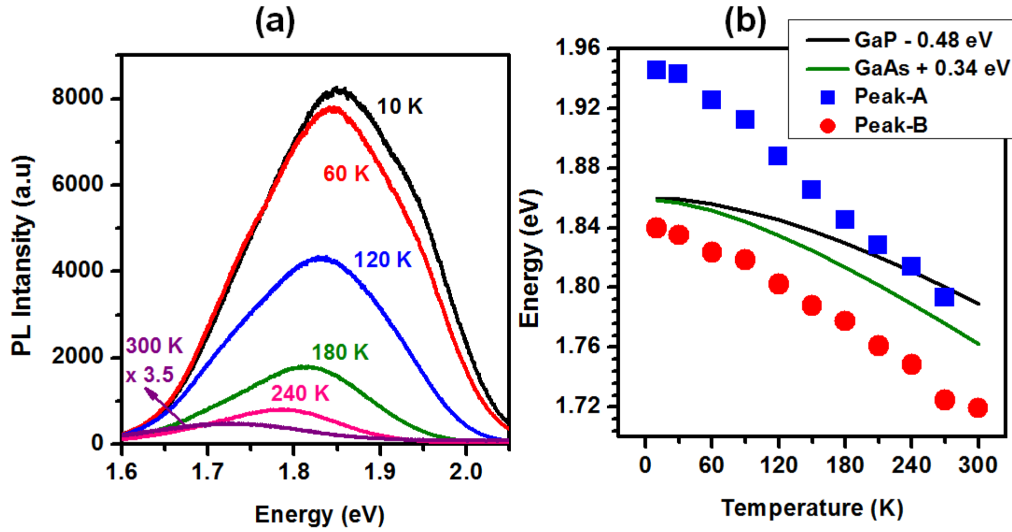

Figure 6.12: Temperature dependent PL measurements of 3.6 ML GaAs. (a) The Intensity reduction and the overall redshift is observed with increasing the temperature, (b) the redshift of both peak–A (red circles) and peak–B (blue squares) with increasing the temperature. The shift of the bandgap energy of bulk GaAs (green line) and GaP (black line) is illustrated for comparison.

The total intensity quenching of the radiative recombination with respect to the temperature are shown in Fig. 6.14a for three different samples. Apparently, the thermal quenching rate of the luminescence is less for the thicker GaAs coverage. For instance, the light output of 2.7 ML sample decreases about 30 times and for 3.6 ML sample, the output reduction is about 15 times. Consequently, it can suggest that due to the increase of the relaxation degree for the larger GaAs QDs, which causes the downward shift of the conduction band edge of GaAs at Γ–valley, the charge carriers confinement, particularly for electron, is enhanced.

The activation energies of the charge carriers can be determined using the Arrhenius plot [156, 157]. The variation of integrated intensity with increasing the temperature can be fitted using the following equation:

$$\frac{I}{I_0} = \frac{1}{(1+\sum_{i}^{n} c_i exp(\frac{-E_i \times 11604}{T}))} \tag{6.1}$$

Here, I denotes the integrated intensity of corresponding peak (peak–A or peak–B) at the different temperatures. I_0 is the integrated intensity of peak–A (or peak–B)

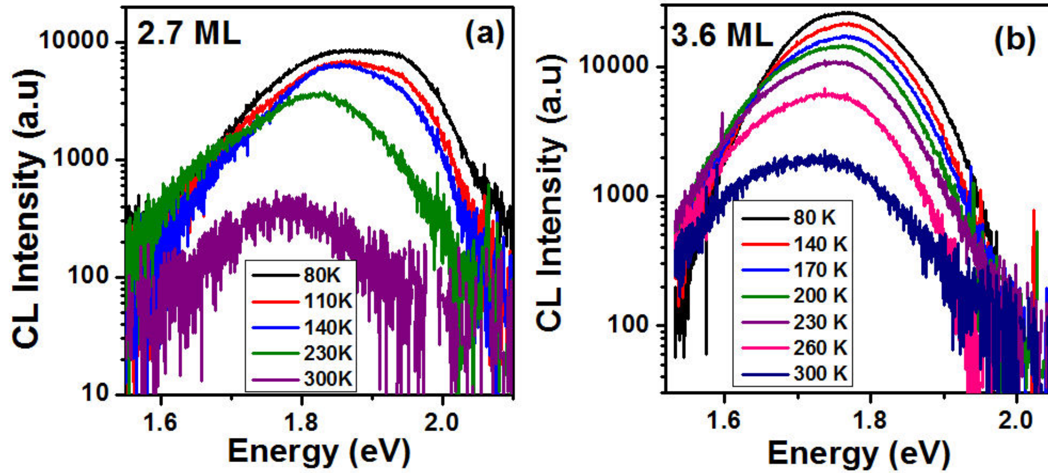

Figure 6.13: Temperature dependent CL spectra in the range of 80 - 300 K for (a) 2.7 ML sample, and (b) 3.6 ML sample.

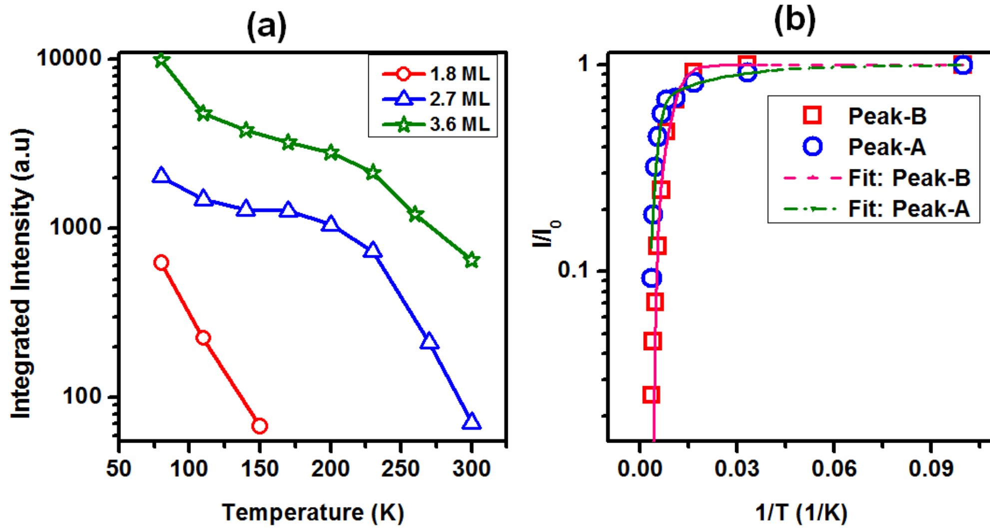

Figure 6.14: (a)The total quenching of the luminescence with increasing the temperature. empty circles (red), empty triangles (blue), and stars (green) denote the total integrated intensity with respect to the temperature for 1.8 ML, 2.7 ML, and 3.6 ML samples respectively. (b) Arrhenius plot of the integrated intensity of the 3.6 ML samples. Lines show the fitted curve.

at 10 K and T represents the temperature in K. E_i denotes the activation energy of the corresponding peak, while c_i is a constant, which denotes the carriers escape efficiency of the QDs, and n defines the level. Fig. 6.14b shows the integrated

intensity variation with respect to the temperature for 3.6 ML sample. The lines show the fitted curve using 6.1. The results for E_i and c_i are summarized in Tab. 6.2. The activation energy increases with increasing the nominal thickness of GaAs. The downward shift of the conduction band edge of GaAs atΓ–valley with increasing the relaxation degree due to the formation of larger QDs may lead to the larger activation energy for electrons to escape from GaAs QDs.

Table 6.2: The obtained activation energies, E_1 and E_2, and the corresponding c_i constant using the Arrhenius plot [156, 157].

Nominal thickness (ML)	**Peak–A**		**Peak–B**	
	E_1 **(meV)**	E_2 **(meV)**	E_1 **(meV)**	E_2 **(meV)**
2.7	6	—	6	83
3.6	7	141	27	182

Nominal thickness (ML)	**Peak–A**		**Peak–B**	
	c_1	c_2	c_1	c_2
2.7	52.4	—	1.9	696.3
3.6	1.0	4.0×10^3	20.7	7.5×10^4

The integrated intensity of the peak–A of the 2.7 ML GaAs sample was fitted only with one activation energy. The obtained low activation energy means the fast thermal quenching of this peak. For peak–B, however, the intensity quenching is well fitted by two activation energies. The first activation energy is weak with a small escape efficiency (c_1). Therefore, the small intensity reduction at temperatures lower than 120 K can be associated with the weak escape efficiency (c_1). The second activation energy is strong with a large escape efficiency and, therefore, it has a significant influence on the thermal quenching of the output intensity. A similar tendency has been seen for the activation energies of the peak–A and peak–B of the 3.6 ML sample. The larger activation energies for both peaks compared to the 2.7 ML sample can be associated with the slower rate of thermal escape of the carriers in the 3.6 ML sample. This corroborates the CL results of the variation of the integrated intensity with temperature, which shows 2 times less quenching

rate for the 3.6 ML sample than 2.7 ML sample. According to our calculations, the height of the barrier for the ground sate of hh (first energy level of hh - band edge of the GaP valence band) is about 2.2 times larger than the experimental activation energy (E_2). The calculated barrier height of the ground sate of hh is about 400 meV for a relaxed QW with thickness in the range of 2–3 nm. Therefore, it can be suggested that the experimental activation energy is related to the required energy for the thermal escape of electrons from the Γ–valley of the relaxed GaAs QDs.

The excitation density dependent PL measurements were carried out in the group of Prof. J. Jimenez. The measurements were done at 80 K using an excitation energy of 3.81 eV (λ = 325 nm) (Fig. 6.15).

The peak position of 1.8 ML GaAs sample shifts linearly toward higher energy range with increasing the excitation density with power of 1/3 from 0.149 $(\text{Wcm}^{-2})^{1/3}$ to 1.8 $(\text{Wcm}^{-2})^{1/3}$ (Fig. 6.15b). The linear blueshift with increasing the excitation density is a well–known behavior for a type–II heterostructure [158, 159]. The significant shift of 40 meV toward higher energy with increasing the excitation density, therefore, may be related to an indirect type–II system. For the nominal thicknesses above 1.8 ML GaAs the position of the transition line at higher energy, peak–A, illustrates a linear blueshift with increasing the excitation density. The blueshift is about 20 meV for 2.7 ML sample and it is about 40 meV for the 3.6 ML sample. The peak position linearly shifts with excitation density to the power of 1/3 up to 1.8 $(\text{Wcm}^{-2})^{1/3}$. The position of peak–B, on the other hand, does not vary significantly for different excitation density (Fig. 6.15 c and b). The shift toward higher energy is about 6 meV for both 2.7 ML and 3.6 ML samples. The small blueshift with increasing the excitation density might be due to the occupation of higher energy states in smaller QDs [158]. Therefore, it may be suggested that the GaAs/GaP heterostructure transforms from a type–II and indirect transition in the case of 1.8 ML sample to a mixed direct type–I and indirect type–II system with increasing the size of GaAs QDs for larger nominal thickness (2.7 ML and 3.6 ML) of GaAs layer.

The dynamics of relaxation and recombination of charge carriers were studied using the time–resolved photoluminescence spectroscopy in collaboration with

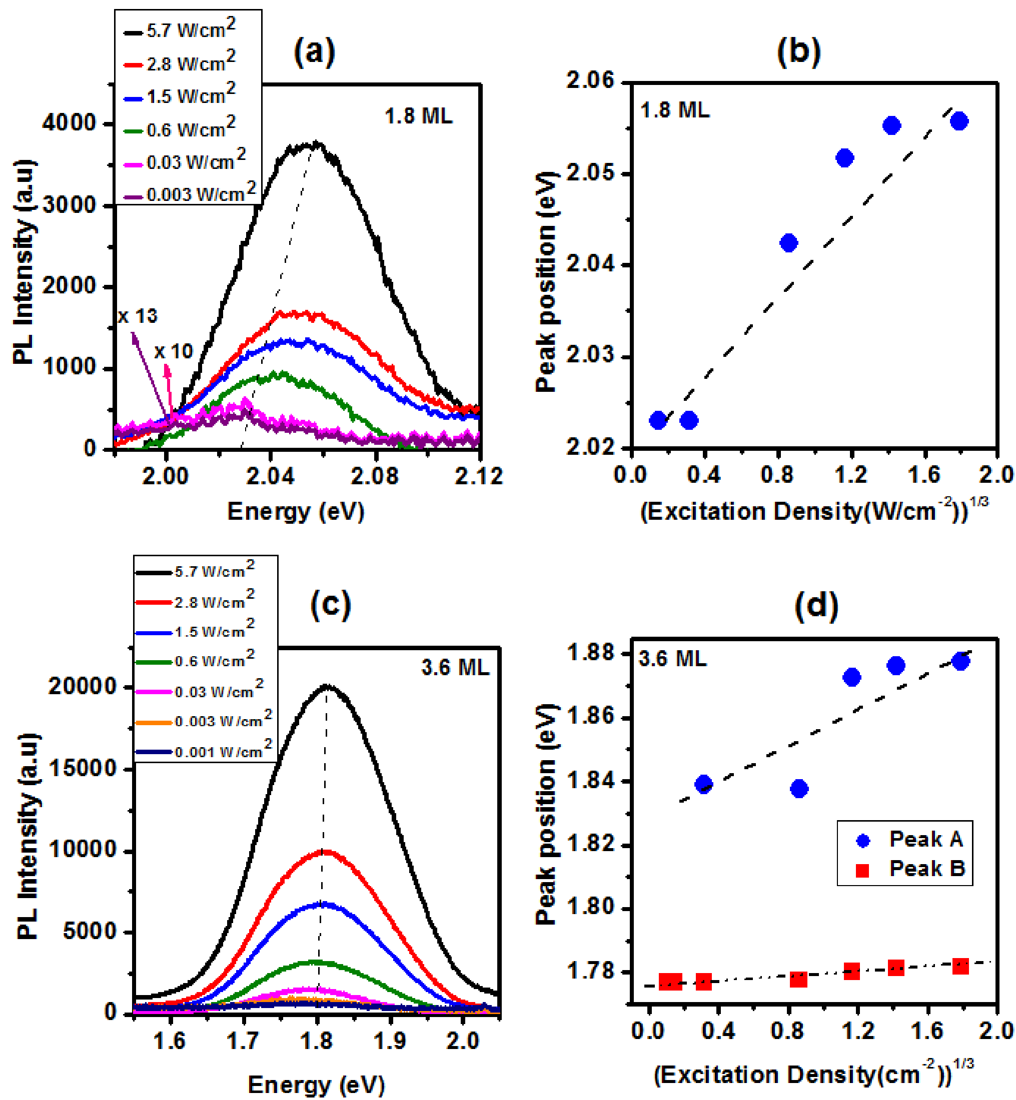

Figure 6.15: Results of excitation density dependent PL. (a), and(c) show spectra for 1.8, and 3.6 ML samples, respectively. (b), and (d) present the variation of the peak positions with respect to the excitation density to the power of 1/3. The blue circles represent the position of peak–A and peak–B position is shown by the red squares. The dash lines are for eye guide.

the Max–Born Institute in Berlin with assistance of Dr. J. Tomm. The measurements were carried out in a He–cryostat using a pulse laser with the repetition rate of 80 MHz and excitation wavelength of 388 nm and excitation density of 120 (Wcm^{-2}) in the range of 5–300 K. Fig. 6.16a presents the PL intensity decay of 3.6 ML sample at 75 K for two emission peaks–A and –B. The transients were fitted by a simple exponential decay with a single time constant. Fig.6.16b summa-

rizes the decay time for three different samples with respect to the emission energy. For each sample, the higher–emission energy, the slower the decay time. With increasing the nominal thickness of GaAs from 1.8 ML to 3.6 ML the decay time for the peak–A reduces from 8.5 ns to 6.0 ns. The decay time of peak–B changes from 5.0 ns for 2.7 ML sample to 2.4 ns for 3.6 ML sample. A model of interdot carri-

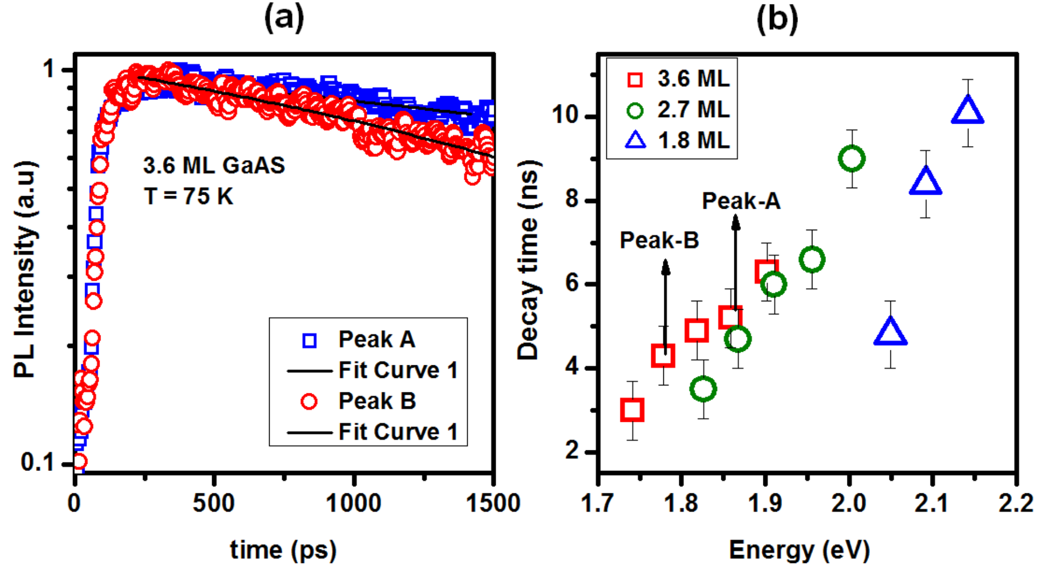

Figure 6.16: (a) Time–resolved PL spectra of the 3.6 ML sample for two emission peak maxima A (blue circles) and B (red squares) at 75 K with their corresponding fits (black lines). The decay time of peak A is 5.5 ns and for peak B 2.4 ns. (b) PL Decay times of 1.8, 2,7, and 3.6 ML samples for different emission energy at 75 K.

ers transfer is utilized for the dense array of QDs (density higher than 10^{10} cm^{-2}) [160, 161, 162, 155, 163]. The carrier relaxation, therefore, in this model can occur via (1) the radiative recombination in the QDs levels and/or (2) carrier in the energy level of ground states of small QDs relax to the energy levels of the larger QDs. Based on these assumptions, the carrier relaxation rate from an energy level in a QD is proportional to the number of unoccupied states in the adjacent QDs and can be written as [160]:

$$\frac{dn_i}{dt} = -\frac{n_i}{\tau_0^i} - \sum_{j<i} \frac{n_i D_i}{\tau_t^{ij}} + \sum_{i<j} \frac{n_j D_j}{\tau_t^{ij}} \tag{6.2}$$

Here, τ_0^i is the total recombination lifetime in the ith ground state, τ_t^{ij} is the interdot

carrier transfer time between E_i and E_j states, D_j is the density of the final E_j states. In this model, the saturation condition is needed to be considered to have a realistic description for the charge carrier relaxation mechanisms. The saturation limit occurs when the number of nonequilibrium carriers in n_i is equal to the available QDs ground states of N_j in the jth dots distribution. Equation 6.2, therefore, must be modify with considering the saturation limit [160].

$$\frac{dn_i}{dt} = -\frac{n_i}{\tau_0^i} - \sum_{j<i} \frac{n_i(N_j - n_j)D_i}{\tau_t^{ij}} + \sum_{i<j} \frac{n_j(N_i - n_i)D_j}{\tau_t^{ij}} \tag{6.3}$$

The filling parameter is defined as:

$$\delta = \frac{N_i - n_i}{N_i} \tag{6.4}$$

Tow different limits can be assumed:

- Weak saturation limit, in which:

$$N_i \gg n_i \Rightarrow \delta \to 1 \tag{6.5}$$

- Strong saturation limit, where:

$$N_i = n_i \Rightarrow \delta = 0 \tag{6.6}$$

The weak saturation limit can happen for low excitation density, where the transfer of the charge carriers from small QDs to the large QDs is expected and, consequently, a delay for the buildup population in the large QDs is anticipated which can be observed as a longer rise time for the lower energy emissions. On the other hand, a strong saturation is expected for a high excitation density and in this case, the interdot transition cannot occur because the states are all occupied in large QDs. Consequently, the longer rise time is not expected.

According to the AFM results, the density of QDs of the studied samples in this work is higher than 10^{10} cm^{-2} and, therefore, a dense array of QDs with a multimodal and broad size distribution can be assumed. Therefore, the previous model may be applied to our system. Fig. 6.17a presents the PL intensity rise with respect to the time for the 3.6 ML sample at 75 K. The transient can be fitted by an

exponential function with a single time constant. The rise time was measured about 45±10 ps. The measured rise time does not change with respect to the energy (Fig. 6.17b). Therefore, the expected variation of the rise time for different energies, due to the delay for the buildup population in the large QDs, does not occur for this system. In fact, the TR–PL measurements in our case were carried out under the

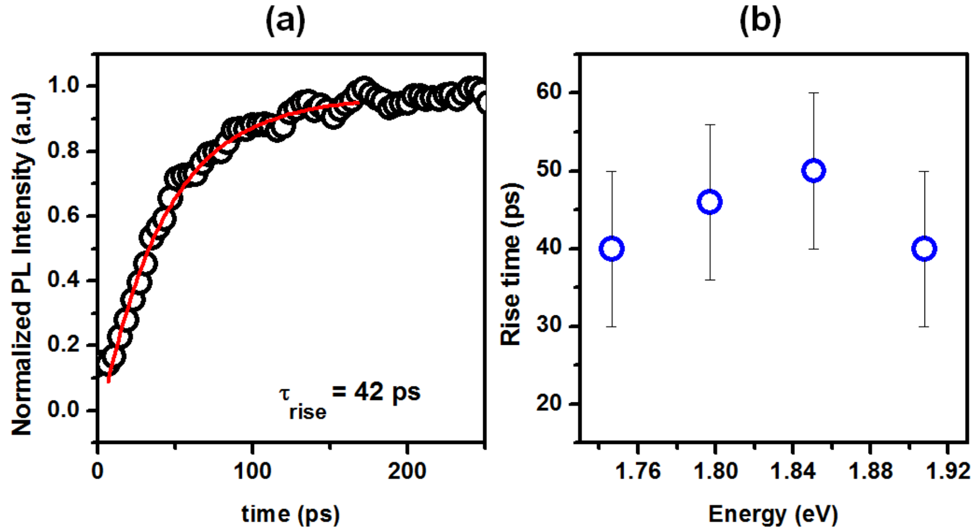

Figure 6.17: (a) PL intensity rise spectra of the 3.6 ML sample at 75 K. The red line curve is the exponentially fitted curve. The rise time of 42 ps was measured. (b) The rise time with respect to energy for 3.6 ML sample.

maximum excitation density. Hence, the results of our TR–PL measurements can be related to the strong saturation limit. Indeed, for a weak saturation limit, the second channel for the relaxation of the charge carriers (interdot transfer) leads to the faster relaxation of charge carriers and, therefore, a shorter decay time for higher PL energy is expected. Based on the measured rise time with respect to the energy (Fig. 6.17b), it is suggested that our system is far from the weak saturation limit ($\delta \rightarrow 0$). Therefore, the second and third terms in equation 6.3 are negligible and interdot transfer cannot occur from the energy states of the small to the states of the large QDs. Consequently, the charge carriers density in i_{th} dots distribution varies exponentially with the time and the measured decay time for GaAs QDs system is related to the recombination in the energy levels of i_{th} dots distribution. The TR–PL results demonstrate the decrease of the decay time with increasing the energy (Fig.

6.16b), thus, the larger the QDs, the shorter the decay time. This offers the stronger overlap between the electron and hole wavefunctions in the larger QDs which can be attributed to the expected direct type–I transition in the large QDs.

According to the temperature dependent measurements, the intensity of output light decreases with increasing the temperature. This may be related to the higher rate of the non–radiative recombination at higher temperatures due to the thermal escaping of the charge carriers. The results of the temperature dependent TR–PL measurements indicate the reduction of decay time with increasing the temperature. Fig. 6.18 shows the results of the decay time with respect to the temperature for the sample with GaAs nominal thickness of 3.6 ML. The corresponding decay time of peak–A reduces from 6.5 ns to 3.0 ns. For peak–B the decay time decreases from 3.0 ns to about 900 ps. A similar tendency has been seen for 1.8 ML and 2.7 ML samples. Therefore, the shorter decay time at higher temperatures may be associated with the significant rise of the non–radiative recombination rate and the fast mechanism of the non–radiative recombination can result to the reduction of the decay time [164].

To interpret the experimental results the following model is suggested [165]. The structural investigations, AFM and TEM, demonstrate that the QW (1.2 ML sample and WL) and the small QDs (less than 1 nm height) are fully strained. Therefore, the conduction band minimum of GaAs shifts 356 meV upward due to the strain. Consequently, the electrons at the Γ–valley of GaAs are located significantly higher than the electrons of X–valley in the GaP. The heavy holes, however, are fully confined in the valence band of GaAs. In this situation, the expected optical transition is indirect and occurs between the electrons localized at the X–state of GaP and the hh in Γ–valley of GaAs.

The growth of the thicker GaAs layer leads to the formation of larger QDs. This, in turn, may cause the reduction of the strain degree that refers to the partial relaxation of GaAs QDs. Depending on the relaxation degree, the state of the Γ–like electrons in GaAs shifts to the lower energy. On the other hand, due to the confinement effect, the energy states of QDs are pushed done for the larger QDs. The downward shift of the energy states of Γ–like electrons due to the relaxation

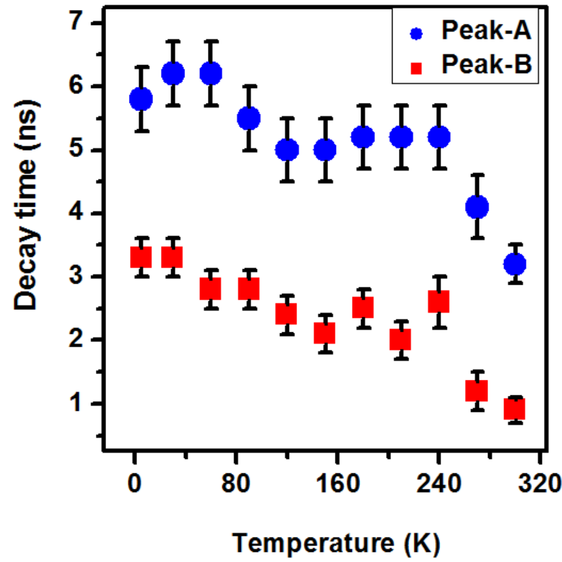

Figure 6.18: Decay time with respect to the temperature for the 3.6 ML GaAs sample. Blue circles correspond to the decay time of the peak–A and red squares represent the decay time of the peak–B.

together with the confinement effect lead to the localization of Γ state in GaAs at lower energy compared to the X–valley in the GaP matrix. Consequently, this represents the direct electron–hole transition in both **k** and real space. Fig.6.19a shows schematically the band alignment of the two extreme situations of a fully strained (type–II and indirect) and a fully relaxed (type– I and relaxed) GaAs/GaP heterostructure. The two arrows denote the expected e–hh transition for both cases. From the AFM analysis, It is known that for nominal thickness above 1.8 ML a multimodal size distribution fits better to the investigated QDs. Therefore, QDs can be divided depending on their height into the small, intermediate, and large QDs. An equivalent arrangement may be applied to the lateral size distribution. The small QDs are strained with an indirect e–hh transition, whereas the large QDs are relaxed with a direct e–hh transition. The electrons localized in the QDs with intermediate size are expected to have a mixed $\Gamma - X$ nature [154]. It is assumed that all of the QDs contribute to the optical emission and they are the origin of peak–A and –B in Fig. 6.11 for the nominal thickness above 1.8 ML. The peak–A is due to the smaller QDs and the B due to the larger QDs.

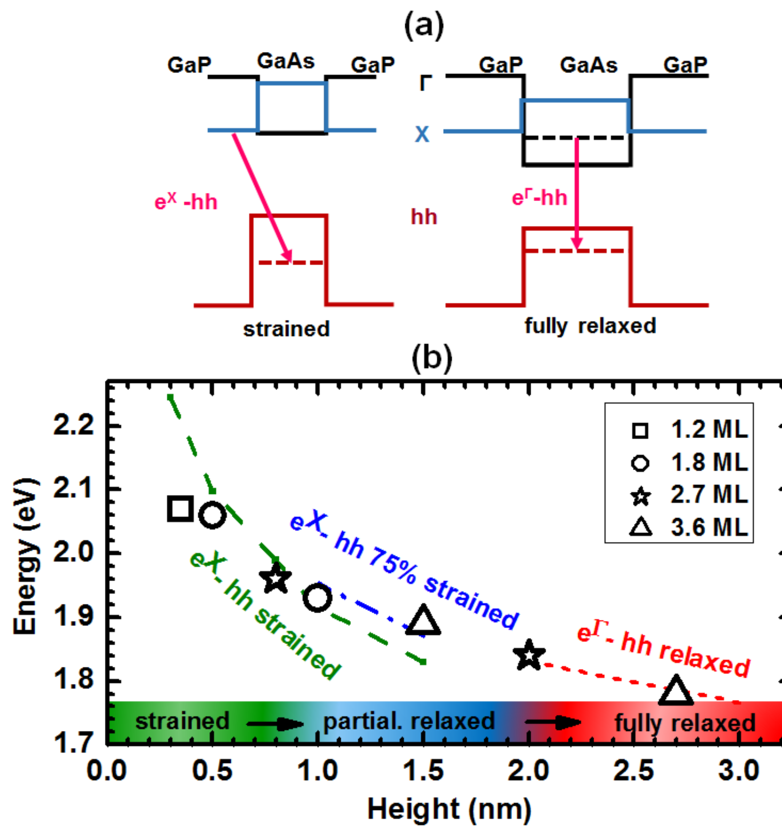

Figure 6.19: (a) Scheme of band alignment for a fully strained (type–II and indirect) and a fully relaxed (type –I and relaxed) GaAs/GaP heterostructure. The two arrows present the favorable e–hh transition. (b) The calculated energetically lowest e–hh transition for fully strained, 75% strained, and fully relaxed QDs as a function of the height. The symbols show the luminescence peak positions of four samples. The height for every peak position was taken from AFM analysis and gives the average height of small and large dots for the QDs samples, and the thickness of the QW in 1.2 ML sample.

The experimental behavior of the luminescence intensity for the samples with different GaAs thickness and the ratio between peak–A and –B support the model. The increasing of the total integrated intensity may be connected to a transition from a fully strained indirect type–II QDs system (1.8 ML sample) to a relaxed system with direct type–I QDs (3.6 ML sample). The large QDs for 2.7 ML and 3.6 ML samples are suggested to be relaxed and, therefore, have higher intensity due to the stronger overlap between electrons and holes wavefunctions in the type–I

band alignment. The fact that both 2.7 ML and 3.6 ML samples emit light up to room temperature and their faster decay time for peak–B can be attributed to the direct and type–I character of large QDs in those samples. Peak–A for the small QDs with a slower decay time and faster thermal quenching behave like a type–II system. The larger QDs have light emission at lower energy mainly due to the confinement effect. The connection between the increasing of size and the red shift in emission energy with the corresponding band alignment explain the decay time behavior presented in Fig. 6.16 b. The probability to have a mixed direct and indirect transition, and finally a direct and type–I QD increases with increasing the size of the QDs. The faster decay time of the larger dots can be explained by the stronger overlap between the electron–hole wavefunctions in a system with a direct type–I nature. The fastest measured decay time of about 2 ns is still higher than the reported values for the pure type–I systems, but it may be attributed to the mixed direct–indirect nature of the optical transitions.

The excitation density PL measurements in the range of 0.001 to 10 W/cm^2 verifies this picture and shows a remarkable 40 meV blueshift for peak A and a slight blueshift of about 6 meV for peak B for 3.6 ML sample (Fig. 6.15). The strong blueshift has already been reported for several type–II QDs [158, 159].

Generally, at the interface of two semiconductors, with their conduction band minima at two different valleys, the formation of localized interface states are expected. Particularly for a common anion heterointerface, these states may have mixed Γ–X character that participate to the optical transition [154]. However, in the case of GaAs/GaP with a common cation heterointerface, it was predicted by atomic empirical pseudopotential calculations that the interface states are not localized in the gap and are not optically active [154]. The appearance of peak–A and –B in luminescence spectra shows that both kinds of transition occur simultaneously in a mixed ensemble of type–I and type–II QDs.

In order to corroborate our model, the energy states of GaAs/GaP QWs and QDs were calculated for different relaxation degree [79]. The QDs were modeled as QW with a thickness same as the height of the QDs because the height of the QDs is at least one order of magnitude smaller than their lateral size. According to the cal-

culation, only for QDs with the height larger than 2 nm and fully relaxed, a direct e–hh transition in GaAs QDs is favorable. Fig. 6.19b shows the calculated energetically lowest and favorable e–hh transition for fully strained, 75% strained, and fully relaxed QDs as a function of the height. The symbols show the peak positions of samples with the nominal thickness of GaAs between 1.2 ML to 3.6 ML. The corresponding height for every peak position was taken from AFM analysis and gives the average height of small and large QDs in every sample. The luminescence peak positions fit well to the calculated results.

These results support our model for a transition from optically low–efficient indirect type–II strained QW and QDs to optically efficient direct type–I relaxed QDs while the size of dots increases. The strain relaxation in the GaAs/GaP QDs occurs via the formation of edge dislocations, which do not act as the non–radiative center and hence, allows the realization of e–hh transition [152, 166]. Similar characteristics have been also reported for the QDs based on the direct InGaAs embedded in the indirect GaP matrix [167].

Several Stranski–Krastanow QDs systems such as (In,Ga)As/GaAs and InAs/InP show luminescence spectra with two peaks, which are attributed to the QDs and to the wetting layer. However, the emission energy of the GaAs/GaP QDs is very low for the strained wetting layer with an estimated thickness of 0.4 ± 0.05 nm. Therefore, it is suggested that the origin of the light emission is the carrier recombination in the QDs. Only for 1.8 ML sample, the origin of peak–A might be the fully strained wetting layer.

6.2.3 Influence of growth temperature on GaAs QDs

Several samples were grown to investigate the influence of the growth temperature (T_G) on the characteristic features of GaAs QDs. To grow the samples, after oxide desorption of the 400 μm un–doped GaP (001) substrates, 500 nm GaP undoped buffer layer was grown at 520°C under 2.7 sccm PH_3. Afterward, growth was interrupted under the PH_3 flux to achieve the desired T_G in the range of 450–530 ^{o}C. Then, a 2.7 ML thick GaAs layer was grown under 2.5 sccm AsH_3 flux. After the growth of GaAs layer, growth was interrupted using 2.5 sccm AsH_3 to achieve

520 ^oC as T_G and finally the 50 nm GaP cap layer was grown. Fig. 6.20 shows the morphology of the GaAs quantum structures measured using AFM (measurements were carried out in IKZ). The results indicate that the morphology of the QDs changes with increasing T_G. The formation of almost round shape GaAs QDs is observed when T_G is 450 ^oC while the morphology of QDs changes to the elongated QDs (QD dashes) for T_G = 500 ^oC. With increasing T_G up to 530 ^oC, elongated QDs with larger average length are formed. Tab. 6.3 summarizes the results of AFM measurements analysis. The average height of QDs increases from 1.4 nm in the case of T_G = 450 ^oC to 2.9 nm for T_G = 530 ^oC. The results indicate also that the width of QDs in the [110] direction does not vary significantly and it is about 20±1 nm for different growth temperatures. The average length of QDs along the $[1\bar{1}0]$ direction, on the other hand, elongates for the higher T_G than 450 ^oC. The average length is 20 nm for the grown sample at 450 ^oC, while it rises up to 58 nm for the grown sample at 530 ^oC. The density of QDs reduces with increasing the temperature from 7.6×10^{10} cm^{-2} to 3.6×10^{10} cm^{-2} for 450 ^oC and 530^oC, respectively. The estimated thickness of WL using the AFM results demonstrates a thinner WL with increasing T_G. The WL thickness varies between 0.4±0.05 nm to 0.1±0.05 nm for 450 ^oC, and 530 ^oC, respectively. The reduction of the WL thickness and density with increasing the growth temperature can be related to the formation of the larger elongated QDs for the equivalent nominal thickness of GaAs (2.7 ML).

Table 6.3: Results of the AFM measurements analysis. The growth conditions were same for all samples except the applied T_G for the growth of the 2.7 ML GaAs layer.

T_G (^{o}C)	**Height (nm)**	**Width [110] (nm)**	**Length $[1\bar{1}0]$ (nm)**	**density $\times 10^{10}$ (cm^{-2})**	**WL (nm)**
450	1.4	20	20	7.6	0.4
500	1.8	21.1	48	4.8	0.21
530	2.9	21.1	58	3.6	0.15

Fig. 6.21 shows the size distribution of the height, width, and length of the GaAs QDs that were grown at T_G in the range of 500–530 ^oC. Accordingly, a

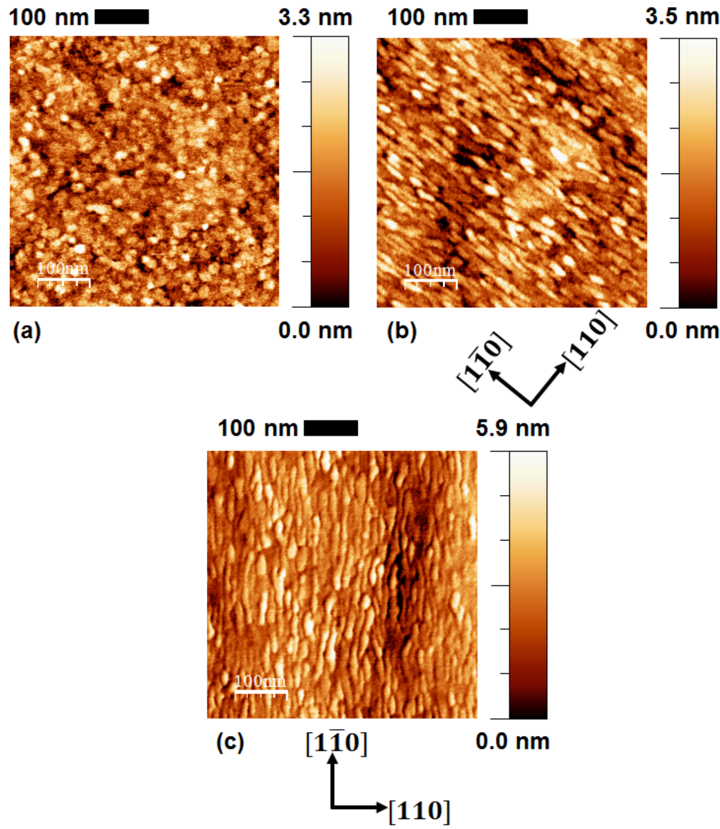

Figure 6.20: Results of AFM measurements of grown samples at different T_G with the identical nominal thickness of 2.7 ML GaAs, (a) T_G = 450 ^{o}C, (b) T_G = 500 ^{o}C, and (c) T_G = 530 ^{o}C. The elongation direction is shown for the grown samples at T_G = 500, and 530 ^{o}C.

multimodal size distribution corresponds better than a Gaussian distribution for the height, width, and length [155].

The shape transition of QDs can be explained using a model for the long rectangular islands. In this model, an island is considered with height (h), width (w), length (l), and facet angle (θ). It is also assumed that the relaxation of islands occurs along the growth direction (z) [168, 151]. Fig. 6.22 shows the scheme of the considered island. The island energy, therefore, can be written as [168]:

$$E = E_{surface-interface} + E_{relax} \tag{6.7}$$

Here, $E_{surface-interface}$ defines the surface and interface energy, while E_{relax} denotes the variation of energy due to the elastic relaxation. The surface energy can be written as a function of tension. If γ_i defines the island–substrate interface tension

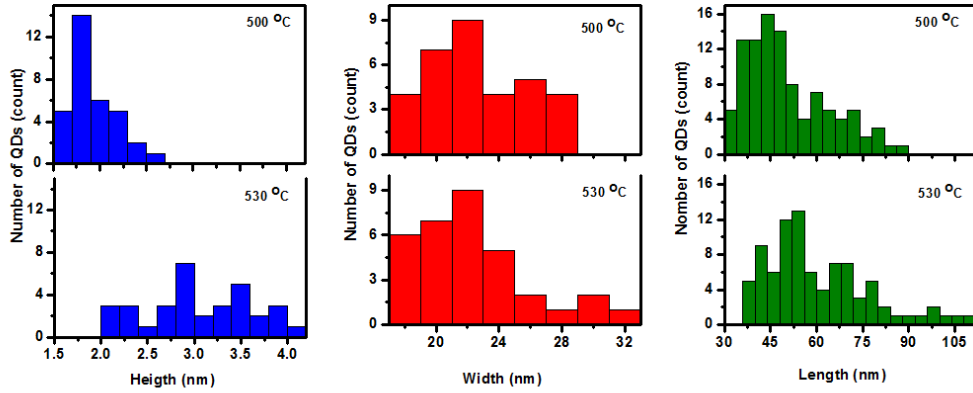

Figure 6.21: The size distribution of the height, width, and length of the GaAs QDs grown at different T_G.

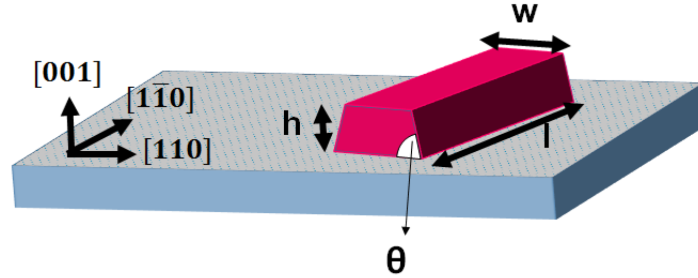

Figure 6.22: Scheme of an elongated QD along the [1$\bar{1}$0] direction. The height, width, length, and the facet angle are denoted with h, w, l, and θ, respectively.

and, γ_l, γ_w, and γ_h denote the length, width, and height tension of the island per unit area, then, $E_{surface-interface}$ can be written as [168]:

$$E_{surface-interface} = wl(\gamma_i + \gamma_l - \gamma_w) + 2(w+l)[h\gamma_h csc\theta - hcot\theta(\gamma_l + \gamma_w - \gamma_i)/2] \quad (6.8)$$

Since the growth is done in the SK mode, the GaAs WL is considered as the proper reference instead of the substrate. Consequently, γ_i may considered equal to zero. Equation 6.8, therefore, reduces to [168]:

$$E_{surface-interface} = wl(\gamma_l - \gamma_w) + 2(w+l)[h\gamma_h csc\theta - hcot\theta(\gamma_l + \gamma_w)/2] \quad (6.9)$$

γ_l and γ_w are considered equivalent in the rectangular island model, however, I suggest that the difference between γ_l and γ_w may be the reason for the formation of elongated QDs. The increase of the growth temperature may cause the reduction of

tension along [1$\bar{1}$0], γ_l (dimmer axis of group–V–terminated elements), compared to [110], γ_w, for Ga ad–atoms. This leads to the higher mobility and the increase of the diffusion length of Ga ad–atoms along the [1$\bar{1}$0] direction [116] with increasing the growth temperature. The different diffusion lengths for ad–atoms along these two directions can cause a preferred direction for ad–atoms and, therefore, it can be suggested as the origin of the elongation of the GaAs QDs in this direction.

The optical properties of the samples were investigated using a PL system in Paul Drude Institute in Berlin with the assistance of Dr. P. Corfdir. The measurements were carried out using an excitation wavelength of 325 nm and in a He–cryostat in the range of 10–300 K. Fig. 6.23 shows the PL spectrum of the samples at 10 K.

The results indicate the optical transitions in the range of 2.1 eV to 1.75 eV. Each sample has a broad spectrum at 10 K that can be related to the broad size distribution of the QDs and elongated QDs (Fig.6.21). The elongated QDs may be divided into two classes of the small and large elongated QDs and, therefore, the broad spectrum can be fitted using two Gaussian peaks. The peak–A at higher energy is related to the small QDs and located at 1.98, 1.89, and 1.86 eV for T_G equal to 450, 500, and 530 ^{o}C, respectively. The peak at lower energy, peak–B, is associated to the large QDs and located at 1.89 eV for T_G = 450 ^{o}C, 1.81 eV for T_G = 500 ^{o}C, and 1.78 eV T_G = 530 ^{o}C (Tab. 6.4). The redshift of spectra is observed with increasing the T_G. This redshift is related to the quantum confinement effect and the formation of larger QDs at higher T_G that is confirmed by the AFM results [169]. The luminescence intensity is similar for the different growth temperatures.

Temperature–dependent measurements of the samples including the elongated QDs demonstrate the redshift of the peak positions, peak–A and peak–B (Fig. 6.24a). This redshift is consistent with the shift of E_g of GaAs and GaP toward the lower energy based on the Varshni model [65]. The thermal quenching of the luminescence is observed for both peaks (Fig. 6.24b). The activation energies for peak–A and peak–B was determined using the integrated intensity with respect to the temperature and equation 6.1. The obtained value for E_1, and E_2 of Peak–A and peak–B for the samples grown at different T_G are summarized in Tab.6.5. The

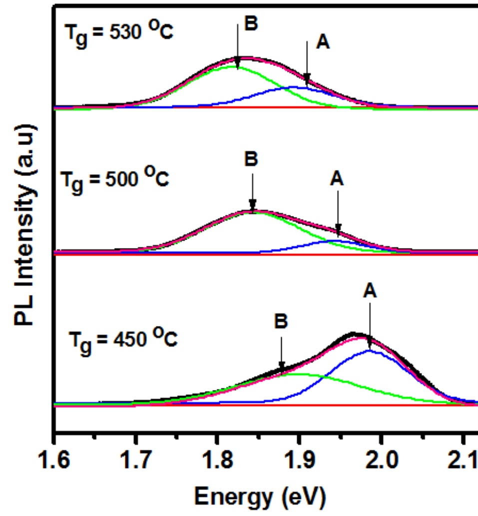

Figure 6.23: PL results of the samples with the identical nominal thickness of 2.7 ML GaAs that was grown at T_G in the range of 450–530 ^{o}C. PL measurements were carried out in a He–cryostat at 10 K using an excitation wavelength of 325 nm. The spectrum of each sample was fitted by two Gaussian peaks. The position of peak–A and peak–B is shown by the arrows.

Table 6.4: The peak position of the optical transition of three different samples at 10 K. The spectrum of each sample were fitted by two Gaussian peaks. The samples have identical nominal thickness of 2.7 ML but they were grown at three different T_G.

T_G (^{o}C)	Peak–A (eV)	Peak–B (eV)
450	1.98	1.89
500	1.89	1.81
530	1.86	1.78

first activation energy of both peaks of the samples including the elongated QDs are small with a weak c_1. The small c_1 refers to the low efficiency of the carrier thermal escape. Therefore, it leads to the slow thermal quenching of the output luminescence at temperatures below 120 K. The strong E_2 has a large influence in the thermal quenching of the intensity due to the large c_2. The results indicate, however, that both E_1, and E_2 are larger for the grown samples at higher T_G. The largest activation energy of about 234 meV belong to the sample grown at 530 ^{o}C. The increase

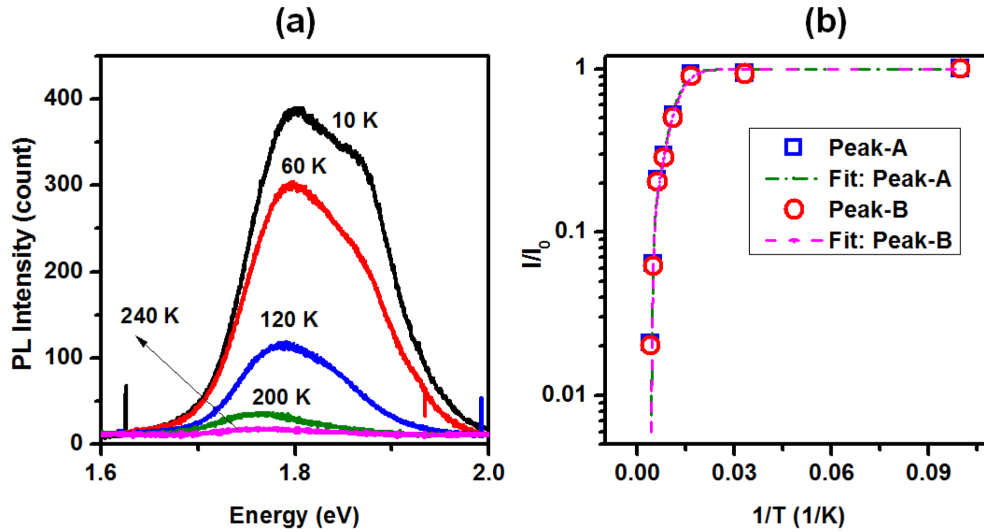

Figure 6.24: (a) Temperature dependence measurements of the grown sample at 530 ^{o}C, (b) The Arrhenius plot of the intensity of both peaks versus temperature. The lines are the fitted curves.

of the activation energy leads to the lower rate of the thermal quenching. This, in turn, may be attributed to the enhancement of the charge carrier confinement for the grown sample at higher temperatures. From AFM results, it is known that the height and length of the QDs rise with increasing T_G. The sample grown at 530 ^{o}C has the largest average height of 2.9 nm and the average length of 58 nm. The increase of the size of the GaAs QDs leads to the increase of the relaxation degree. This can cause the downward shift of the conduction band edge of GaAs QDs at Γ–valley. Therefore, a type–I direct transition is expected for the large size elongated QDs and the increase of the activation energy can be related to the stronger confinement of electrons in a type–I system. This is confirmed by the calculations for the QW of GaAs with the thickness of 3 nm (Fig. 6.2b). Therefore, the two activation energies, E_1 and E_2, may be related to the activation energy for the thermal escape of electrons.

The excitation density dependent PL measurements were carried out at 10 K using the excitation density in the range of 1.3 Wcm^{-2} to 130 Wcm^{-2} (measurements were done in PDI with the assistance of Dr. P. Corfdir). Fig. 6.25a shows the PL spectra measured ate the different power density for the sample grown at 530 ^{o}C. The positions of peak–A and peak–B are shown with the arrows. The

Table 6.5: The obtained activation energies, E_1, and E_2, using the Arrhenius equation with respect to the intensity reduction of peak–A and peak–B of each sample with increasing the temperature [156, 157]. The corresponding escape efficiency, c_1, and c_2, are shown. The GaAs layer has identical nominal thickness of 2.7 ML but it was grown at different T_G in the range of 450–530 ^oC.

T_G (^{o}C)	Peak–A		Peak–B	
	E_1 (meV)	E_2 (meV)	E_1 (meV)	E_2 (meV)
450	6	—	6	83
500	10	125	16	131
530	30	251	38	253

T_G (^{o}C)	Peak–A		Peak–B	
	c_1	c_2	c_1	c_2
450	52.4	—	1.9	696.3
500	6.6	1.9×10^4	19.5	1.3×10^4
530	43.7	1.1×10^7	38.2	1.4×10^7

shape of the PL spectrum does not change with increasing the excitation density. The peak positions, however, shift toward higher energy at higher excitation density (Fig. 6.25b). The small blueshift of about 8 meV of the both peak–A and peak–B is close to the 6 meV blueshift of the peak–B for the 3.6 ML sample grown at 450 ^{o}C. Consequently, the formation of the larger QDs leads to the smaller blue shift with increasing the excitation density. The significant blueshift in type–II QW is a well–known behavior that is attributed to the formation of a triangular potential at the interface of the conduction band (in or case conduction band). It was also shown that in the QDs system, the blue shift can be related to the occupation of the higher energy states for instance in small QDs [158]. The shifts toward higher energy with increasing the excitation density in our system including QDs with large size distribution, therefore, may be attributed to the occupation of the higher energy states in small QDs.

The formation of elongated QDs along the $[1\bar{1}0]$ may cause the polarization dependence of the intensity of the radiative transitions along [110] and $[1\bar{1}0]$ direc-

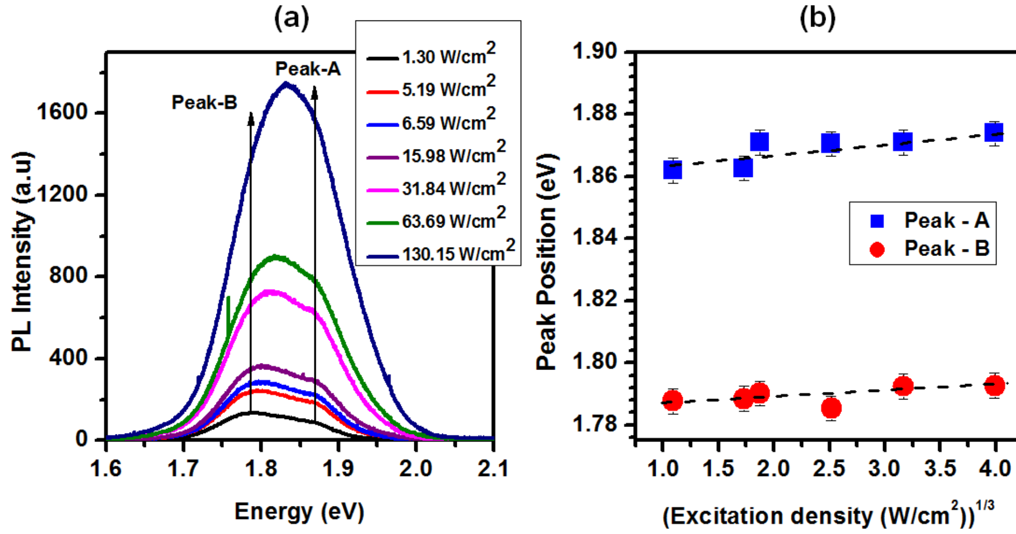

Figure 6.25: (a) PL spectra of the sample grown at 530 ^{o}C for different excitation density. (b) The peak position as a function of the excitation density to the power of 1/3. The blue circles represent the peak–A and peak–B is demonstrated with red squares. Measurements were carried out at 10 K.

tions. To study the influence of the elongation of QDs, the polarization dependent PL measurements were carried out at 10 K and the output light was polarized in the range of 0–360° (measurements were done in PDI with the assistance of Dr. P. Corfdir). Fig. 6.26 depicts the results of the polarization PL measurements for the grown samples at 450 ^{o}C, and 530 ^{o}C.

Fig. 6.26a and b present the integrated intensity of peak–A and peak–B for 450 ^{o}C, and 530 ^{o}C, respectively. According to the results, the integrated intensity of radiative transition is larger in $[1\bar{1}0]$ compared to [110] for both samples. The results, however, indicate that the ratio of the integrated intensity along $[1\bar{1}0]$ to [110] for both peak–A and peak–B is larger for the elongated GaAs QDs. The total intensity polarization of PL spectra was calculated using:

$$P = \frac{I_{[1\bar{1}0]} - I_{[110]}}{I_{[1\bar{1}0]} + I_{[110]}} \tag{6.10}$$

Fig. 6.26c and d show the total intensity polarization of radiative transition with respect to the energy for T_G = 450 and 530 ^{o}C, respectively. The results demonstrate that the PL spectrum of the sample– T_G = 530 ^{o}C is about 50% polarized in the energy range of 1.7 eV to 1.9 eV, while the polarization is less than about 10%

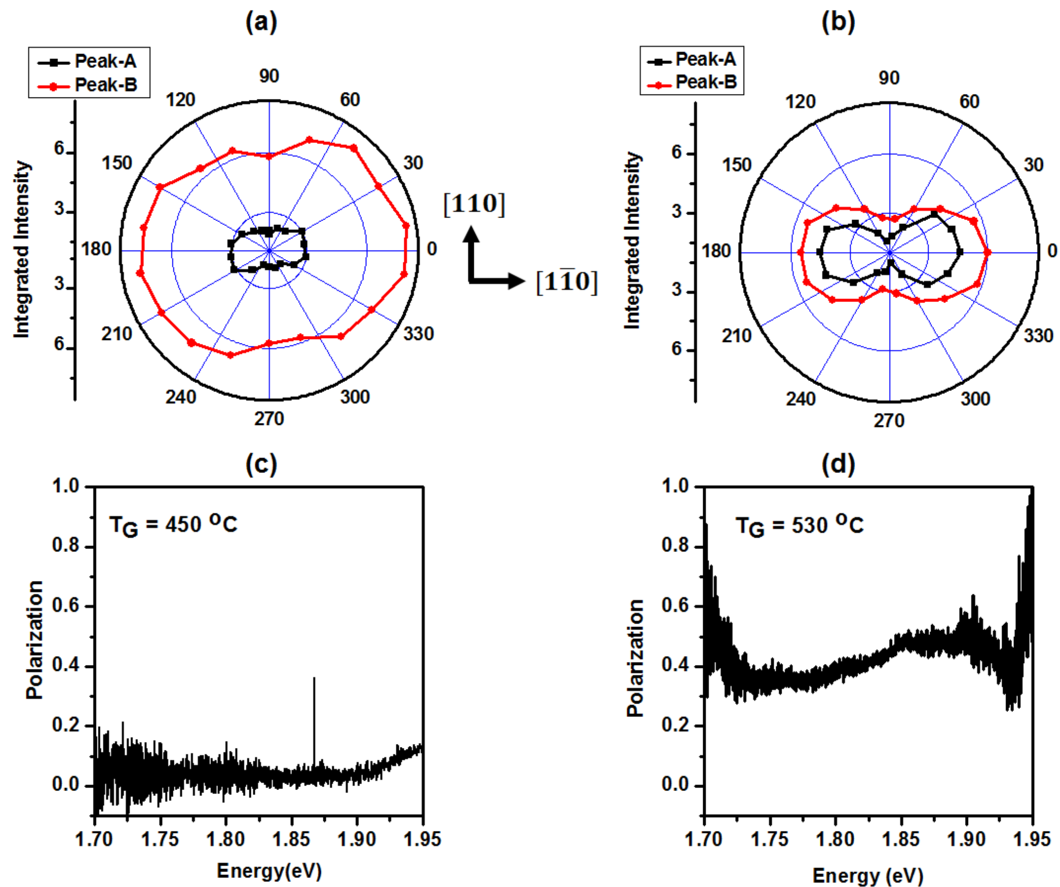

Figure 6.26: Results of polarization dependence PL measurements that were carried out at 10 K in the range of 0–360° polarization angle. (a), (b) the integrated intensity of peak–A and –B with respect to detection angle along the [110] direction for the grown samples at 450 and 530 ^{o}C, respectively. (c) and (d) the total PL polarization with respect to energy for the grown samples at 450 and 530 ^{o}C.

for the sample– T_G = 450 ^{o}C. Consequently, the elongation of GaAs QDs in [1$\bar{1}$0] direction may lead to the higher probability of radiative recombination in this direction. This, in turn, leads to the higher intensity of radiative recombination in [1$\bar{1}$0] direction. Therefore, elongation of QDs leads to the increase of the luminescence along [1$\bar{1}$0] and a polarized emission spectrum can be suggested for the samples consisting the elongated QDs.

The following model may explain the experimental results: The structural characterizations (AFM) show the increase of the QDs size with increasing T_G. The size distribution analysis offer also a broad and multimodal size distribution. The

results corroborate the reduction of the WL thickness down to 0.1 nm and indicate the elongation of the QDs in the $[1\overline{1}0]$ direction with increasing the growth temperature. The increase of the growth temperature leads to the higher mobility and, therefore, the increase of the diffusion length of Ga ad–atoms in the $[1\overline{1}0]$ direction. This, in turn, may lead to a favorable direction for the Ga ad–atoms that can cause the elongation of GaAs QDs. Formation of large QDs increases the relaxation degree via the increase of the density of dislocations. The dislocation may be sorted in screw dislocations, which form perpendicular to the growth direction, mixed dislocations that are in the growth and elongation directions, and the edge dislocations that form in the growth direction [170]. Several investigations indicated that the edge dislocations do not act as the non–radiative centers [152, 166]. The screw and mixed dislocations, on the other hand, participate in the recombination as the non–radiative centers [166].

According to the calculations, the increase of the relaxation degree of QDs can shift the conduction band edge of GaAs QDs at Γ–valley to the lower energy than the X–valley of GaP. The energy states of the electron for larger QDs shift downward due to the quantum confinement effect. A transition from an indirect type–II to a direct type–I system, therefore, is expected with increasing the relaxation degree and formation of larger QDs.

The PL spectra show a redshift with increasing the growth temperature, which corresponds to the formation of the larger elongated QDs at higher temperatures. The analysis of temperature–dependent PL measurements demonstrate the larger activation energies for the grown samples at the higher temperatures. For instance, the activation energy for the sample grown at T_G = 530 ^{o}C is about 234 meV. Therefore, a lower thermal quenching rate of the luminescence is anticipated for the sample including the larger elongated QDs. The excitation density dependent PL measurements in the range of 1.3 to 310 W/cm^2 illustrate a blueshift of about 8 meV for both peak–A and peak–B for the grown structure at T_G = 530 ^{o}C (Fig. 6.24b) that can be attributed to the participation of the high energy states, for instance, in small elongated QDs [158]. The broad size distribution of elongated QDs may support this picture. The polarization dependent PL measurements indicate a

larger polarization for the output intensity of the elongated QDs compared to the QDs (Fig. 6.26). In fact, a different electronic structure is offered for the elongated QDs (QDash) [171, 69]. The nature of the density of states of the elongated QDs (QDash) is not well known and it is supposed that they have behavior between QDs and QWires [172, 173, 171]. It is suggested that the transient of the charge carries along the elongation direction is easier for elongated QDs or QDashes, whereas this transient is more complicated for the QDs due to the three–dimensional confinement [174]. Therefore, the higher polarization of the output intensity along the $[1\bar{1}0]$ direction for the elongated QDs can be related to their QWire nature.

On the other hand, it is expected that the total luminescence intensity increases with the transition from a mixed type–II and type–I system for the grown sample at 450 ^{o}C to the expected type–I system for the samples including the elongated QDs. Indeed, a stronger overlap between the wavefunction of electrons and holes is anticipated in a type–I system, in which the electron and holes are in the same real–space and k–space. The total intensity of the emitted light, however, is similar for the samples including the elongated QDs and the grown sample at 450 ^{o}C including QDs. The increase of the relaxation degree for the large elongated QDs is expected to result via the formation of the dislocation defects. The larger density of screw and mixed dislocations for elongated QDs, therefore, is anticipated for elongated QDs. The higher density of mixed and screw dislocation, which act as the non–radiative centers, may be proposed as the origin of the higher probability for the non–radiative recombination in the elongated QDs (QDash) compared to QDs. Therefore, the larger probability of non–radiative recombination in the large and relaxed elongated QDs can lead to the comparable output intensity of the elongated QDs with expected direct type–I transition and the QDs with a mixed type–I and type–II nature.

6.3 LEDs based on GaAs QDs embedded in GaP

6.3.1 LEDs based on the III–V semiconductors

III–V semiconductors are one of the interesting materials for the LEDs production. GaP can be a good candidate for the LEDs production at the visible wave-

lengths because it is a transparent material for this region due its large bandgap energy. This leads to the easier extraction of the emitted light in the most part of the visible range and, therefore, a higher extraction efficiency is expected. To fabricate the operational LEDs based on the indirect GaP, the disadvantage of the different crystal momentum of electrons and holes must be overcome. The useful light emitters can be fabricated by doping the indirect GaP with impurities such as nitrogen (N) that have a significant attractive short–range potential [175, 176]. The spatial localization of electrons in impurities leads to a delocalization in momentum space. This increases the probability for the electrons to have equivalent crystal momentum of the holes. The emission wavelength of the GaP:N LEDs vary in the range of yellow to green light depending on the N concentration. The external quantum efficiency of these type of LEDs, however, is not higher than 0.3% [177].

Design, growth and fabrication of the quantum structures on III–V semiconductors can be a promising idea. An important commercial type of LEDs is based on the $(Al_xGa_{(1-x)})_yIn_{(1-y)}P$ lattice matched to GaAs. The LEDs based on this material system emit from yellow to red wavelengths. The largest direct bandgap for this material system is at about 550 nm, whereas for Al content of more than 53% the system transforms to an indirect material system. This material system is incapable for the high–efficiency green emission [177]. The highest reported external quantum efficiency for 558–577 nm AlGaInP LEDs is lower than 2% [192]. The complicated epitaxial process in addition to the several required fabrication steps are the further disadvantages of this material system [177, 178].

Using the large and direct bandgap material on a relaxed buffer on GaAs substrate is an alternative idea. Masselink et. al reported the fabrication of the LEDs based on InGaP and (Al,Ga)InP grown on the relaxed buffers on GaAs substrates. The reported wavelength is around 550 nm [179]. Fitzgerald et al. used a similar idea to fabricate the LEDs on GaP substrates [180]. However, the threading dislocations in both case are the disadvantage of the structures.

The emission of GaN can be varied from violet to green with adding In to the system and decreasing the bandgap energy. In clusters, however, can form due to the thermodynamic instability of InGaN that results in spatial non–uniformity of In

atoms. These In–clusters limit the realization of green LEDs based on InGaN/GaN QWs. The high forward voltage threshold of InGaN LED is the further disadvantage of this system [181, 182, 183, 184, 185].

The LEDs based on InP/GaP system emit light at 550 nm to 720 nm [186, 187, 189]. The active region of the diode consists of the stacked self–assembled InP QDs grown in SK mode accompanied by the WL and embedded in a GaP matrix. The green emission appears to originate from the wetting layer. The complicated band structure of the InP/GaP system is the difficulty of this system.

Recently, fabrication of LEDs based on the self–assembled InGaAs QDs embedded in GaP matrix has been reported. The shortest reported wavelength is at about 1.86 eV (667 nm) [143]. The segregation of In atoms and difficulties to grow the (In,Ga)As QDs on GaP substrates are the disadvantages of this system [136, 138].

In the previous section, I described the growth and characterization of the GaAs QDs embedded in the GaP matrix. The broad emission spectra were observed in the range of 1.7 eV to 2.1 eV for the GaAs/GaP heterointerface. Therefore, this material system might be a good candidate for the LED production. In this section, I will bring up the EL results of fabricated LEDs based on the GaAs/GaP system [129].

6.3.2 Growth and processing

Samples were grown using the Riber–32P GSMBE on a Sulfur (S)–doped GaP (001) substrate. After desorption of native oxides of the substrate, a GaP: Si buffer layer with the thickness in the range of 300 to 700 nm was grown. The Si concentration was about 10^{18} cm^{-3}. Afterward, the intrinsic region consisting of 5 (or 1) periods of 1.2 ML or 3.6 ML of the undoped GaAs layer were grown. Each GaAs layer was covered by 11 nm undoped GaP spacer layer. Finally, the structures were capped by a thick (300 to 700 nm) GaP:Be layer with Be concentration about 10^{18} cm^{-3}. Fig. 6.27 shows the scheme of the grown structures. A p–n junction of GaP: Si–GaP: Be was grown with equivalent doping concentration for Si and Be as the reference sample.

The grown structures then were processed for EL measurements. Fig.6.28 shows

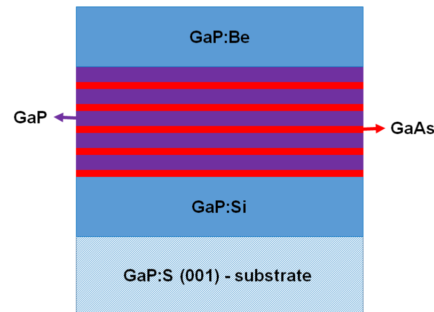

Figure 6.27: Scheme of the grown p–i–n junction of GaP: Be–GaAs–GaP: Si. Each structure consists of 300 to 700 nm GaP: Si buffer and GaP: Be cap layer. Active region consists of 1 or 5 periods of 1.2 ML or 3.6 ML GaAs/ 11 nm GaP.

the scheme of the desired isolated–mesa, where the p–doped GaP layer, the intrinsic region including the GaAs quantum structures, and the n–doped GaP layer are confined in a pillar with a circular cross–sectional area with the diameter of 300 μm. The final constructed mesa includes a 7.5 nm nickel (Ni)and 100 nm gold–germanium alloy (Au: Ge (88:12)) as the back contact and a cross shape front contact of 20±3 nm Chromium (Cr) and 230±3 nm Au. The samples, then, were mounted on the cheap carries and bonded using thin Gold wires. The description of the processing method can be found with details in the M.Sc. thesis of C. Golz [129].

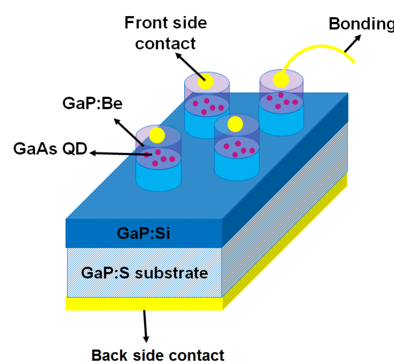

Figure 6.28: Scheme of the final mesa including the back side contact (7.5 nm Ni and 100 nm Au: Ge (88:12)), GaP:S substrate, GaP: Si buffer, GaAs quantum structure, GaP: Be cap, cross shape front side contact (20±3 nm Cr and 230±3 nm Au), and the bonding.

6.3.3 Optical results

Fabricated LEDs were mounted on the cold finger of a cryostat for EL measurements. The cryostat was cooled down to 80 K. Fig. 6.29 illustrates the results of EL measurements on two LEDs with 1.2 ML and 3.6 ML GaAs as the active region under a constant current density of 142 Acm^{-2}. The black curve corresponds to the EL spectrum of the sample with 3.6 ML GaAs while the blue curve indicates the results for 1.2 ML GaAs–LED. The EL spectrum of the reference p–n junction is shown with the red curve for comparison. The results indicate a broad spectrum with the FWHM of 290 meV for the EL spectrum of the reference sample. However, the peak shape and the peak position (at about 2.1 eV) of the reference sample differs from the EL spectra of the samples with GaAs quantum structures as the active region.

According to the EL spectra, the peak position shifts toward lower energy with increasing the nominal thickness of GaAs. It is known from AFM results that the formation of the GaAs QDs occurs for the nominal thicknesses above 1.2 ML (more information can be found in 6.2.2). Therefore, the emission line at 1.96 eV for the sample with 1.2 ML GaAs may be associated with the radiative recombination in a thin GaAs QW. Whereas, the emission line at 1.83 eV for the 3.6 ML GaAs sample may be related to the large QDs. 130 meV redshift of the emission line with increasing the nominal thickness of GaAs can be related to the quantum confinement effect due to the formation of large QDs. The optical properties of the stacked GaAs/GaP were investigated. For this purpose, one sample was grown with the intrinsic region of 5 periods of 3.6 ML undoped GaAs capped by 11 nm undoped GaP. The equivalent doping concentrations were used for Si and Be of the n– and p–GaP layer. An identical processing approach was applied to fabricate the LED structure. The EL measurements were carried out at 80 K using the same current density of 594 Acm^{-2} and the results are shown in Fig. 6.30. The results demonstrate a peak at the same position of the one period GaAs/GaP active region (red curve) for the 5 periods stacked of 3.6 ML GaAs (blue curve). The EL spectra imply a larger FWHM and shift of the tail of the spectra toward the lower energy range for the stacked structure. The origin of the redshift, may be attributed to (i) the coupling

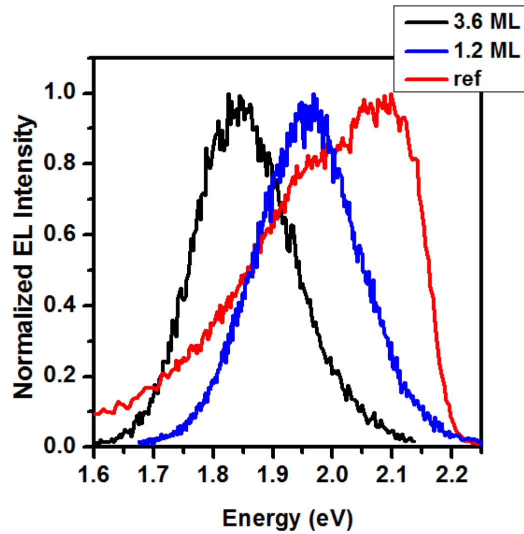

Figure 6.29: The EL spectra of p–i–n junction of GaP:Be–GaAs –GaP:Si. Blue curve represents the EL of 1.2 ML GaAs while the spectrum of the 3.6 ML GaAs sample is illustrated by the black curve. The EL spectrum of a GaP:Be–GaP:Si p–n junction is shown for comparison (red curve). The EL measurements of p–i–n junction were carried out under identical current density of 142 Acm^{-2}. The measurements were done at 80 K.

of the wavefunction of the QDs in the stacked structure [193], (ii) the formation of larger QDs in the upper layer [194], a larger inhomogeneous size distribution, or (iii) the strain relaxation in the upper layers [194]. The probability of the coupling between the individual QDs layers is low due to the thick GaP spacer layer (11 nm). Several investigations were done on the influence of the spacer thickness on the optical properties of stacked self–assembled structures. It was shown that for the thin spacer layers the strain relaxation results to a significant redshift [195]. Our results, however, imply an equivalent peak position but a broader FWHM for the spectrum of the stacked sample compared to one period GaAs/GaP active region. Therefore, it may be suggested that the broader FWHM results from a larger inhomogeneous size distribution in the stacked structure. According to AFM results, the size distribution of QDs for one layer of GaAs with the nominal thickness of 3.6 ML is broad and multimodal. Consequently, a similar tendency is expected for the stacked structure and presumably, a larger size distribution of QDs at upper layers can be the origin of the broader FWHM of the spectrum of the stacked structure.

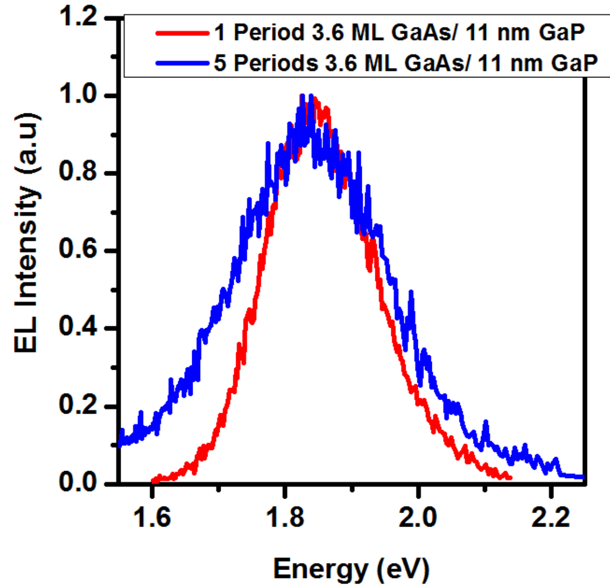

Figure 6.30: The EL results of p–i–n junction of GaP:Be– GaAs – GaP:Si with identical thickness of 3.6 ML GaAs. Blue curve represents the EL results of the sample consists of 5 periods of GaAs/GaP while the red curve indicates the results for one period GaAs/GaP sample. The EL measurements of p–i–n junction were carried out under identical current density of 594 Acm^{-2}. The measurements were done at 80 K and the EL intensity was normalized.

6.4 Summary

The formation of GaAs QDs on GaP substrate for nominal thickness larger than 1.2 ML was demonstrated. According to the AFM results, the size of QDs increases with increasing the grown nominal thickness of GaAs and a multimodal size distribution fits better to the analyses data. The influence of using different growth temperature was seen as the formation of the elongated QDs in the case of the temperatures higher than 450 ^{o}C. The elongation of QDs happens in $[1\bar{1}0]$ direction.

The optical emission of the GaAs/GaP QDs was demonstrated up to room temperature for 2.7 ML and 3.6 ML GaAs samples in the visible range. The broad luminescence spectra of the grown samples with nominal GaAs thicknesses above 1.2 ML can be fitted using two Gaussian peaks. The thin wells and small dots are fully strained and have type–II band alignment with the indirect e–hh transition. On

the other hand, it may be suggested that the increase of the size of the QDs is followed by the increasing of the relaxation degree. This, in turn, can push downward the conduction band edge of GaAs at Γ–valley and leads to the transformation of the band alignment of GaAs/GaP heterointerface from a type–II system to a type–I system and a direct e–hh transition. The theoretical calculations support the provided model.

I demonstrated the fabrication of the LEDs based on the GaAs quantum structures embedded in the GaP matrix. The optical results indicate the EL for both samples 1.2 ML and 3.6 ML GaAs. The corresponding EL spectra show a different peak shape and position compared to the grown GaP p–n junction as the reference. The 100 meV redshift of the EL peak for the GaAs QDs (3.6 ML) sample compared to 1.2 ML sample is related to the quantum confinement effect and the formation of large QDs that is consistent with the PL and CL results of the un–doped GaAs/GaP samples. The stacked structure emission shows a broader FWHM compared to the one period of 3.6 ML GaAs sample. The broader FWHM of the stacked structure can be attributed to the broader size distribution of QDs at upper layers.

Chapter 7

$Al_xGa_{1-x}As$ quantum structure in the GaP matrix

The production of the light emitter in the so–called "Green–GaP" wavelength range is an ongoing challenge [196]. The InGaN/GaN heterostructures are reported as the promising emitters for the energy range of 3.5 eV (blue wavelength range) [197]. On the other hand, the highest emission energy of the III–V semiconductor quantum structures in the GaP matrix is reported to be around 2.0 eV. InAs QDs, for instance, have the emission at 1.73 eV [124]. The highest emission energy of InP QDs is reported at about 2.0 eV [125]. $In_xGa_{1-x}As$ QDs/GaP system has the emission around 2.0 eV for x = 0.3 [138]. In the previous chapter, I reported the emission energy of 2.07 eV for a thin GaAs QW (1.2 ML) in the GaP matrix.

Among the III–V semiconductors, AlAs has the closest lattice constant with GaAs but larger E_g of 2.1 eV [198]. AlAs, however, is an indirect semiconductor with the minimum of the conduction band at X–valley. $Al_xGa_{1-x}As$, meanwhile, is a direct bandgap energy semiconductor for $x \leq 0.45$. Consequently, a higher direct E_g may be achieved for $Al_xGa_{1-x}As$/GaP for $x \leq 0.45$ compared to GaAs/GaP system.

In this chapter, the results of my attempts to shift E_g to higher energy range with designing the proper band structure of $Al_xGa_{1-x}As$/GaP system with respect to the content of Al will be discussed. The main goal was to design a light emitter close to the green gap. Section 7.1 concentrates on the results of the simulations and the theoretical model for the band alignment of the $Al_xGa_{1-x}As$/GaP heterostructure. I will explain the growth and characterization results in section 7.2, and finally the results will be summarized in section 7.3.

7.1 Electronic structure of $Al_xGa_{1-x}As$/GaP

The lattice constant of AlAs, a_{AlAs}, is reported to be in the range of 5.660–5.662 Å [199, 200]. Consequently, the lattice mismatch of AlAs and GaAs is about 0.12%. Therefore, the lattice mismatch of the $Al_xGa_{1-x}As$ and GaP is in the range of 3.7–3.77%, when x varies between 0.0 to 0.5.

The band alignment of $Al_xGa_{1-x}As$ changes with respect to the Al content and the driven strain by the 3.7–3.77% lattice mismatch with GaP. Fig.7.1 shows the band alignment of a thin QW of $Al_xGa_{1-x}As$ with thickness of 0.4 nm. The band

alignment was calculated with considering the biaxial strain effect. The calculations were done for x_{Al} = 0.05 (Fig. 7.1), and x_{Al} = 0.4 (Fig. 7.1b) using the solid model theory [77, 79].

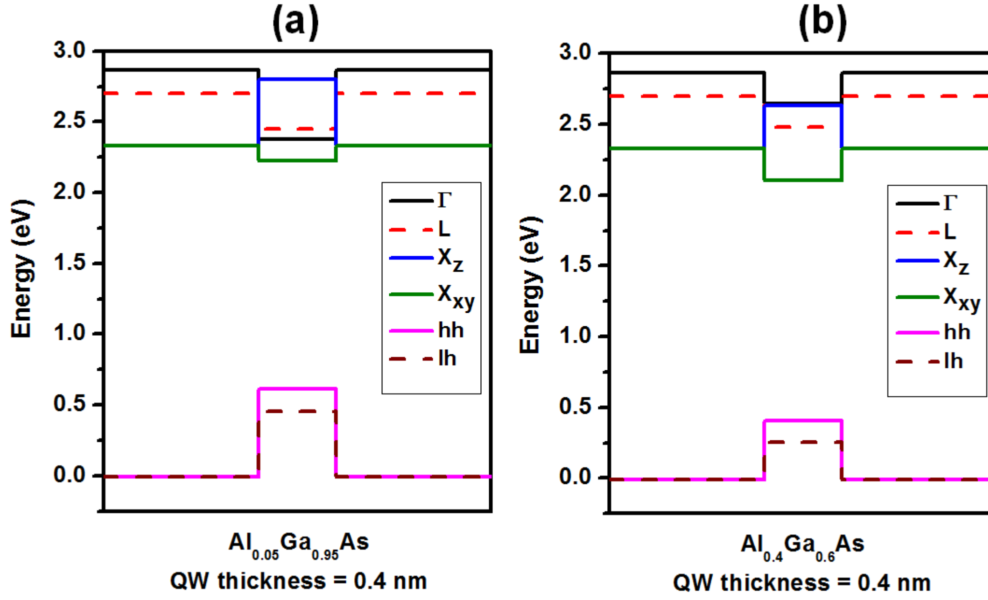

Figure 7.1: The band alignment of the strained $Al_{0.4}Ga_{0.6}As$ in GaP matrix. The thickness of QW is 0.4 nm for both (a) x_{Al} = 0.05, and (b) x_{Al} = 0.4. The black line represents the conduction band edge at Γ–valley, blue line is the conduction band at L–valley, red line show the conduction band at X–valley, green line is related to the hh and brown line demonstrates the lh.

The conduction band edge of $Al_xGa_{1-x}As$ at Γ–valley shifts upward due to the strain and the valence band splits to hh and lh bands. The biaxial strain causes also the splitting of the X–valley of the $Al_xGa_{1-x}As$ into two components in the xy–plane and in the z–axis. The results demonstrate that in the z–direction the minimum of the $Al_xGa_{1-x}As$/GaP system is located at X–valley of GaP. The maximum of valence band is situated at Γ–valley of $Al_xGa_{1-x}As$. Therefore, an indirect type–II heterointerface is predicated for the strained $Al_xGa_{1-x}As$ on GaP. The valence band edge of $Al_xGa_{1-x}As$ shifts downward with increasing the Al content from 0.05 to 0.5. While, the conduction band at Γ has an upward shift with increasing the Al content. The shift of the conduction band and valence band can be associated with the increase of the lattice mismatch and larger content of Al.

It is notable that E_g of the indirect type–II heterostructure increases with increas-

ing the Al content due to the downward shift of the valence band to lower energies. E_g increase from 1.75 eV for the Al content (x_{Al}) = 0.05 to 1.93 eV for x_{Al} = 0.4. Hence, shift of E_g toward the higher energy is predicted with increasing x_{Al}. Fig. 7.2 shows the results of the calculated E_g for different contents of Al. The blueshift of the bandgap energy with increasing the Al content is observed.

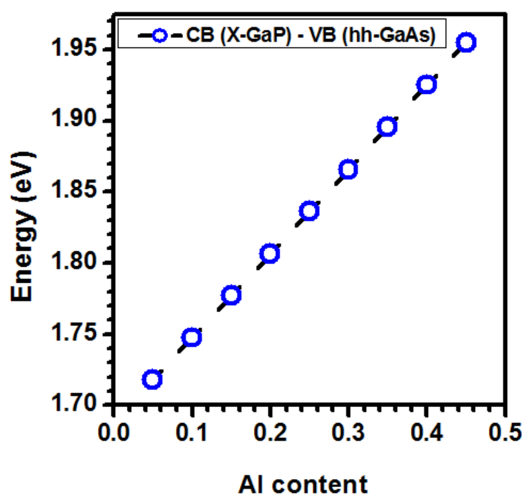

Figure 7.2: The variation of E_g with respect to the Al content. Open circles are related to the difference between the conduction band edge of GaP and valence band edge in Γ–valley of GaAs.

7.2 Growth and characterization of $Al_xGa_{1-x}As$/GaP

The growth of $Al_xGa_{1-x}As$ was done on the undoped GaP (001) substrates. The GaP buffer and cap layer were grown under the same growth conditions, T_G = 520 ^oC, growth rate of 0.83 μm/h, and thickness of 500 nm and 50 nm, respectively. The nominal contents of Al and Ga were determined with the temperature of the effusion cells, so that, the total growth rate of $Al_xGa_{1-x}As$ was equal to 0.3 ML/s. T_G = 450 ^oC was applied to grow the desired $Al_xGa_{1-x}As$ layer. The two different nominal thickness (1.2, and 2.7 ML) of $Al_xGa_{1-x}As$ with two different nominal contents of Al (x_{Al} = 0.3, and 0.5) were grown at 450 ^oC. To characterize the morphology of $Al_xGa_{1-x}As$ quantum structures, the growth of $Al_xGa_{1-x}As$ layer was repeated using the same growth condition on the 50 nm GaP layer. Fig. 7.3 shows the scheme of the grown samples.

The growth was monitored using the RHEED pattern. A sharp and streaky RHEED pattern was seen after the growth of the GaP buffer layer. The RHEED reconstruction demonstrate less intensity but the pattern did not transform to a spotty or broken lines after the growth of the $Al_xGa_{1-x}As$ layer with the nominal thicknesses in the range of 1.2–2.7 ML for nominal Al contents between 0.1 to 0.5. After the growth of 50 nm GaP layer, REHHD showed a streaky pattern. This may suggest the growth of a thin QW of $Al_xGa_{1-x}As$ between the GaP buffer layer and 50 nm GaP barrier.

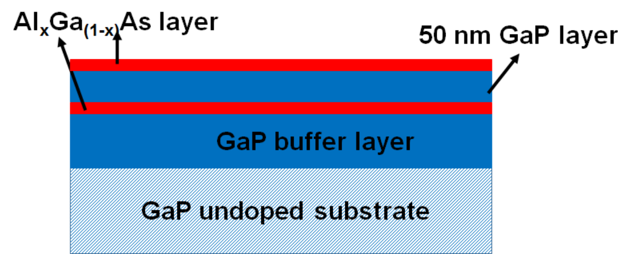

Figure 7.3: Scheme of the grown $Al_xGa_{1-x}As$/GaP samples including the 500 nm GaP buffer, desired thickness and Al content for $Al_xGa_{1-x}As$, 50 nm GaP layer, and final $Al_xGa_{1-x}As$ layer with the equivalent thickness and Al content of the previous $Al_xGa_{1-x}As$ layer.

The morphology of the quantum structures were investigated using the AFM measurements. Fig. 7.4 depicts the AFM results for $Al_xGa_{1-x}As$ samples with x_{Al}=0.5. The measurements were carried out in IKZ. The formation of the large oval shape structure is seen for both 1.2 and 2.7 ML $Al_{0.5}Ga_{0.5}$. The same oval shape structures are seen for 2.7 ML $Al_{0.3}Ga_{0.7}$. Fig. 7.3a presents,the scheme of the oval structures and the AFM results for $Al_{0.5}Ga_{0.5}$ layer with nominal thickness of 1.2 ML and 2.7 ML are shown in Fig. 7.4 b and c, respectively. According to the AFM results the average height, width, and length of the oval structures are 15±1 nm, 450±20 nm, and 1260±40 nm for different nominal thicknesses and nominal Al contents. The density of the oval structure is $3\pm1\times 10^6$ cm^{-2}. A semi–ellipsoid shape was considered for the oval structures. The average volume of one oval structure, therefore, is 3.1×10^7 nm^3. The WL thickness, therefore, can be estimated using the AFM results. The estimated WL is 0.6±0.05 nm for 2.7 ML samples and it is 0.25±0.05 nm for 1.2 ML sample.

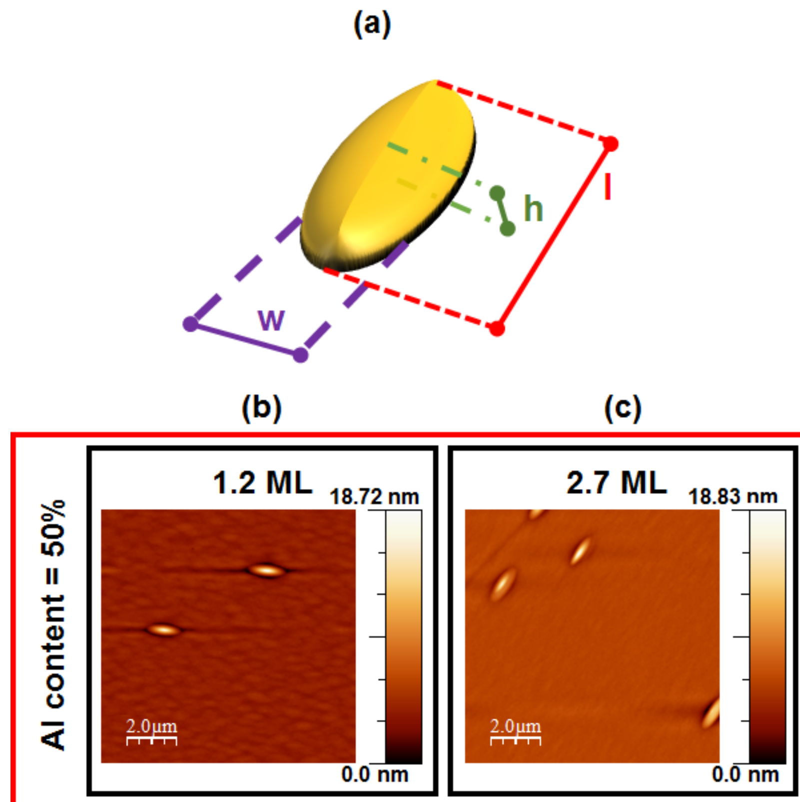

Figure 7.4: (a) Scheme of the oval shape structures, h, w, and l denote height, width, and length of the structures, respectively. AFM image of $Al_{0.5}Ga_{0.5}$ with nominal thickness of (b) 1.2 ML, and (c) 2.7 ML.

The formation of the oval structure may result from the agglomeration of the Ga and/or Al ad–atoms during the cooling down of the substrate [116]. These large oval structures may be considered as the defects that may participate as the non–radiative rather than the radiative centers in the emission. The structure on the surface of uncapped samples are not necessarily identical with the capped structure, particularly, due to the complex kinetic of the overgrowth of the $Al_xGa_{1-x}As$ layer by the GaP cap layer [155, 201] Consequently, based on the RHEED pattern, a thin QW can be suggested for the embedded $Al_xGa_{1-x}As$ layer in the GaP matrix.

The optical characterization were carried out at 80 K using the CL system in the group of Prof. J. Jimènez. Fig. 7.5 represents the results for the samples with identical nominal thickness of 2.7 ML and nominal Al contents of 0.0, 0.3, and 0.5. The spectrum of 2.7 ML GaAs indicates a broad peak with the FWHM of 78 nm. The spectra of the $Al_xGa_{1-x}As$ samples show, on the other hand, the 2 times nar-

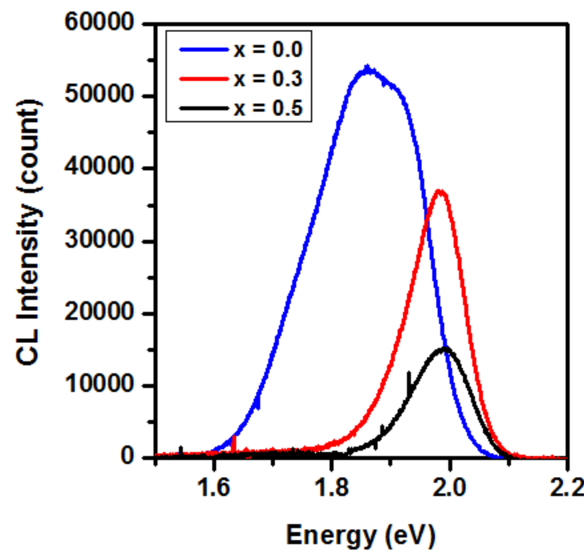

Figure 7.5: CL results of the samples with identical nominal thickness of 2.7 ML and different nominal Al contents at 80 K. Blue curve indicate the spectrum of x_{Al} = 0.0, while the CL results of x_{Al} = 0.3 is illustrated by the red curve, and black curve shows the results for x_{Al} = 0.5.

rower peaks. The broad peak of 2.7 ML GaAs sample is related to the multimodal size distribution of GaAs QDs (more information can be find in Chapter.6). The spectrum can be fitted by two Gaussian peaks located at peak–A = 1.93 eV and peak–B = 1.84 eV. Whereas, the spectra of 2.7 ML $Al_{0.5}Ga_{0.5}As$ and $Al_{0.3}Ga_{0.7}As$ illustrate one emission line (peak–A) at 1.98 eV and 1.99 eV, respectively. 50 meV shift of the emission line toward the higher energy range can be due to the larger bandgap energy of $Al_xGa_{1-x}As$/GaP system compared to GaAs/GaP. These results confirm our theoretically predicted blueshift of the bandgap energy with increasing the content of Al. 10 meV blueshift of the emission line for $Al_{0.5}Ga_{0.5}As$ compared to $Al_{0.3}Ga_{0.7}As$ is consistent with the theoretical calculations. The luminescence of the $Al_xGa_{1-x}As$/GaP indicates a lower intensity compared to the GaAs/GaP heterostructure. It may be attributed to the transition from a mixed type–II indirect and type–I direct heterointerface for GaAs/GaP to a pure type–II indirect system for $Al_xGa_{1-x}As$/GaP.

The quantum confinement effect can cause the shift of the emission line as well. To investigate the influence of the quantum confinement on the emission spectrum,

the $Al_{0.5}Ga_{0.5}$ samples with different nominal thickness of 1.2 ML and 2.7 ML were grown (Fig.7.6).

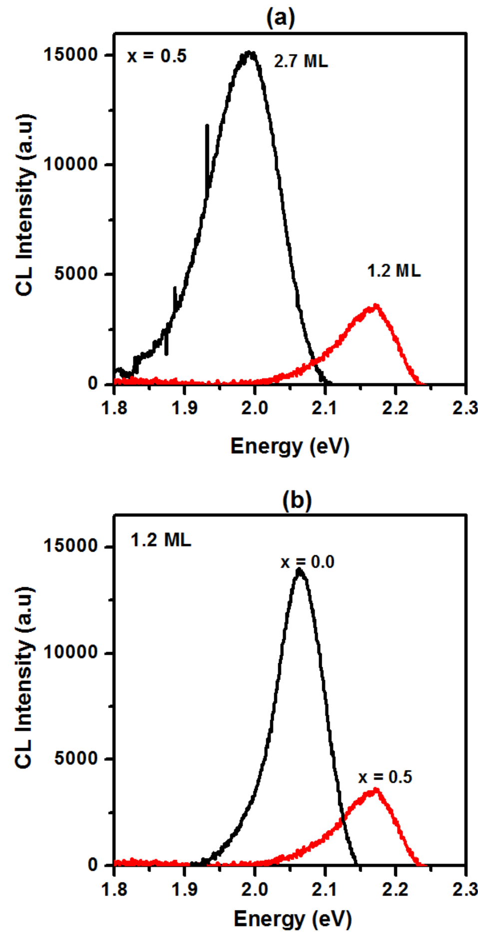

Figure 7.6: CL for (a) samples with identical Al nominal content (x = 0.5) and different nominal thicknesses of 1.2 ML (red curve) and 2.7 ML (black curve), (b) samples with identical nominal thickness of 1.2 ML and different Al nominal content of x = 0.0 (black curve) and x = 0.5 (red curve).

Fig. 7.6a shows the CL spectra of the two samples with identical nominal content of Al (x_{Al} = 0.5) and different nominal thickness of 1.2 ML and 2.7 ML. The confinement effect leads to the shift of the emission peak of $Al_{0.5}Ga_{0.5}As$ form 1.99 eV for 2.7 ML sample to 2.17 eV for 1.2 ML. The 180 meV shift toward higher energy range is related to the smaller AlGaAs QW that, in turn, pushes down the hh energy states toward lower energies, which are confined in the $Al_{0.5}Ga_{0.5}As$ QW. The downward shift of the hh states, on the other hand, can lead to the less

overlap between the wavefunctions of the electrons in the X–valley of GaP and hh in the Γ–valley of AlGaAs QW. This can be the origin of the less intensity of the emitted light by the 1.2 ML compared to 2.7 ML sample. Fig. 7.6b indicates the influence of the nominal content of Al for two samples with identical nominal thickness of 1.2 ML. The results demonstrate the shift of the emission peak from 2.07 eV to 2.17 eV with increasing the nominal content of Al from x_{Al} = 0.0 to x_{Al} = 0.5, respectively. The 100 meV shift toward higher energy may be attributed to the shift of the valence band and therefore, the hh states to lower energies with increasing the Al content. This corroborates the theoretical calculated blueshift of the bandgap energy with increasing the nominal content of Al.

Excitation density dependent PL measurement is a powerful approach to investigate a type–II heterostructure. Fig. 7.7 presents the results of the excitation density dependent PL measurement on 2.7 ML $Al_{0.5}Ga_{0.5}As$ sample. The measurements

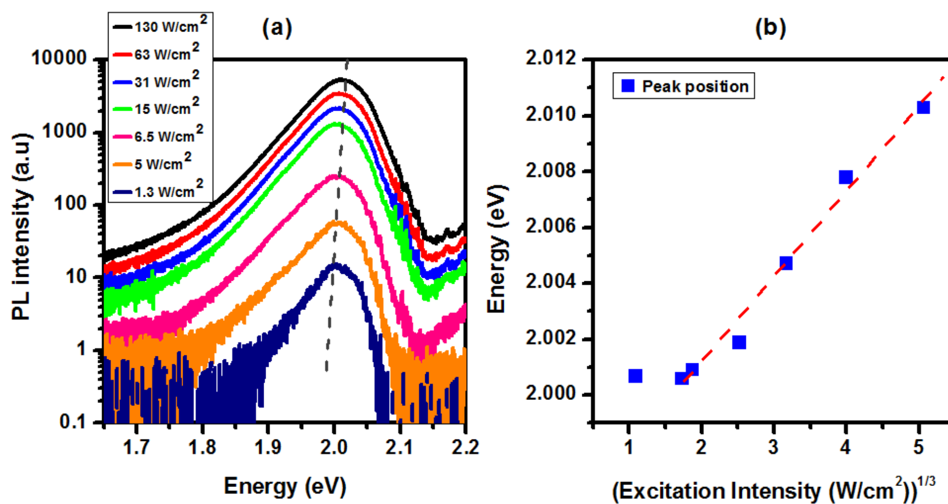

Figure 7.7: (a) Excitation density dependent Pl of $Al_{0.5}Ga_{0.5}As$ with respect to energy. The dash line is for eye guide. (b) The blueshift of the peak position with increasing the excitation density to the power of 1/3. the red dash line is for eye guide. Measurements were done at 10 K.

were carried out using a He–Cd laser with excitation wavelength of 325 nm and at 10 K (measurements were done in PDI with assistance of Dr. P. Corfdir). A linear shift of about 10 meV is observed with increasing the excitation density to the power of 1/3 (Fig. 7.7b). The blueshift with increasing the power density is a well

known behavior for the radiative transition in a type–II QW heterostructure [158] and it is attributed to the formation of the triangular potential well at the interface of the conduction band edge of GaP and AlGaAs. The higher excitation density leads to the occupation of the higher energy states in the triangular potential well that cause the blueshift of the radiative transition. The blueshift of the emission line with increasing the excitation density supports the calculated type–II indirect transition for $Al_xGa_{1-x}As$/GaP heterostructure.

Fig. 7.8 illustrates the results of the temperature–dependent PL measurements. The measurements were done on the 2.7 ML $Al_{0.5}Ga_{0.5}As$ sample in the range of 10–200 K, using the excitation wavelength of 325 nm and excitation density of 130 W/cm^2 (measurements were done in PDI with assistance of Dr. P. Corfdir). Fig. 7.8a shows the PL intensity with respect to the energy. The shift of the emission line toward lower energy range with increasing the temperature is also indicated [65]. The thermal quenching of the output intensity is seen. This may be attributed to the thermal escaping of the confined hh from AlGaAs QW. The thermal escaping of hh together with the less overlap between the electron and hole wavefunctions in a type–II indirect system result to the vanishing of the luminescence at temperatures higher than 200 K.

Fig. 7.8b shows the ratio of the integrated intensity with respect to the temperature. I/I_0 in the graph denotes the ratio of the integrated intensity as a function of temperature, I, to the maximum intensity that is related to the luminescence intensity at 10 K (I_0). The red line demonstrates the fitted curve using equation 6.1. The activation energy of E_1 = 60 meV was calculated using Arrhenius plot (6.1) [156]. The efficiency of the participation of this mechanism in the thermal quenching of output intensity is $c_1 = 1.6\times10^3$. The large c_1 together with the 60 meV activation energy can be the origin of the fast thermal quenching of the output which is followed by the vanishing of the luminescence for temperatures higher than 200 K. E_1 can be associated with the activation energies for thermal escaping of the confined hh in the $Al_{0.5}Ga_{0.5}As$ QW.

The calculated indirect type–II system for the $Al_xGa_{1-x}As$/GaP, therefore, corroborates with the experimental results. This picture is supported by the blueshift

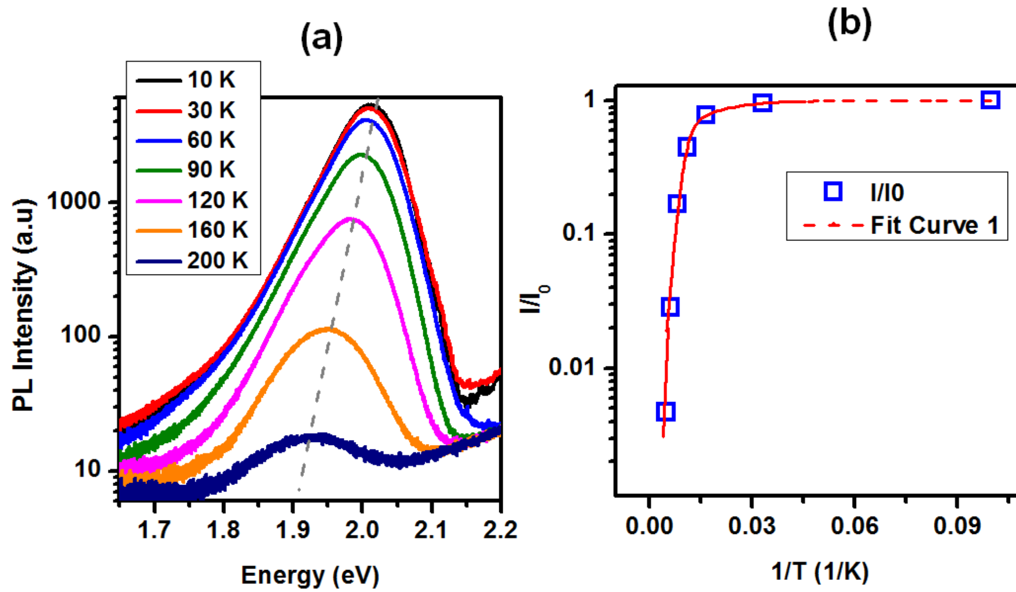

Figure 7.8: (a)Temperature dependent PL measurements with respect to the energy in the range of 10–200 K. The dash line is for eye guide and shows the redshift of the peak position with increasing the temperature(b) I/I_0 with respect to the temperature, the red line is the fitted curve using equation 6.1.

of the emission peak for higher excitation density and the fast thermal quenching that is followed by the destruction of the radiative recombination for temperatures higher than 200 K.

The experimental results can be interpreted using the following model. According to the structural results, RHEED and AFM, a thin $Al_xGa_{1-x}As$ QW is suggested for the embedded $Al_xGa_{1-x}As$ in the GaP matrix. This thin QW is fully strained and therefore, the conduction band edge of $Al_xGa_{1-x}As$ at Γ–valley shifts upward. Thus, electrons are located at the X–valley of GaP. The maximum of the valence band is, however, at Γ–valley of $Al_xGa_{1-x}As$ and related to the hh. Consequently, an indirect type–II system, in which e and h are located at different real– and *k*–space, is predicted for this system. The expected radiative transition, in this case, is related to e^X_{GaP} and $hh^\Gamma_{Al_xGa_{1-x}As}$. Fig. 7.9 shows the expected transition of e–hh in the $Al_xGa_{1-x}As$/GaP system.

This model is supported by the experimental results. The CL results indicate that the intensity reduces by a factor of 4 with increasing the Al content from 0.0 to 0.5. This can be associated with the transmission from a mixed type–I and type–II sys-

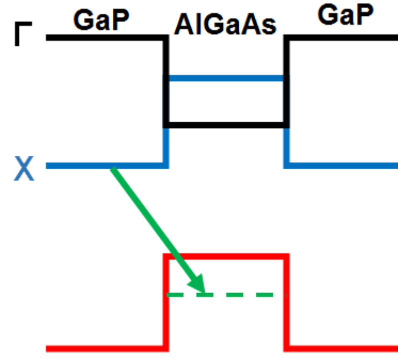

Figure 7.9: The band alignment of a thin $Al_xGa_{1-x}As$ QW in the GaP matrix. The black line represents the conduction band edge at Γ–valley, blue line shows the X–valley of conduction band, and the hh valence band is denoted by the pink line. The eligible e–hh transition is shown using the red arrow.

tem to a pure indirect type–II transition of electron and holes for $x_{Al} > 0.0$. The indirect type–II transition is referred to the e–hh that are located in different real–space and k–space which is followed by the less overlap between the wavefunctions of electron and holes. Thus, a less probability of the radiative recombination is expected. The excitation density dependent PL measurements demonstrate the linear blueshift of the peak position with increasing the power density to the power of 1/3. The blueshift of about 10 meV can be corresponded to the type–II QW system and occupation of the higher states in the triangular potential at interface of the conduction band edge of GaP and AlGaAs [158, 202]. The thermal quenching of the radiative intensity is observed and the luminescence vanishes for the temperature higher than 200 K. The type–II heterostructure in which holes are confined in the QW but electrons are located in the X–valley of GaP, therefore, can be the origin of the rapid destruction of the radiative recombination at high temperatures.

The exact content of the Al, however, is a subject of debate. Several investigations was done on the influence of segregation of the group–III elements [203, 204, 205]. Studies on AlGaAs/GaAs system suggest an interface roughness due to the segregation of Ga atoms [203, 205]. Segregation of the In atoms in the InGAs QDs grown on GaP (001) is also reported as a significant difficulty to determine the exact incorporated In atoms in the QDs structure, which changes the band alignment and the optical properties of the InGAs QDs [136]. The interface roughness and inter-

mixing can change the composition profile of the $Al_xGa_{1-x}As$ QW. The variation of the composition leads to the change of the band alignment and the variation of the emission spectra. A better study using TEM measurements, therefore, is needed to investigate the composition profile of the grown samples.

7.3 Summary

The growth of $Al_xGa_{1-x}As$ QW was demonstrated using the RHEED pattern and AFM analysis. Optical characteristic of the grown samples indicated the shift of the peak position toward higher energy with increasing the content of Al. The influence of the quantum confinement was illustrated in the shift of the peak position toward lower energy with increasing the nominal thickness of the grown $Al_xGa_{1-x}As$ QW for identical nominal content of Al. The results of the power density dependent PL measurements indicated the linear blueshift of the peak position with increasing the power density to the power of 1/3 that is consistent with the calculated type–II band alignment for the $Al_xGa_{1-x}As$ QW in the GaP matrix system. The calculation demonstrated that the expected transition is an indirect type–II between e and hh which are located at different real–space and k–space. The expected transition, therefore, occur between the e located at the X–valley of GaP and hh at the Γ–valley of $Al_xGa_{1-x}As$ QW.

Chapter 8

Conclusion

In this work, the critical influence of the growth conditions on the crystal and surface quality of the grown structures on GaP (001) substrate were investigated. The growth, structural and optical properties of GaAs QDs embedded in the GaP matrix were studied. The structural and optical features of the AlGaAs QWs grown in the GaP matrix were analyzed.

The influence of the PH_3 flux and growth temperature were studied on the surface and crystal quality of the homoepitaxial growth of GaP and heteroepitaxial growth of AlGaP [115]. It was shown that the crystal quality of the AlGaP sacrificial layer affects the quality of the thin GaP layer grown on the AlGaP. Therefore, it was suggested that the crystal quality of the AlGaP sacrificial layer acts as a key point to grow a high quality thin GaP cap layer that is going to be fabricated as the GaP membrane [206]. It was shown that the small window of PH_3 flux = 2.7 sccm with growth temperature = 490 ^{o}C is the optimum growth condition for AlGaP layer.

Under the proper growth conditions, formation of GaAs QDs via the Stranski–Krastanow mechanism was observed. The critical thickness for the 2D to 3D transition was observed to be 1.8 ML for GaAs/GaP system. It was found from the structural characterizations that the lateral and vertical size of GaAs QDs increased for the larger the nominal thickness. A multimodal size distribution was suggested for the QDs based on the AFM analyses. It was demonstrated that the thin QWs and small GaAs QDs are fully strained, while the increase of the size of the QDs is followed by the increasing of the relaxation degree.

The optical measurements showed the luminescence in the range of 1.7 eV to 2.07 eV. The broad emission spectra of the samples was attributed to the broad size distribution of the QDs. The shift of the spectra toward lower energy was observed with increasing the nominal thickness of the grown GaAs layer that was related to the quantum confinement effect and the formation of the larger QDs. An indirect type–II transition was proposed as the origin of the emission for the strained GaAs QDs. On the other hand, the calculations showed the downward shift of the conduction band edge of GaAs at Γ–valley with the increase of the relaxation degree for the larger GaAs QDs. Therefore, the emission of the large relaxed QDs was attributed to a direct type–I transition. This picture was supported

by the experimental results. The increase of the intensity and the radiative emission at room temperature for the 2.7 ML and 3.6 ML samples, and the shorter decay time with increasing the nominal thickness of GaAs corroborated the proposed model [165].

The influence of the growth temperature on the morphology of GaAs QDs was investigated. The structural characterization showed that the increase of the growth temperature leads to the morphology transformation from QDs to elongated QDs for the equivalent thickness of GaAs layer. The optical measurements indicated the redshift of the emission spectra with increasing the growth temperature that was associated with the formation of the larger QDs. The polarization PL measurements showed a five times larger luminescence polarization for the elongated QDs to the QDs. The output intensity of the samples with the elongated QDs was observed to be similar to the sample with QDs. It was proposed that the formation of mixed and screw defects, which behaves as the non–radiative recombination centers, may increase the probability of the non–radiative recombination and reduce the output luminescence of the samples including the large elongated QDs.

The fabrication of LEDs based on the GaAs QDs embedded in GaP matrix was shown. The EL was observed for the LEDs based on the 1.2 ML and 3.6 ML GaAs. The shift of the spectra toward lower energy range was observed with increasing the nominal thickness of the GaAs layer, which was attributed to the formation of the large QDs.

The influence of the Al content was studied on the optical and structural properties of $Al_xGa_{1-x}As$ embedded in the GaP matrix. CL showed a blueshift of the emission line with increasing the Al content. It was proposed based on the calculations that the AlGaAs/GaP is an indirect type–II heterostructure. This picture was confirmed by the rapid thermal quenching of the radiative recombination up to 200 K. This was attributed to the weak overlap between the wavefunction of electron and holes, which are located at different real–space and k–space. The blueshift of 10 meV with the increase of the excitation density also corroborated the type–II system.

Appendix

Appendix.I

Table 8.1: α and β for different semiconductors. The values have been obtained from experimental results [68].

III–V semiconductor	direct gap (Γ valley) α (mev/K)	direct gap (Γ valley) β (K)	indirect gap (X valley) α (mev/K)	indirect gap (X valley) β (K)
AlAs	0.885	530	0.7	530
AlP	0.5771	372	0.318	588
GaAs	0.5405	204	0.46	204
GaP	—	—	0.610	460
InAs	0.276	83	0.276	83
InP	0.49	273	—	—

Appendix.II

Table 8.2: Lattice and elastic constants of III-V semiconductors[78].

III-V semiconductor	a (Å)	C_{11}	C_{12}	C_{44}	D^{001}
AlAs	5.65	1.250	0.534	0.542	0.854
AlP	5.43	1.320	0.630	0.615	0.955
GaAs	5.65325	1.223	0.571	0.600	0.934
GaP	5.43	1.439	0.652	0.714	0.906
InAs	6.08	0.833	0.453	0.396	1.088
InP	5.87	1.022	0.576	0.460	1.127

Appendix.III

Table 8.3: Spin–orbit splitting, bandgap energy, valence and average energy, and conduction band energy of III–V semiconductors that were used in this work [78].

III–V semiconductor	Δ_0	$E_{v,av}$	a_v	E_g	E_c	a_c
$AlAs^{ind}$	0.28	-7.49	2.47	2.23	-5.17	4.09
AlP^{ind}		-8.09	3.15	2.51	-5.58	5.12
GaAs	0.34	-6.92	1.16	1.52	-5.29	-7.17
GaP^{ind}	0.08	-7.40	1.70	2.35	-5.02	3.26
InAs	0.38	-6.67	1.00	0.41	-6.13	-5.08
InP	0.11	-7.04	1.27	1.42	-5.58	-5.04

Bibliography

[1] R. Zallen and W. Paul, Band Structure of Gallium Phosphide from Optical Experiments at High Pressure, Phys. Rev. **134**, A1628 (1964).

[2] H. B. Panish and H. C. Casey, Temperature Dependence of the Energy Gap in GaAs and GaP, J. Appl. Phys. **40** 1, 163−167 (1969).

[3] J. R. Lang, J. Faucher, S. Tomasulo, K. N. Yaung, and M. L. Lee, Comparison of GaAsP solar cells on GaP and GaP/Si, Appl. Phys. Lett. **103**, 092102 (2013).

[4] T. Soga, T. Suzuki, M. Mori, Z.K. Jiang, T. Jimbo, M. Umeno, Electrical properties of GaP on Si grown by metalorganic chemical vapor deposition, J. Cry. Growth. **132**, 414-418 (1993).

[5] K. J. Bachmann, U. Rossow, N. Sukidi, H. Castleberry, and N. Dietz, Heteroepitaxy of GaP on Si(100), J. Vac. Sci. Technol. B. **14(4)**, 3019 (1996).

[6] Y. Song, and M. L. Lee, InGaAs/GaP quantum dot light-emitting diodes on Si, Appl. Phys. Lett. **103**, 141906 (2013).

[7] H. J. Scheel, Introduction to Liquid Phase Epitaxy, John Wiley & Son, New York, Ltd, (2007).

[8] M. L. Hitchman, Chemical vapor deposition: principles and applications, London u.a.: Academic Press u.a.,(1993).

[9] K. E. Spear, Principles and applications of chemical vapor deposition, Pure and Applied Chemistry, **54(7)**, (1982).

[10] R.E. Enstrom, E. A. Miller, and A. G. Sigai, Vapor phase growth system and its use in the preparation of several III-V compound semiconductors, RCA Laboratories, United States, Washington, D.C.: National Aeronautics and Space Administration ; Springfield, Va.: National Aeronautics and Space Administration, (1971).

[11] John D. Joannopoulos, Steven G. Johnson, Joshua N. Winn, Robert D. Meade, Photonic Crystals Modeling the Flow of Light, Princeton University, second edition (2008).

[12] H. Altug, PHYSICS AND APPLICATIONS OF PHOTONIC CRYSTAL NANOCAVITIES, Stanford University, ©Copyright by Hatice Altug (2007).

[13] H.Benisty, PHOTONIC CRYSTALS New designs to confine light, Nature Physics, **1**,(2005).

[14] K. Rivoire, S. Buckley, F. Hatami, J. Vučković, Second harmonic generation in GaP photonic crystal waveguides, Appl. Phys. Lett. **98**, 263113 (2011).

[15] J. D. Joannopoulos, P. R. Villeneuve, S. Fan, Photonic crystals: putting a new twist on light, Nature. **386**, 143 (1997).

[16] T. Tanabe, M. Notomi, S. Mitsugi, A. Shinya, E. Kuramochi, All-optical switches on a silicon chip realized using photonic crystal nanocavities, Appl. Phys. Lett. **87**, 151112 (2005).

[17] I. Fushman, E. Waks, D. Englund, N. Stoltz, P. Petroff, J. Vučković, Ultrafast nonlinear optical tuning of photonic crystal cavities, Appl. Phys. Lett. **90**, 091118 (2007).

[18] M. B. Panish, I.Hayashi, S. Sumski, A Technique for the Preparation of Low-Threshold Room-Temperature GaAs Laser Diode Structures, IEEE J. QE-**5**, 210 (1969).

[19] I.Hayashi, M. B. Panish, P. W. Foy, A Low-Threshold Room-Temperature Injection Laser, IEEE J. QE-**5**, 211 (1969).

[20] M. B. Panish, H. Temkin, Gas Source Molecular Beam Epitaxy: Growth and properties of Phosphorous Containing III-V Heterostructures, Springer-Verlag Berlin Heidelberg, (1993).

[21] M. A. Herman, H. Sitter, Molecular Beam Epitaxy,**chapter 1**, Fundamentals and Current Status, Springer-Verlag Berlin Heidelberg, (1989).

[22] M. Henini, Molecular Beam Epitaxy: From research to mass production, Elsevier Inc. (2013).

[23] K. Bayrappa, T. Ohachi, Crystal Growth Technology, William Andrew Inc., Norwich, New York, **chapter 3**, (2003).

[24] A. Ichimiya, P. I. Cohen, Reflection High-Energy Electron Diffraction, Cambridge [u.a.]: Cambridge Univ. Press, (2010).

[25] V. P. LaBella, M. R. Krause, Z. Ding, P. M. Thibado, Arsenic-rich GaAs(0 0 1) surface structure, Surface Science Reports, **60**, 1−53 (2005).

[26] W. Braun, Applied RHEED: reflection high-energy electron diffraction during crystal growth, Berlin [u.a.]: Springe, (1999).

[27] C. L. Briant, Auger electron spectroscopy, Boston u.a.: Acad. Pr., (1988).

[28] H. Fujiwara, Spectroscopic ellipsometry: principles and applications, Chichester: Wiley, (2007).

[29] G. Bauer, W. Richter, Optical Characterization of Epitaxial Semiconductor Layers, **chapter 2**, Springer-Verlag Berlin Heidelberg, (1996).

[30] L. I. Maissel, R. Glang (eds.), Hand book of Thin Film Technology, McGraw-Hill, New York, (1970).

[31] http://www.pinstopin.com/a-c-pressure-readings/

[32] C. H. L. Goodman, M. V. Pessa, Atomic layer epitaxy, J. Appl. Phys. **60**, R 65 (1986).

[33] Y. Ota, Thin Solid Films, Silicon molecular beam epitaxy, **106**, 3-136 (1983).

[34] J. E. Davey,T. Pankey, Epitaxial GaAs Films Deposited by Vacuum Evaporation, J. Appl. Phys. **39**, 1941 (1968).

[35] J. A. Venables, G. D. T. Spiller, and M. Hanbücken, Nucleation and growth of thin films, Rep. Prog. Phys., **47**, 399-459 (1984).

[36] K.Oura, V. G. Lifshits, A. A. Saranin, A. V. Zotov, and M. Katayama, Surface Science: An Introduction, Springer-Verlag Berlin, **chapter 14**, (2003).

[37] E. Bauer and H. Popper. Recent advances in epitaxy. Thin Solid Films, **12(1)**:167âĂŞ185, (1972).

[38] I. Daruka and A-L. Barabási, Dislocation-Free Island Formation in Heteroepitaxial Growth: A study at Equilibrium, Phys. Rev. Let. **79**, 3708-3711 (1997).

[39] W. Seifert, N. Carlsson, M. Miller, M. E. Pistol, L. Samuelson, and L. R. Wallenberg, IN-SITU GROWTH OF QUANTUM DOT STRUCTURES BY THE STRANSKI-KRASTANOW GROWTH MODE, Prog. Crystal Growth and Charact, **33**, 423−471 (1996).

[40] A. Baskaran1, and P. Smereka, Mechanisms of Stranski-Krastanov growth, J. Appl. Phys. **111**, 044321 (2012).

[41] C. Ratsch and A. Zangwill. Equilibrium theory of the Stranski-Krastanov epitaxial morphology. Surf. Sci., **293:123âĂŞ131**, (1993).

[42] F. Hatami, Indium Phosphide Quantum Dots in GaP and in $In_{0.48}Ga_{0.52}P$, Ph.D. thesis, (2002).

[43] B. J. Spencer and J. Tersoff, Dislocation energetica in epitaxial strained islands, Appl. Phys. Lett., **77**, 2533 (2000).

[44] D. Vanderbilt and L. K. Wickham, Elastic Energies of Coherent Germanium Islands on Silicon, Mat. Res. Soc. Symp. Proc. **202**, (1991).

[45] L. Goldstein, F. Glas, J. Y. Marzin, M. N. Charasse, and G. Le Roux, Growth by molecular beam epitaxy and characterization of InAs/GaAs strained-layer superlattices, Appl. Phys. Lett. **47**, 1099 (1985).

[46] N. W. Ashcroft, N. D. Mermin, Solid State Physics. **Chapter 6**, Harcourt, Inc. (1976).

[47] D. K. Bowen, B. K. Tanner, High Resolution X-ray Diffractometry and Topography, This edition published in the Taylor & Francis e-Library, (2005).

[48] M. A. Capano, K. L . Kavanagh, S. Bensoussan, L. W. Hobbs, Analysis of Semiconductor by Double-Crystal X-RAY Diffractometry, The Rigaku Journal. **5**, 1 (1988).

[49] L. Tapfer and K. Ploog, Improved assessment of structural properties of $Al_xGa_{(1-x)}As$/GaAs heterostructures and superlattices by double-crystal x-ray diffraction, Phys. Rev. B. **33**, N. 5, 5565−5574 (1986).

[50] J. E. Bailey, P. B. Hirsch, The Dislocation Distribution, Flow Stress, and Stored Energy in Cold-worked Polycrystalline Silver, Philosophical Magazine, **5:53**, 485−497 (1960).

[51] P. E. West, Introduction to Atomic Force Microscopy: Theory, Practice, Applications, ©Copyright (2009) Paul West.

[52] Scanning Electron Microscope A to Z, Basic Knowledge to use SEM, JEOL.

[53] B. G. Yacobi and D. B. Halt, Cathodoluminescence Microscopy of Inorganic Solids, New York, N.Y.: Plenum Press, (1990).

[54] Guide to Strike Cameras, Hamamatsu

[55] K. Kanayat, and S. Okayama, Penetration and energy-loss theory of electrons in solid targets, J. Phys. D: Appl. Phys. **5**, 43−58 (1972).

[56] D. Drouin, A. R. Couture, D. Joly, X. Tastet, V. Aimez, R. Gauvin, CASINO V2.42-A Fast and Easy-to-use Modeling Tool for Scanning Electron Microscopy and Microanalysis Users, SCANNING, **29**, 92−101 (2007).

[57] P. Y. Yu and M. Cardona, Fundamentals of Semiconductors-Physics and Materials Properties, **Fourth edition**, Springer-Verlag Berlin Heidelberg, (2010).

[58] S. M. Sze and Kwok K. Ng, Physics of Semiconductor Devices, **Third edition**, John Wiley & Sons, Ltd. (2007).

[59] C. Kittel, Introduction to Solid States Physics, **chapter 14**, John Wiley & Sons, Inc, (1953).

[60] N. W. Ashcroft, N. D. Mermin, Solid State physics, **chapter 28 and 29**, Harcourt, Inc, (1976).

[61] lab.frumania.com.

[62] J. Singh, Electronic and Optoelectronic Properties of Semiconductor Structures, **chapter 2**,CAMBRIDGE UNIVERSITY PRESS, (2003).

[63] N. W. Ashcroft, N. D. Mermin, Solid. State. Physics. **chapter 10 and 11**, Harcourt, Inc. (1976).

[64] I. Vurgaftman, J. R. Meyer, and L. R. Ram-Mohan, Band parameters for III-V compound semiconductors and their alloys, J. Appl. Phys. **89**, 5815−5875 (2001).

[65] Y. P. Varshni, Temperature dependence of the energy gap in semiconductors, Physica. **34**, 149-154 (1967).

[66] K. P. O′Donnell and X. Chen, Temperature dependence of semiconductor bandgaps, Appl. Phys. Lett. **58**, No. 25 (1991).

[67] S. Adachi, "Properties of Group IV, III-V, and II-VI Semiconductors", John Wiley & Sons, Ltd, (2005).

[68] http://www.ioffe.rssi.ru.

[69] D. Bimberg, M. Grundmann, N. N. Ledenstov, Quantum Dot Heterostructures, John Wiley & Sons, Ltd. (1999).

[70] W. R. Frensley, nd N. G. Einspruch, Heterostructures and Quantum Devices, **chapter 1**, A volume of VLSI Electronics: Microstructure Science, (Academic Press, San Diego), (1994).

[71] P. Harrison, QUANTUM WELLS, WIRES AND DOTS- Theoretical and Computational Physics of Semiconductor Nanostructures, John Wiley & Sons Ltd, **Second edition**, (2005).

[72] Y. Sun, S. Thompson, T. Nishida, Strain Effect in Semiconductors: Theory and Device Applications, New York [u.a.] : Springer, (2010).

[73] R. L. Anderson, Experiment on Ge-GaAs Heterojunctions, Solid-States. Electronic. **5**, 341-351 (1962).

[74] D. T. Calow, P. d. Deasley, S. J. T. Owen, P. W. Webb, A Review of Semiconductor Heterojunctions, J. Mater. Sci. **2**, 88-96 (1967).

[75] J. Tersoff, Theory of semiconductor heterojunctions: The role of quantum dipoles, Phys. Rev. B. **30**, 4874 (1984).

[76] E. T. Yu, J. O . McCaldin, T. C. McGill, Band Offsets in Semiconductor Heterojunctions, Solid Stats Physics. **46**, 1-146 (1992).

[77] C. G. Van de Walle, R. M. Martin, Theoretical study of band offsets at semiconductor interfaces, Phys. Rew. B. **35**, (1987).

[78] C. G. Van de Walle, Band lineups and deformation potentials in the model-solid theory, Phys. Rew. B. **39**, 1871−1883 (1989).

[79] S. Birner, T Zibold, T Andlauer, T Kubis, M Sabathil, A. Trellakis, P. Vogl, nextnano: General Purpose 3-D Simulations, IEEE Transactions on Electron Devices,**54**, 2137(2007).

[80] S. M. Sez, M. K. Lee, Semiconductor devices, physics and technology, John Wiley & Sons, Inc, 3ed Edition, (2012).

[81] M. Razeghi, Technology of Quantum Devices, Springer US: Boston, MA, (2010).

[82] E. F. Schubert, LIGHT-EMITTING DIODES, Cambridge University Press, (2003).

[83] J. P. Colinge, C. A. Colinge, Physics OF Semiconductor Devices, ©KLUWER ACADEMIC PUBLISHERS,(2002).

[84] G. E. Moore, Cramming more components onto integrated circuits, Electronics. **38**, Number 8 (1965).

[85] E. Matioli, and C. Weisbuch, Impact of photonic crystals on LED light extraction efficiency: approaches and limits to vertical structure designs, J. Phys. D: Appl. Phys. **43**, 354005 (2010).

[86] F. Koyama, S. Kinoshita, and K. Iga, Room-temperature continuous wave lasing characteristics of a GaAs vertical cavity surface-emitting laser, Appl. Phys. Lett. **55**, 221 (1989).

[87] J.L. Jewell, J. P. Harbison, A. Scherer, Y.H. Lee, L.T. Florez, Vertical-cavity surface emitting lasers: Design, growth, fabrication, characterization, IEEE J. Quantum Electron. **27**, 1332−1346 (1991).

[88] P. Berme, C. Luo, L. Zeng, L. C. Kimerling, and J. D. Joannopoulos, OPTICS EXPRESS. **15**, No. 25, 16986 (2007).

[89] B. Troia, A. Paolicelli, F. De Leonardis and V. M. N. Passaro, Photonic Crystals for Optical Sensing: A Review, **chapter 11**, (2013).

[90] K. M. Ho, C. T. Chan, C. M. Soukoulis, R. Biswas and M. Sigalas, Solid. State. Communications. **89**, No. 5, 413−416 (1994).

[91] S. Y. Lin, J. G. Fleming, D. L. Hetherington, B. K. Smith, R. Biswas, K. M. Ho, M. M. Sigalas, W. Zubrzycki, S. R. Kurtz, and Jim Bur, Nature. **394**, (1998).

[92] S. Noda, et al., Full Three-Dimensional Photonic Bandgap Crystals at Near-Infrared wavelengths, Science. **289**, 604 (2000).

[93] G. Fleming and S. -Y. Lin, Three-dimensional photonic crystal with a stop band from 1.35 to 1.95 μm, Opt. Let. **24**, 49−51 (1999).

[94] P. Lodahl, et al., Controlling the dynamics of spontaneous emission from quantum dots by photonic crystals, Nature. **430**, 654−657 (2004).

[95] S. Ogawa, et al., Control of Light Emission by 3D Photonic Crystals, Science. **305**, 227−229 (2004).

[96] T. Asano, B-S. Song, S. Noda, Analysis of the experimental Q factors ($\sim$1 million) of photonic crystal nanocavities, OPTICS EXPRESS, **14**, No. 5 (2006).

[97] J. W. Morris, Jr., A Survey of Materials Science I. Structure, **chapter 4**, Department of Materials Science and Engineering University of California, Berkeley, (2007).

[98] C. Kittel, Introduction to Solid States Physics, **chapter 16**, John Wiley & Sons, Inc, (1953).

[99] N. W. Ashcroft, N. D. Mermin, Solid State physics, **chapter 30**, Harcourt, Inc. (1976).

[100] M. Ohring, The Materials Science of Thin Films,**chapter 1**, (1991).

[101] P. Gay, P.B. Hirsch, and A. Kelly, The estimation of dislocation densities in metals from X-ray data, Acta Metallurgica. **1**, 315 (1953).

[102] David J. Whitehouse, Surfaces and their Measurement, Elsevier Science & Technology, Hermes Penton Ltd, First published in (2002).

[103] Y.-S. Choi, K. Hennessy, R. Sharma, E. Haberer, Y. Gao, S.P. DenBaars, et al., GaN blue photonic crystal membrane nanocavities, Appl. Phys. Lett. **87**, 243101 (2005).

[104] C.-F. Lai, P. Yu, T.-C. Wang, H.-C. Kuo, T.-C. Lu, S.-C. Wang, et al., Lasing characteristics of a GaN photonic crystal nanocavity light source, Appl. Phys. Lett. **91**, 041101 (2007).

[105] A.M. Adawi, A.R. Chalcraft, D.M. Whittaker, D.G. Lidzey, Refractive index dependence of L3 photonic crystal nano-cavities, Opt. Express. **15**, 14299 (2007).

[106] D.F. Nelson, Electro-optic and Piezoelectric Coefficients and Refractive Index of Gallium Phosphide, J. Appl. Phys. **39**, 3337 (1968).

[107] S. Buckley, K. Rivoire, F. Hatami, J. Vučković, Quasiresonant excitation of InP/InGaP quantum dots using second harmonic generated in a photonic crystal cavity, Appl. Phys. Lett. **101**, 161116 (2012).

[108] K. Rivoire, A. Faraon, J. Vuckovic, Gallium phosphide photonic crystal nanocavities in the visible, Appl. Phys. Lett. **93**, 063103 (2008).

[109] K. Rivoire, A. Kinkhabwala, F. Hatami, W.T. Masselink, Y. Avlasevich, K. Müllen, et al., Lithographic positioning of fluorescent molecules on high-Q photonic crystal cavities, Appl. Phys. Lett. **95**, 123113 (2009).

[110] C. Ratcliff, T.J. Grassman, J. a. Carlin, S. a. Ringel, High temperature step-flow growth of gallium phosphide by molecular beam epitaxy and metalorganic chemical vapor deposition, Appl. Phys. Lett. **99**, 141905 (2011).

[111] J. N. Baillargeon, K.Y. Cheng, K.C. Hsieh, Surface structure of (100) GaP grown by gas source molecular beam epitaxy, Appl. Phys. Lett. **56**, 2201 (1990).

[112] I. Horcas, R. Fernández, J.M. Gómez-Rodríguez, J. Colchero, J. Gómez-Herrero, a M. Baro, WSXM: a software for scanning probe microscopy and a tool for nanotechnology., Rev. Sci. Instrum. **78**, 013705 (2007).

[113] W.G. Bi, High resolution x-ray diffraction studies of AlGaP grown by gas-source molecular-beam epitaxy, J. Vac. Sci. Technol. B Microelectron. Nanom. Struct. **13**, 754 (1995).

[114] J.N. Baillargeon, K.Y. Cheng, K.C. Hsieh, G.E. Stillman, The gas source molecular beam epitaxial growth of $Al_xGa_{1x}P$ on (100) GaP, J. Appl. Phys. **68**, 2133 (1990).

[115] S. Dadgostar, E.H. Hussein, J. Schmidtbauer, T. Boeck, F. Hatami, W.T. Masselink, Structural properties of AlGaP films on GaP grown by gas-source molecular-beam epitaxy, Journal of Crystal Growth, **425**, 94 - 98 (2015).

[116] S. Matteson, H. D. Shih, Morphological studies of oval defects in GaAs epitaxial layers grown by molecular beam epitaxy, Appl. Phys. Lett. **48**, 47 (1986).

[117] M.Asada, Y. Miyamoto, and Y. Suematsu, Gain and the Threshold of Three-Dimensional Quantum-Box Lasers, IEEE J.Quantum Elect. **22**, 1915(1986).

[118] M. Henini, SELF-ASSEMBLED QUANTUM DOTS FOR OPTOELECTRONIC DEVICES: PROGRESS AND CHALLENGES, 2nd CEPHONA Workshop on Microscopic Characterisation of Materials and Structures for Photonics, Warsaw, (2004).

[119] A. O. Kosogov,P. Werner, and U. Gösele, N. N. Ledentsov, D. Bimberg, V. M. Ustinov, A. Yu. Egorov, A. E. Zhukov, P. S. Kop̆ev, N. A. Bert, and Zh. I. Alferov, Structural and optical properties of InAs-GaAs quantum dots subjected to high temperature annealing, Appl. Phys. Lett. **69**(20), 3072 (1996).

[120] M.Grundmann, O.Stier, and D.Bimberg, InAs/GaAs pyramidal quantum dots: Strain distribution, optical phonons, and electronic structure, Phys.Rev.B. **52**,11969 (1995).

[121] E. Placidi, F. Arciprete, R. Magri, M. Rosini, A. Vinattieri, L. Cavigli, M. Gurioli, E. Giovine, L. Persichetti, M. Fanfoni, F. Patella, and A. Balzarotti, InAs Epitaxy on GaAs(001): A Model Case of Strain-Driven Self-assembling of Quantum Dots, DOI 10.1007/978-1-4614-0742-3-2, Springer Science+Business Media, LLC (2012).

[122] H-M Ji, B. Liang, P. J. Simmonds, B-C Juang, T. Yang, R. J. Young, and D. L. Huffaker, Hybrid type-I InAs/GaAs and type-II GaSb/GaAs quantum dot structure with enhanced photoluminescence, Appl. Phys. Lett. **106**, 103104 (2015).

[123] R. B. Laghumavarapu, A. Moscho, A. Khoshakhlagh, M. El-Emawy, L. F. Lester, and D. L. Huffaker, GaSb / GaAs type II quantum dot solar cells for enhanced infrared spectral response, Appl. Phys. Lett. **90**, 173125 (2007).

[124] R. Leon, C. Lobo, T. P. Chin, J. M. Woodall, S. Fafard, S. Ruvimov, Z. Liliental-Weber, M. A. Stevens Kalceff, Self-forming InAs/GaP quantum dots by direct islands growth, Appl. Phys. Lett. **72**, 1356 (1998).

[125] F. Hatami, W. T. Masselink, and L. Schrottke, Radiative recombination from InP quantum dots on (100) GaP, Appl. Phys. Lett. **78**, 2163 (2001).

[126] J. C. P. Chang, T. P. Chin, and J. M. Woodall, Incoherent interface of InAs grown directly on GaP (001), Appl. Phys. Lett., **69** (7), 981 (1996).

[127] G. B. Stringfellow and M. G. Craford, High Brightness Light Emitting Diodes in Semiconductors and Semimetals,Academic Press London, **48**, (1997).

[128] E. F. Schubert, Light Emitting Diodes, Cambridge University Press, Cambridge, U.K. (2003).

[129] C. Golz, Prozessierung und optoelektronische Charakterisierung von LEDs basierend auf (Al, Ga)As Quantenpunkten und Quantentöpfen in GaP, M.Sc thesis, Humboldt University of Berlin.

[130] F. Hatami, W. T. Masselink, L. Schrottke, J. W. Tomm, V. Talalev, C. Kristukat, A. R. Goñi, InP quantum dots embedded in GaP: Optical properties and carrier dynamics, Phys. Rev. B. **67**, 085306 (2003).

[131] A. R. Goñi, C. Kristukat, F. Hatami, S. Dreßler, W. T. Masselink, and C. Thomsen, Electronic structure of self-assembled InP/GaP quantum dots from high-pressure photoluminescence, Phys. Rev. B. **67**, 075306 (2003).

[132] A. R. Goni, C. Kristukat, F. Hatami, S. DreÃ§ler,W.T. Masselink, and C. Thomsen, High-pressure photoluminescence study of the electronic structure of InP/GaP quantum dots, Phys. stat. Sol. (b). **235(2)**, 412-416 (2003).

[133] E. H. Chen, T. P. Chin, J. M. Woodall, and M. S. Lundstrom, Electrical characteristics of nearly relaxed InAs/GaP heterojunctions, Appl. Phys. Lett. **70** (12), 1551 (1997).

[134] H. Moriya, Y. Nonogaki, S. Fuchi, A. Koizumi, Y. Fujiwara, Y. Takeda, Growth mode transition of InGaAs in OMVPE growth on GaP (001), Microelectronic Engineering, **51-52**, 35-42 (2000).

[135] Y. Song, P. J. Simmonds, and M. L. Lee, Self-assembled $In_{0.5}Ga_{0.5}As$ quantum dots on GaP, Appl. Phys. Lett. **97**, 223110 (2010).

[136] T. N. Thanh, C. Robert, C. Cornet, M. Perrin, J. M. Jancu, N. Bertur, J. Even, N. Chevalier, H. Folliot, O. Durand, and A. Lr Corre, Room temperature photoluminescence of high density (In,Ga)As/GaP quantum dots, Appl. Phys. Lett. **99**, 143123 (2011).

[137] J. Shen, Y. Song, M. L. Lee, and J. J. Cha, Spatially resolved In and As distributions in InGaAs/GaP and InGaAs/GaAs quantum dot systems, Nanotechnology. **25**, 465702 (2014).

[138] G. Stracke, A. Glacki, T. Nowozin, L. Bonato, S. Rodt, C. Prohl, A. Lenz, H. Eisele, A. Schliwa, A. Strittmatter, U. W. Pohl and D. Bimberg, Growth of $In_{0.25}Ga_{0.75}As$ quantum dots on GaP utilizing a GaAs interlayer, Appl. Phys. Lett. **101**, 223110 (2012).

[139] C. Robert, C. Cornet, P. Turban, T. N. Thanh, M. O. Nestoklon, J. Even, J. M. Jancu, M. Perrin, H. Folliot, T. Rohel, S. Tricot, A. Balocchi, D. Lagarde, X. Marie, N. Bertru, O. Durand, and A. Le Corre, Electronic, optical, and structural properties of (In,Ga)As/GaP quantum dots, Phys. Rev. B. **86**, 205316 (2012).

[140] C. Robert, T. Thanh, C. Cornet, P. Turban, M. Perrin, A. Balocchi, H. Folliot, N. Bertru, L. Pedesseau, M. O Nestoklon, J. Even, J-M. Jancu, S. Tricot, O. Durand, X. Marie, A. Le Corre, Theoretical and experimental studies of (In,Ga)As/GaP quantum dots, Nanoscale. Res. Lett. **7:643**, (2012).

[141] C. Prohl, A. Lenz, D. Roy, J. Schuppang, G. Stracke, A. Strittmatter, U. W. Pohl, D. Bimberg, H. Eisele, and M. Dähne, Spatial structure of $In_{0.25}Ga_{0.75}As$/GaAs/GaP quantum dots on the atomic scale, Appl. Phys. Lett. **102**, 123102 (2013).

[142] J. Shen, Y. Song, M. L. Lee, and J. J. Cha, Spatially resolved In and As distributions in InGaAs/GaP and InGaAs/GaAs quantum dot systems, Nanotechnology. **25**, 465702 (2014).

[143] Y. Song, and M. L. Lee, Room temperature electroluminescence from light-emitting diodes based on $In_{0.5}Ga_{0.5}As$/GaP self-assembled quantum dots, Appl. Phys. Lett. **100**, 251904 (2012).

[144] M.-E. Pistol, M. R. Leys, L. Samuelson, Properties of thin strained Ga(As,P) layer, Phys. Rev. B. **37**, 4664 (1988).

[145] M. Recio, G. Armelles, J, Meléndez, and F. Briones, Optical properties of GaAs/GaP strainedlayer superlattices, J. Appl. Phys. **67**, 2044 (1990).

[146] J. Arriaga, M. C. Muñoz, V. R. Velasco, and F. García-Moliner, Electronic structure of strained GaAs/GaP (001) superlattices, Phys. Rev. B. **43**, 9626 (1991).

[147] J. A. Prieto, G. Armelles, M.-E. Pistol, P. Castrillo, J. P. Silveria, and F. Briones, Ootical studies of GaAs quantum wells strained to GaP, Appl. Phys. Lett. **70**, 3449 (1997).

[148] P. Castrillo, G. Armelles, J. P. Silveria, F. Briones, and J. Barbolla, Optical phonons of strained GaAs/GaP quantum wells studied by Raman spectroscopy, Phys. Lett. **71**, 1353 (1997).

[149] T. Nomura, K. Murakami, K. Ishikawa, M. Miyao, T. Yamaguchi, A. Sasaki, and M. Hagino, Structure of GaAs heteroepitaxial layer grown on GaP(001) by molecular beam epitaxy, Surf. Sci. **242**, 166-170 (1991).

[150] T. Nomura, K. Ishikawa, K. Murakami, and M. Hagino, Anisotropic relaxation of misfit strain in GaAs films grown on GaP (001), J. Cry. Growth. **127**, 584-588 (1993).

[151] B. J. Ohlsson, M. S. Miller, A. Gustafsson, and M.-E. Pistol, Anisotropic GaAs island phase grown on flat GaP: A Stranski-Krastanow-formed corrugated surface, J. Appl. Phys. **89**, 5726 (2001).

[152] T. S. Shamirzaev, D. S. Abramkin, A. K. Gutakovskii, and M. A. Putyato, High quality relaxed GaAs quantum dots in GaP matrix, Appl. Phys. Lett. **97**, 023108 (2010).

[153] D. S. Abramkin, M. A. Putyato, S. A. Budennyy, A. K. Gutakovskii, B. R. Semyagin, V. V. Preobrazhenskii, O. F. Kolomys, V. V. Strelchuk, and T. S. Shamirzaev, Atomic structure and energy spectrum of Ga(As,P)/GaP heterostructures, J. Appl. Phys. **112**, 083713 (2012).

[154] V. Popescu1, and A. Zunger, Localized interface states in coherent isovalent semiconductor heterojunctions, Phys. Rev. B. **84**, 125315 (2011).

[155] H.Kissel, U. Müller, C. Walther, and W. T. Masselink, Size distribution if self-assembled InAs quantum dots on GaAs (001) for intermediate InAs coverage, Phys. Rev. B. **62**, 7213-7218 (2000).

[156] K. Laidler, The Development of the Arrhenius Equation, J. Chem. Educ. **61 (6)**, 494 (1984).

[157] S. R. Logan, The orgin and status of the Arrhenius Equation, J. Chem. Educ. **59 (4)**, 279 (1982).

[158] M. K. K. Nakaema, F. Iikawa, M. J. S. P. Brasil, E. Ribeiro, G. Medeiros-Ribeiro, W. Carvalho Jr. , M. Z. Maialle, and M. H. Degani, On the origin of the blueshift from type-II quantum dots emission using microphotoluminescence, Appl. Phys. Lett. **81**, 2743 (2002).

[159] F. Hatami, M. Grundmann, N. N. Ledentsov, F. Heinrichsdorff, R. Heitz, J. Bohrer, and D. Bimberg, et.al, Phys. Rev. B. **57**, (1988).

[160] J. W. Tomm, T. Elsaesser, Yu. I. Mazur, G. G. Tarasov, Z. Ya. Zhuchenko, and W. T. Masselink, Transient luminescence of dense InAs/GaAs quantum dot arrays, Phys. Rev. B. **67**, (2003) 045326.

[161] Yu. I. Mazur, J. W. Tomm, V. Petrov, G. G. Tarasov, H. Kissel, C. Walther, Z. Ya. Zhuchenko, and W. T.Masselink,Staircase-like spectral dependence of ground-state luminescence time constants in high-density InAs/GaAs quantum dots, Appl. Phys. Lett. **78** , 3214 (2001).

[162] G. G. Tarasov,Yu. I. Mazur, Z. Ya. Zhuchenko, A. Maaßdorf, D. Nickel, J. W. Tomm, H. Kissel, C. Walther, and W. T. Masselink,Carrier transfer in self-assembled coupled InAs/GaAs quantum dots, J. Appl. Phys. **88**, 7162 (2000).

[163] A. Tackeuchi, Y. Nakata, S. Muto, Y. Sugiyama, T. Usuki, Y. Nishikawa, N. Yokoyama, and O. Wada, Time-Resolved Study of Carrier Transfer among InAs/GaAs Multi-Coupled Quantum Dots, Jpn. J. Appl. Phys. **34**, L1439 (1995).

[164] P. Tighineanu, R. Daveau, E. H. Lee, J. D. Song, S. Stobbe, and P. Lodahl, Decay dynamics and exciton localization in large GaAs quantum dots grown by droplet epitaxy, Phys. Rev. B. **88**, 155320 (2013).

[165] S. Dadgostar, J. Schmidtbauer, T. Boeck, A. Torres, O. Martínez, J.Jiménez, J. W. Tomm, A. Mogilatenko, W. T. Masselink, and F. Hatami, GaAs/GaP quantum dots: Ensemble of direct and indirect heterostructures with room temperature optical emission, Submitted to Appl. phys. Lett.

[166] T. Hino, S. Tomiya, T. Miyajima, K. Yanashima, S. Hashimoto, and M. Ikedaa, Characterization of threading dislocations in GaN epitaxial layers, Appl. Phys. Lett. **76**,3421 (2000).

[167] G. Stracke, E.M. Sala, S. Selve, T. Niermann, A. Schliwa, A. Strittmatter, and D. Bimberg, Indirect and direct optical transitions in In0.5Ga0.5As/GaP quantum dots, Appl. Phys. Lett. **104**, 123107 (2014).

[168] J. TersofI and R. M. Tromp,Shape Transition in Growth of Strained Islands: Spontaneous Formation of Quantum Wires, Phys. Rev. let. **70**, 2782 (1993).

[169] O. I. Mići ć, H. M. Cheong, H. Fu, A. Zunger, J. R. Sprague, A. Mascarenhas, and A. J. Nozik, Size-Dependent Spectroscopy of InP Quantum Dots, J. Phys. Chem. B. **101**, 4904-4912 (1997).

[170] F. A. Ponce, D. Cherns, W. T. Young, and J. W. Steeds,Characterization of dislocations in GaN by transmission electron diffraction and microscopy techniques, Appl. Phys. Lett. **69**, 770 (1996).

[171] S. Joshi, Quantum dash based photonic integrated circuits for optical telecommunications,Optics / Photonic. Institut National des Télécommunications, English. <NNT : 2014TELE0031>.https://tel.archives-ouvertes.fr/tel-01149697, (2014).

[172] H. Dery, E. Benisty, A. Epstein, R. Alizon, V. Mikhelashvili, G. Eisenstein, R. Schwertberger, D. Gold, J. P. Reithmaier, and A. Forchel, On the nature of quantum dash structures, J. Appl. Phys. **95(11)**, 6103-6111 (2004).

[173] J. H. Wei and K. S. Chan, A theoretical analysis of quantum dash structures, J. Appl. Phys **97(12)**, (2005).

[174] N. A. Jahan, C. Hermannstädter, J-H. Huh, H. Sasakura, T. J. Rotter, P. Ahirwar, G. Balakrishnan, K. Akahane, M. Sasaki, H. Kumano, and I. Suemune, Temperature dependent carrier dynamics in telecommunication band InAs quantum dots and dashes grown on InP substrates, J. Appl. Phys. **113**, 033506 (2013).

[175] D. G. Thomas and J. J. Hopfield, Isoelectronic traps due to nitrogen in gallium phosphide, Phys. Rev. **150**, 680 (1966).

[176] W. T. Masselink and Y.-C. Chang, Theory of the Exciton Bound to an Isoelectronic Trap in GaP, Phys. Rev. Lett. **51**, 509 (1983).

[177] T. Gessmann and E. F. Schubert, High-efficancy AlGaInP light-emitting diodes for solid-state lighting application, J. Appl. Phys. **95**, 2203 (2004).

[178] W. Jan, T.-F Liao, T. P. Chen, C. S. Chang, AlGaInP light emitting diode with metal reflector structure, Proc. of SPIE, The Int. Soc. Opt. Eng. **5739**, 81 (2005).

[179] W. T. Masselink and M. Zachau, $In_{0.35}Ga_{0.65}P$ Light-Emitting Diodes Grown by GSMBE, The seventh international Conf. on molecular beam epitaxy, 24-28. Aug. 1992, Schw ä bische Gm ünd, Germany; some of these results are published in Appl. Phys. Lett. vol. 61, pp. 58-60, 1992 and in J. Cry. Growth. **127**, 14-18 (1993).

[180] L. McGill, J. W. Wu, and E. A. Fitzgerald, Yellow-green strained-InGaP quantum-well epitaxial-transparent substrate light emitting diodes, J. Appl. Phys. **95**, 7561 (2004).

[181] M. Koike, N. Shibata, H. Kato, and Y. Takahashi, Development of high efficiency GaN-based multi quantum well light-emitting diodes and their applications, IEEE J. Selec. Topics in Quantum Elect. **8**, 271-277 (2002).

[182] C. Wetzel, Y. Xia, T. Detchprohm, P. Li, and J. S. Nelson, Development of high power green light emitting diode dies in piezoelectric GaInN/GaN, Proc. SPIE Int. Soc. Opt. Eng. **5739**, 1 (2005).

[183] T. Mukai, Recent progress in group-III nitride light-emitting diodes, IEEE J. Selec. Topics in Quantum Elect. **8**, 264-270 (2002).

[184] C-H. Lu, C-C. Lan, Y-L. Lai, Y-L. Li, and C-P. Liu, Enhancement of Green Emission from InGaN/GaN Multiple Quantum Wells via Coupling to Surface Plasmons in a Two-Dimensional Silver Array, Adv. Funct. Mater. **21**, 4719-4723 (2011).

[185] T. Shioda, H. Yoshida, K. Tachibana, N. Sugiyama, and S. Nunoue, Enhanced light output power of green LEDs employing AlGaN interlayer in InGaN/GaN MQW structure on sapphire (0001) substrate, Phys. Stat. Sol. (A). **209**, 473-476, (2012).

[186] F. Hatami,W. T. Masselink, H. Kostial, V. Lordi, and J.S. Harris, Red light-emitting diodes based on InP/GaP quantum dots, J. Appl. Phys. **97**, 096106 (2005).

[187] F. Hatami, W. T. Masselink, and J. S. Harris, Green emission from InP-GaP quantum-dots light-emitting diodes, IEEE Photonics. Tech. Let. **18**, 895 (2006).

[188] F. Hatami, W. T. Masselink, and J. S. Harris, Colour-tunable light-emitting diodes based on InP/GaP nanostructures, Nanotechnology. **17**, 3703-3706 (2006).

[189] F. Hatami, G. Mussler, M. Schmidbauer, L. Schrottke, H.-Y. Hao, H. T. Grahn, and W. T. Masselink, Optical emission from ultra-thin strained type-II InP/GaP quantum wells, Appl. Phys. Lett. **79**, 2886 (2001).

[190] A. Belabbes, C. Panse, J. Furthmüller, and F. Bechstedt,Electronic bands of III-V semiconductor polytypes and their alignment, Phys. Rev. B. **86**, 075208 (2012).

[191] A. De and C. E. Pryor, Predicted band structures of III-V semiconductors in the wurtzite phase, Phys. Rev. B. **81**, 155210 (2010).

[192] K. Streubel, N. Linder, R. Wirth, A. Jaeger, High brightness AlGaInP light-emitting diodes, IEEE J. Selec. Topics in Quantum Elect. **8**, 321-332 (2002).

[193] G. S. Solomon, J. A. Trezza, A. F. Marshall, and J. S. Harris, Phys. Rev. Lett. **76**,952 (1996).

[194] M. O. Lipinski, H. Schuler, O. G. Schmidt, K. Eberl, and N. Y. Jin-Phillipp, Strain-induced material intermixing of InAs quantum dots in GaAs, Appl. Phys. Lett. **77**, 1789 (2000).

[195] J. Ibáñez, A. Patané, M. Henini, L. Eaves, S. Hernández, R. Cuscó, L. Artús, Yu. G. Musikhin, and P. N. Brounkov, Strain relaxation in stacked InAs/GaAs quantum dots studied by Raman scattering, Appl. Phys. Lett. **83**, 3069 (2003).

[196] K. L. Simons, S. W. Sanderson, Light Emitting Diodes and the Lighting Revolution: The Emergence of a Solid-State Lighting Industry, Department of Economics Rensselaer Polytechnic Institute 110, 8th Street Troy, NY 12180-3590 USA, Email: simonk@rpi.edu.

[197] Y-K. Kuo, T-H. Wang, J-Y. Chang, and M-C. Tsai, Advantages of InGaN light-emitting diodes with GaN-InGaN-GaN barriers, Appl. Phys. Lett. **99**, 091107 (2011).

[198] A.K. Saxena, The conduction band structure and deep levels in Ga1-xAlxAs alloys from a high-pressure experiment, J. Phys. C. **13**, no.23, 4323-4334 (1980).

[199] J. Singh, Physics of Semiconductors and Their Heterostructures, McGraw-Hill, (1993).

[200] M. Leszczynski, M. Micovic, C. A. C. Mendonca, A. Ciepielewska, and P. Ciepielewski, Lattice constant of AlAs, Cryst. Res. Technol. **27**, 977-100 (1992).

[201] J. M. García, G. Medeiros-Ribeiro, K. Schmidt, T. Ngo, J. L. Feng, A. Lorke, J. Kotthaus, and P. M. Petroff, Intermixing and shape changes during the formation of InAs self-assembled quantum dots, Appl. Phys. Lett. **71**, 2014 (1997).

[202] M. Jo, M. Sato, S. Miyamura, H. Sasakura, H. Kumano, and I Suemune, Origin of the blueshift of photoluminescence in a type-II heterostructure, Nano. Res. Lett. **7:65**, 4 (2012).

[203] M. A. Sadeghzadeh, S. M. Azizi, Interfacial Al segregation limiting electron mobility at the inverted interface of AlGaAs/GaAs quantum well, Semicond. Sci. Technol. **27**, 105009 (2012).

[204] J. M. Moison, C. Guille, F. Houzay, F. Barthe, and M. Van Rompay, Surface segregation of third-column atoms in group III-V arsenide compounds: Ternary alloys and heterostructures, Phys.Rev.B. **40**, 6149 (1989).

[205] Y. Fu and M. Willander, Alloy scattering in GaAs/AlGaAs quantum well infrared photodetector, J. Appl. Phys. **88**, 288 (2000).

[206] M. Gould, S. Chakravrthi, I. R. Christen, N. Thomas, S. Dadgostar, Y. Song, M. L. Lee, F. Hatami, K-M. C. Fu, A Large Scale GaP on Diamond Integrated Photonics Platform for NV Center-Based Quantum Information, Journal of the Optical Society of America B **33**, No. 3 (2016).

Curriculum Vitae

LIST of PUBLICATIONS

Publications related to this work

- GaAs/GaP quantum dots: Ensemble of direct and indirect heterostructures with room temperature optical emission, **S.Dadgostar**, J. Schmidtbauer, T. Boeck, A. Torres, J. Jimenez, O. Martinez, J. W. Tomm, W. T. Masselink, F. Hatami, Appl. Phys. Lett. **108**, 102103 (2016).

- Room temperature green to red electroluminescence from (Al,Ga)As/GaP QDs and QWs, Christian Golz, **Shabnam Dadgostar**, W. Ted Masselink, and Fariba Hatami, SPIE OPTO, Vol. **9768** 97681I-1 (2016).

- A Large-Scale GaP-on-Diamond Integrated Photonics Platform for NV Center-Based Quantum Information, M. Gould, S. Chakravarthi, I. R. Christen, N. Thomas, **S. Dadgostar**, Y. Song, M. Larry Lee, F. Hatami, K-M. C. Fu, Journal of the Optical Society of America B **33**, No. 3 (2016).

- Red to green optical emission from (Al, Ga) As/GaP quantum structures, F. Hatami, **S. Dadgostar**, C. Golz, W. T. Masselink, CLEO: Science and Innovations, **STu3R. 1**, (2016).

- Efficient Coupling of Single Nitrogen-Vacancy Center Photons to a GaP-on-Diamond Integrated Optics Platform, M Gould, IR Christen, S Chakravarthi, **S Dadgostar**, F Hatami, KM Fu, CLEO: QELS-Fundamental Science, **FTu3D. 6**, (2016).

- Efficient extraction of zero-phonon-line photons from single nitrogen-vacancy centers in an integrated GaP-on-diamond platform, M Gould, ER Schmidgall, **S Dadgostar**, F Hatami, KMC Fu, arXiv preprint arXiv:1606.01826, (2016).

- Structural properties of AlGaP films on GaP grown by gas-source molecular-beam epitaxy, **S.Dadgostar**, E.H. Hussein, J. Schmidtbauer, T. Boeck, F. Hatami, W. T. Masselink, J. Cryst. Growth. **425**, 94-98 (2015).

- Thermal annealing effect on the structural properties of epitaxial growth of GaP on Si substrate, E. H. Hussein, **S. Dadgostar**, F. Hatami, W. T. Masselink, J. Cryst. Growth. **419**, 42-46.

Conference

- Structural and optical properties of GaAs quantum dots grown on GaP (100) substrate, **S.Dadgostar**,J. Schmidtbauer, T. Boeck, A. Torres, J. Jimenez, O. Martinez, J. W. Tomm, W. T. Masselink, F. Hatami,conference on Quantum Dots and Nanostructures: Growth, Characterization, and Modeling XIII, part of SPIE OPTO, 2016.

- Room temperature green to red electroluminescence from (Al,Ga)As/GaP QDs and QWs, C. Golz, **S.Dadgostar**, W. T. Masselink, F. Hatami, conference on Quantum Dots and Nanostructures: Growth, Characterization, and Modeling XIII, part of SPIE OPTO, 2016.

- Impact of growth temperature on the structural and optical properties of GaAs quantum structures grown on GaP (100) substrates, **S. Dadgostar**, J. Schmidtbauer, T. Boeck, A.Torres, O. Martìnez, J. Jimènez, F. Hatami, W. T. Masselink , DPG conference, Berlin, Germany, March 2015.

- Investigation of structural and optical properties of self-assembled GaAs quantum dots on GaP (100), **S. Dadgostar**, J. Schmidtbauer, T. Boeck, A.Torres, O. Martinez, J. Jimenez, F. Hatami, W. T. Masselink, EMRS fall meeting, Warsaw, Poland, September 2014.

- Structural properties of AlGaP films on GaP grown by gas-source molecular-beam epitaxy, **S. Dadgostar**, E.H. Hussein, J. Schmidtbauer, T. Boeck, F. Hatami, W. T. Masselink , MBE conference, Arizona, USA, September 2014.

- Structural properties of AlGaP films on GaP grown by gas-source molecular-beam epitaxy, **S. Dadgostar**, E.H. Hussein, J. Schmidtbauer, T. Boeck, F. Hatami, W. T. Masselink, DPG conference, Dresden, Germany, March 2014.

- Self-assembled growth of $In_xGa_{1-x}As$ quantum dots on GaP by gas-source molecular-beam epitaxy, **S. Dadgostar**, J. Schmidtbauer, T. Boeck, F. Hatami, W. T. Masselink, DPG conference, Dresden, Germany, March 2014.

- Impact of growth temperature on the interface quality of AlP/GaP superlattices grown using gas-source molecular-beam epitaxy, S. Dadgostar, F. Hatami, W. T. Masselink, DPG conference, Regensburg, Germany, March 2013.

- Effects of substrate temperature and annealing on structural properties of GaP/Si(100) grown by gas-source molecular beam epitaxy, E. H. Hussein, **S. Dadgostar**, F. Hatami, and W. T. Masselink, DPG conference, Regensburg, Germany, March 2013.

Selbständigkeitserklärung

Hiermit versichere ich, die vorliegende Arbeit selbständig und ohne unerlaubte fremde Hilfe angefertigt zu haben. Ich versichere, mich nicht anderweitig um einen Doktorgrad beworben zu haben. Die dem Verfahren zu Grunde liegende Promotionsordnung der Mathematisch-Naturwissenschaftlichen Fakultätp der Humboldt-Universität zu Berlin habe ich zur Kenntnis genommen.

Berlin, 14 December 2015

Shabnam Dadgostar